Detector Positioning in a Field-Deployable Limited-Angle Gamma Ray Emission Tomography System

by

Viridiana Borjas Padilla

A thesis submitted to the
School of Graduate and Postdoctoral Studies in partial
fulfillment of the requirements for the degree of

Master of Applied Science in Nuclear Engineering

Department of Energy and Nuclear Engineering

University of Ontario Institute of Technology
(Ontario Tech University)

Oshawa, Ontario, Canada

August 2023

Thesis Examination Information

Submitted by: **Viridiana Borjas Padilla**

Master of Applied Science in Nuclear Engineering

Thesis Title: Detector Positioning in a Field-Deployable Limited-Angle Gamma Ray Emission Tomography System

An oral defense of this thesis took place on August 10, 2023 in front of the following examining committee:

Examining Committee:

Chair of Examining Committee	Dr. Jennifer McKellar
Research Supervisor	Dr. Kirk Atkinson
Examining Committee Member	Dr. Ed Waller
Thesis Examiner, Ontario Tech University - FEAS	Dr. Eleodor Nichita

The above committee determined that the thesis is acceptable in form and content and that a satisfactory knowledge of the field covered by the thesis was demonstrated by the candidate during an oral examination. A signed copy of the Certificate of Approval is available from the School of Graduate and Postdoctoral Studies.

Abstract

Imaging techniques have been part of the medical and industrial fields for more than a century due to their simple use in the inspection of internal parameters without sample damage. These methods take advantage of the interactions of matter with the medium to present quantitative and qualitative information about a sample, where a sectional scanning technique that performs a rotation of the sample or the detection device is commonly used to capture and register relevant data. This technique is called Tomography, and it uses mathematical algorithms to process and analyze the data that will eventually form or reconstruct the image of the object of interest. Nevertheless, if a sample or detector rotation is not achievable due to dimension limitations or accessibility, a limited-angle tomography technique (sometimes called Laminography) can be performed via scans from a limited angular range. And, the limited captured data will be processed using more sophisticated reconstruction algorithms to compensate for these constraints. Therefore, in this thesis, limited-angle tomography of large samples with a mechanically supported detection device is modeled through mathematical methods and computational simulations in an object-oriented code system, in order to test its positioning capabilities.

Keywords: **Limited-Angle Tomography, Detector Positioning, Radioactive Samples, Geant4**

Declaration of Authorship

I, Viridiana Borjas Padilla, declare the thesis titled, "Detector Positioning in a Field-Deployable Limited-Angle Gamma Ray Emission Tomography System" and the work presented in it are my own. I confirm that:

- I hereby declare that this thesis consists of original work which I have authored. This is a true copy of the thesis, including any required final revisions, as accepted by my examiners.

- I authorize the University of Ontario Institute of Technology to lend this thesis to other institutions or individuals for the purpose of scholarly research. I further authorize University of Ontario Institute of Technology to reproduce this thesis by photocopying or by other means, in total or in part, at the request of other institutions or individuals for the purpose of scholarly research. I understand that my thesis will be made electronically available to the public.

Signed: Viridiana Borjas Padilla

Date: 25/08/2023

Statement of Contributions

I hereby certify that I am the sole author and sole source of the creative works and/or inventive knowledge described in Chapter 3. Mathematical Model. I have used standard referencing practices to acknowledge ideas, research techniques, and other materials that belong to others.

The development of Chapter 4. Computational Model is based on and developed with existing codes publicly available in Geant4 libraries and Dr. Mustafa Schmidt, Bergische Universität Wuppertal, tutorials and examples for Geant4.

The following work is a continuance of the preceding papers:

- K. D. Atkinson, "Development of a Gamma Emission Tomography System For High-Throughout Burn Up Assessment of Spent Nuclear Fuel Assemblies", *Transactions of the American Nuclear Society*, vol. 117, American Nuclear Society, Inc, 2017.

- K. D. Atkinson & L. Grana, "Development of a Limited Angle Gamma Ray Emission Tomography System for In-Situ Spatially-Resolved Measurement of Fuel Burn Up and Pre-Shutdown Power", *Transactions of the American Nuclear Society*, vol. 118, American Nuclear Society, Inc, 2018.

Dr. Kirk Atkinson, Ontario Tech University, provided the idea and direction for this project.

Acknowledgements

Foremost, I would like to express my sincere gratitude to my supervisor Dr. Kirk Atkinson for his direction and support throughout my master's program but, most of all, for inspiring me to always do more and encourage me to pursue a career in the field.

Also, I want to thank Dr. Filippo Genco for teaching me to never give up and bringing me support when I most needed it.

I would like to thank my family and friends from Mexico and Canada for always supporting me and keeping me sane—during the development of this thesis—in Spanish and English.

The completion of this thesis and master's program could not have been possible without the support, joy and grammatical reviews from my family from Canada; I will never stop thanking you. And my thanks to Kyle for introducing me to them and for encouraging me to always be my best.

Lastly, but most importantly, I want to thank my mom for her patience and motivation, and for being my role model. This work is yours.

Contents

List of Figures

List of Tables

Chapter 1

Introduction and Background

1.1   Motivation of Study

World events have shown how delicate international relationships can be, and how the uncontrolled use and ease of access to substances and tools dedicated to nuclear energy production can be wrongfully used. Thus, techniques that verify nuclear material and nuclear-related activities through on-site inspections, ongoing monitoring and evaluations [1] can be helpful in the attempt to control or supervise its usage. Safeguard assessments are validated by an international organization, the International Atomic Energy Agency (IAEA), to ensure that its members comply with the commitments of no utilization of nuclear programs for nuclear-weapon purposes. Therefore, the following thesis is motivated by the ongoing interest in optimization, and the limited independence and flexibility of the techniques typically utilized for non-destructive assay (NDA) inspections. With these examinations, structural and compositional information of the nuclear fuel existing conditions, and identification of missing or substituted rods in the assembly, is ideally represented by high-quality images. However, due to the large dimensions and shielding characteristics of the systems, complete on-site measurements of fuel systems have been a challenge. Nevertheless, an unconventional approach to perform an NDA with an imaging technique typically utilized for flat, complex and multilayered objects, that provides high-resolution depth information, could allow further fuel analysis. In this technique, special supports are utilized to perform flexible yet accurate motions of the sample since in the configuration, the sample is tilted with respect to the detector axis to

obtain scans from a limited angular range. However, this motion or change of position is not an option while studying nuclear systems on-site, so an unexplored limited-angle tomography technique with a detection device mounted on a mechanical support is undertaken in this thesis to corroborate the feasibility of the detector positioning during the data acquisition process.

1.2 Background of Imaging Methods

The first imaging technique was accidentally discovered in 1895 by Wilhem Röntgen while trying to study cathode rays. In the experiments, he discovered that a new type of radiation, x-rays produced by a cathode ray tube, formed a tinge on a fluorescent (barium platinum cyanide) screen when located near the tube [2]. To test the absorption properties of the rays, he placed different objects between the stream source (cathode tube) and the receptor screen (fluorescent plate) in a dark room for better visualization of the light emitted [3], encouraging him to record his discoveries on photographic plates for further validation [4]. Due to his excitement and curiosity about the rays behavior, he tested and recorded the hand of his wife while being irradiated with the x-rays which became the first radiographic image in history. At the end of 1895, according to Martz *et al.* [5] "Röntgen had demonstrated three major uses for x-rays that we continue today: medicine (various body parts), industrial inspection (his rifle complete with internal flaws), and baggage inspection (metal objects in a wooden box)". This awarded him the Nobel Prize in Physics in 1901.

As soon as Roentgen's studies became public, medical possibilities were evident. However, x-ray users and their patients began to notice side effects due to the direct contact and constant use of them. The symptoms escalated according to the amount of energy delivered by the source, exposure time of sample to source, and sensitivity of the tissue causing hair loss, skin dryness and burns, and cancer (often leading to death) [6]. These consequences called for an improvement in x-ray production and shielding, which meant a further study of its interaction with matter, and the creation of standards and limits to control and protect the public from its use.

1.2.1   Imaging

The purpose of imaging is to re-create or re-construct an exact copy of an object via data acquisition of its components. Thus, evolution in image capturing and information storage have played an important role in the advances of imaging methods.

When x-rays were discovered, fluorescent plates were used to reveal and study the interior of an object. But, in 1918, the cellulose nitrate film introduced by George Eastman substituted the use of these rigid and fragile photographic plates, allowing productivity, image quality, and consistency due to the flexibility of the mechanical chemical procedure to reveal images [7]. Nevertheless, the low quality and low dynamic range of film [8], along with its high flammability that started several fires and high toxicity that was responsible for later deaths [9], required a change in the chemical composition and methodology used. After 1950, scanners and electronic reproduction in electromechanical engravers replaced the photoengraving [10] commonly used in photographic film. At the same time, advances in image storage and processing evolved, but until the invention of digital computers and the effort to correct errors of film cameras, in the early 60s, the first digitized images were produced [11, 12]. Currently, image capture and processing by manual or digital techniques are part of common activities. New advances in multiple technologies have given them adaptability on several tasks in the medicine, industry, and design fields, just to mention a few.

1.2.2   Methods

Thanks to Roentgen's experiments, curiosity about the physical nature of x-rays and their difference from the already-known phenomena of luminescence for the emission and absorption of light, led to the discovery of different interactions of radiation with matter. An example of this is H. Becquerel's studies in 1895, who reproduced Roentgen's experiments, using uranium crystal plates in black paper exposed to sunlight for long periods and then kept in the dark [13]; since, at the time, it was believed that phosphorescent materials like uranium crystals, needed to be exposed to the sunlight to show a result or, in other words, exhibit

radioactivity. The rays emitted had high penetration characteristics and were able to ionize gases [14]. Soon after, his studies were retaken by Marie and Pierre Curie, which introduced for the first time the term "radio-active" to explain that the radiative activity on the observed rays depends on the nuclear structure of the sample used [15, 16]. At the same time, E. Rutherford conducted his own experiment, focusing on exposing a uranium compound to magnetic and electric fields, which produced two types of radiation: one that could penetrate thick materials (beta-rays), and another with low penetration characteristics or easy to absorb (alpha-rays) [17]. Later, P. Villard observed a non-deflecting and extremely penetrating type of radiation (gamma-rays) originating from radium in barium chloride [18]. Scientists kept studying the properties of the newly discovered rays, taking them to redefine the structure of the atom and observe several of their properties. For example, while studying interactions of alpha-rays with gas molecules, Rutherford provoked the first nuclear reaction [19], and W. Bother and H. Becker showed that some reactions can emit radiation [20], proving the existence of a neutrally charged particle - called neutron - in 1932 by J. Chadwick [21]. All these rays and particles have distinct interactions with matter, meaning different penetration characteristics and energy ranges, which allow variety in the methodologies used to acquire information from known and unknown objects.

From 1896 to 1912, several radioactive substances were discovered, each with different time intervals of radiation emission, and obeyed Rutherford and Soddy's theory for non-stable atoms that undergo spontaneous decay in an attempt to be stable while emitting radiation. So, the resulting daughter atom can have different chemical and physical properties than the parent or original atom [22, 23]. Due to the necessity of classifying them in the periodic table, Soddy in 1913 defined the concept of isotope to describe elements with the same nuclear charge but different mass [23].

Moreover, the non-stability, easy identification, and particular properties of radioactive substances in biological bodies marked a difference in detecting and treating diseases. Attempts to study the effects of radioisotopes (an unstable isotope that emits radiation) in organic tissues started in the 1900s with H. A.

Danlos and E. Bloch while treating skin tuberculosis with radium [24]. In 1913, George von Hevesy introduced the concept of radiotracers, where a radioactive substance is part of a chemical compound, to study biological systems [25]. This allowed the development of autoradiography, an imaging technique where an x-ray or photographic film is exposed to radioisotopes within a specimen, to localize and quantify the spread of radioactive substances in the body without obtrusion of normal functions [26, 27]. Thus, by the 1920s physicians have already been using barium sulfates to diagnose abdominal disorders and cancers [28]. Further studies, applications, and advances in radiobiology became possible with Joliot and Irène Curie's first fabrication of artificial isotopes through the bombardment of stable nuclei with alpha particles in 1934 [29], but its greater impact was not noticed until the production and use of radiopharmaceuticals, generated with particle accelerators and mass-produced with nuclear reactors [30]. Overall, the use of these radiobiological substances coupled with imaging technologies have allowed detection, treatment, and knowledge of disease - anomalies - in biological bodies like cancer; nevertheless, the use of radiotracers has played the same role for industrial systems in quality assurance as in material internal flaws.

As previously mentioned, the moment that x-rays were discovered, applications in health and industrial fields were evident, leading to a rapid and constant improvement of the techniques and machines used in imaging methods. For example, x-ray machines became more sophisticated in beam quality with exchangeable filters and beam hardening, confinement and shielding, use of thermionic cathodes (cathodes that emit electrons by the effect of temperature increase), beam focalization, rotation of targets, and others [31]. Meanwhile, imaging with non-ionizing radiation was developed years later by taking advantage of the wave-matter interactions. These techniques include ultrasounds or sonograms that use a transducer (i.e., a converter of electrical energy to mechanical or sound waves) to send sound waves and record the incoming echo from the sample's internal structure [32]; and, magnetic resonance imaging (MRI) which applies a strong magnetic field on protons within the body, in order to align them with the field so then a radio frequency can be introduced to disrupt

the proton's position in respect the magnetic field, producing electromagnetic signals with characteristic frequencies that identify the different body tissues [33]. To obtain more information and better image quality, scanning methods for x-ray machines combined with mathematical models were developed after 1960; they acquired and merged multiple images from different angles to reconstruct a complete view of the object, such methods are known as tomographic techniques. The most known are the Computed Tomography (CT) technique, which analyzes and identifies structural aspects of the object, and the Positron Emission Tomography (PET) and the Single Photon Emission Computed Tomography (SPECT) techniques, which focus on functional processes and radioactivity concentrations within the sample. PET and SPECT include the use of radiopharmaceuticals, PET involves nuclear substances emitter of positrons (i.e., positively charged electrons), and by getting in touch with electrons, annihilation occurs producing two detectable gamma-rays 180 degrees apart from each other [34]; whereas SPECT employs γ-emitting radionuclides since a single gamma photon can be produced by the natural decay of the isotopes, and be detected [35]. In contrast, CT uses a narrow x-ray beam that rotates about the object and obtains sectional images or projections of it from every angle [36]. In all cases, image reconstruction methods are used, which involve mathematical models that incorporate all these projections in an entirety. Currently, combinations of these techniques have been developed to compensate for limitations or to complement each other. Even though these methods were developed to study and understand the human body, other fields of industry have taken advantage of their non-invasive characteristics to identify abnormalities in material structures or thermal abilities, inspection of components, and flaws [37]. For instance, in the nuclear industry, energy production through induced fission reactions between a neutron and a large atom leads to the constant handling and usage of radioactive substances. Thus, attempts to understand their processes and dynamics are essential for efficient and controlled reactions. Since radioactive substances must be held in special containers, a key to studying these systems is using tomographic methods based on the energies emitted by the substances. In the case of nuclear reactors, high energies like gamma-rays allow imaging

reconstruction of items behind thick process vessel walls [38], or to characterize fuel relocation structures through mapping of the radioactive activities [39].

Finally, it is important to highlight the danger and sensibility of living organisms to high-penetrating energies commonly used in imaging techniques. As mentioned, the first uses of radioactive substances were not controlled due to the unawareness of the long- and short-term consequences of the materials. In 1913, the German Röetgen Society was the first to propose a set of recommendations to reduce radiation exposure to workers [40]. Years later exposure limitations, unit definitions, and protection standards for national and international governments were stipulated. The International Basic Safety Standards (the BSS) is used to protect workers, patients and public from ionizing radiation [41] while the IAEA oversees the safe, secure and peaceful use of nuclear energies. They work together to ensure that radiation exposure of the public is kept as low as reasonably achievable through standards and regulations [42]. The IAEA has issued a set of Safety Standard Series that covers nuclear, radiation, transport and waste safety. In addition, other safety reports related to nuclear activities are also available to the public.

1.3   Thesis Outline

Imaging techniques vary in design, performance and quality control. These aspects can be modified individually, but it must be considered that altering one will influence the others. And, this will be reflected in the image quality, to be specific on its resolution and contrast. But image reconstruction methods can improve this quality and reduce the use of radiation doses in the system, which has a great impact on the nuclear field since safety, security and control over the usage of radioactive substances is of main concern. Thus, an imaging technique configuration that allows less human interaction in the process is substantial to achieve a reduced dose exposure time and inaccuracy.

In this project, a mechanical support for the detection device utilized in a modified gamma-ray emission tomography system is proposed as a flexible and accurate form of motion for the detector. This structure could eliminate human

errors like inaccuracies on the detector positioning and reduce the worker's dose exposure due to the structure's easy adaptability to every type of surface with independently adjustable legs. The modified emission tomography system and the proposed mechanical support are presented and described in six chapters and three appendices. So far, in Chapter 1 an introduction and background to the first imaging techniques, and their main components have been provided to demonstrate the importance and motivation in the scientific community around tomography systems. To understand the methodology and objective of the work, Chapter 2 reviews the fundamental concepts of tomography, its applications in medical and industrial fields, and the advantages and disadvantages of their use; along with some imaging reconstruction methods that are supported by Appendix A, where an overview of data processing is presented. The mechanical support is delineated in Chapter 3 through a mathematical model and fundamental concepts used to describe the possible types of motions for the structure, and in Chapter 4 through a computational simulation of the system's configuration, which is supported by Appendix B and Appendix C that contain the constructed code. Finally, Chapter 5 and Chapter 6 present and discuss the obtained results, conclusions and future work on the proposed mechanical support, and equipment and simulation performance.

Chapter 2

Literature Review and Work Statement

Tomography is a sectional imaging technique which is non-invasive and adaptable to various ionizing radiation sources, with an extended list of applications in medical and industrial fields for the detection of anomalies and analysis of systems. Thus, the following chapter presents a literature review of the current use and knowledge acquired of gamma-ray tomographic techniques and variations of it; however, some fundamental concepts must be covered first to understand the terminology used and the objective of the study.

2.1   Fundamentals and Literature Review

The sectional images or projections from tomographic systems are obtained through scanning methods that vary with the source characteristics. As discussed, radiation has the ability to interact with matter. The process will depend on the ionizing energy source used, resulting in a wide list of distinct consequences and reactions which can be divided by the interaction of matter with charged particles or the interaction of matter with photons. This paper is focused on the interaction of electromagnetic radiation with matter, specifically γ-rays, due to its non-destructive, high-penetrating and adaptable characteristics in tomographic systems for nuclear applications. Further details and specifications of these processes are explained in Section 2.1.1 along with detection mechanisms.

In Section 2.1.3, an overview of imaging techniques utilizing γ-rays is provided, since the configuration used in the scanning process depends on the radiative properties of the sample and movement of the source. In general, the object of study can be classified as a radioactive or non-radioactive substance to facilitate the layout of the system. For instance, with non-radioactive objects, Computed Tomography (CT) scans are commonly used and generated with an x-ray that is beamed onto a detector while Positron Emission Tomography (PET) or Single-Photon Emission Computed Tomography (SPECT) scans use radiopharmaceuticals that emit, or result in the emission of, gamma rays in all directions which are detected by rotating or stationary devices.

Since several projections are taken in one run, mathematical reconstruction methods are often used to recreate a visualization of the original system from those sectional images, which will produce three-dimensional (3D) imaging and real-time 3D imaging videos (i.e., four-dimensional (4D) imaging). A further and detailed explanation of some of these algorithms is developed in Section 2.1.2.

The constant innovation in technologies over the years has allowed adaptability and variety on tomography systems for fields like medicine, in the detection, treatment and tracing of rare diseases; and in the industry, for analysis of the internal structures of a system. However, other common applications in sciences include archaeology for quantitative measures of antique artifacts [43], biology for morphological behavior of biological systems [44], astrophysics for analysis of internal and external phenomena of celestial bodies [45], and nuclear for inspection of nuclear waste [46] or to analyze irradiated nuclear fuel [47]. Therefore, Section 2.1.3 presents a thorough review of applications for modified γ-ray tomographic systems that have taken part in innovative and modern studies of radiative systems which, combined with visual reconstruction tools, allow a better understanding of the problem and provide forecast reinforcement.

2.1.1 Interaction of Radiation with Matter

Overall, in its simplest form, a gamma ray tomography system consists of a radioactive source, a sample and a detector that captures the remaining traces of energy or charged particles (products of the interaction of radioactive substances

with the particles in the sample or medium, see Figure 2.1) that are distributed in the sample. Due to this, a deep understanding of the effects caused by the different interactions between radiation and matter is necessary for the development of the project.
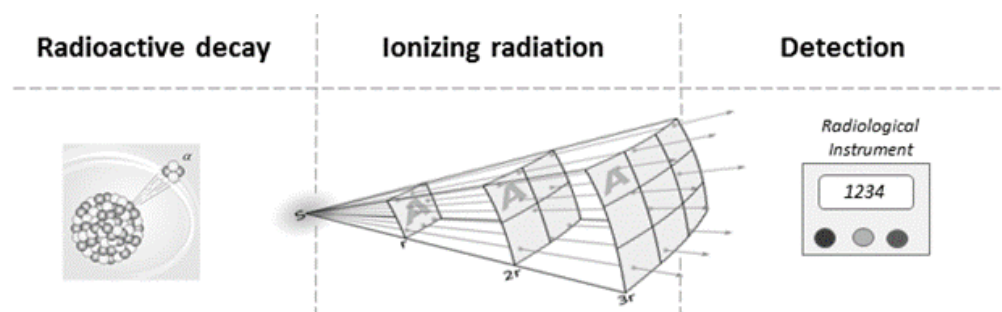
FIGURE 2.1: Process followed in the detection of isotopes, that go through spontaneous disintegration and emit ionizing radiation [48].

Radioactive Decay

Matter is composed of compounds or elements, compounds are formed by molecules, molecules are two or more elements combined, elements are made of atoms, and atoms are constituted by particles. An atom's structure is integrated by electrons (negatively charged particles) that orbit around a nucleus, which comprises protons (positively charged particles) and neutrons (neutrally charged particles); the number of electrons and protons in an atom is equal, thus a single atom has a neutral charge. The number of protons, or atomic number (Z), is characteristic of its element, meaning that all elements have a different number of protons while atoms with the same number of protons belong to the same element [49]. However, the number of neutrons in an atom can vary in different and same elements. Thus, atoms of the same element with different neutron numbers are called isotopes. And the combination of the number of protons and neutrons constitutes the mass number (A) [50]. As mentioned, electrons move around the nucleus of an atom. This movement can be described by orbitals that will show where the electron is likely to be found. An atom has different orbital levels, and each of them is quantized; in other words, electrons possess discrete

energy values that will determine their position in the atom's orbitals [51]. Figure 2.2 is a representation of these orbitals. Following this, if an electron gains enough energy, it will enter an excitation state and jump to the next high-energy level, but if it loses energy then it will be de-excited and fall to a lower-energy level. In both processes, absorption and emission of energy will be seen in the form of a wave or particle. If the energy being delivered is high enough to remove the electron from the atom, then this process is called ionization [52]. Furthermore, an electron that is in an excited state cannot remain there, so it will eventually decay to a lower state level and release energy in its process.
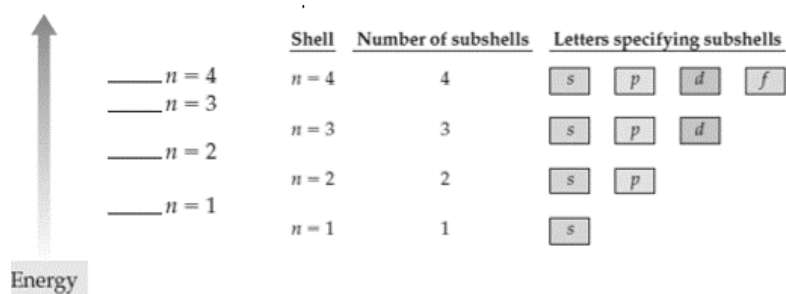
FIGURE 2.2: Energy levels on the atom's configuration (or principal quantum numbers) with its respective subshells for the first four orbitals [51].

The atom configuration consists of a nucleus that contains neutrons and protons "glued" together due to the nuclear force that compensates for the repulsive electromagnetic forces between positive charges; and electrons that surround the nucleus while remaining in their orbital by the effect of electromagnetic forces, because of the attraction between negative (electrons) and positive (protons) charges [53]. That said, atoms are constantly looking for equilibrium in their forces so specific combinations of neutrons and protons produce a stable nucleus, but excess neutrons cause instability due to the spare amount of energy in the nucleus, leading to a radioactive decay [54]. This process is called radioactive because, during decay, the element loses energy in the form of electromagnetic waves or high-energy particles. The decay of a radioactive element (isotope) to a stable one is spontaneous and not always singular; nevertheless, the probability that this active atom disintegrates in a certain time

interval can be predicted through the following calculations since every isotope has the same chance of decaying in one second [54][55]. Let us assume that the probability of decay at this time (per second) is denoted by λ. At the start, the substance has a certain number of atoms N but after disintegration occurs, this number will decrease per second λN so the rate at which the loss of atoms happens is determined by

$$\frac{dN}{dt} = -\lambda N. \tag{2.1}$$

And the integral form of Equation 2.1 at a time t, with a number of atoms at time zero N_0 is

$$N(t) = N_0 e^{-\lambda t}. \tag{2.2}$$

The rate of atoms lost at a time t is called activity α and is measured in Bq (Becquerels) or ds (disintegrations per second), that applied to Equations 2.1 and 2.2 has the form

$$\alpha(t) = \lambda N(t), \tag{2.3}$$

and with an activity at time $t = 0$

$$\alpha(t) = \alpha_0 e^{-\lambda t}. \tag{2.4}$$

The half-life of the isotope occurs when half of the initial number of atoms remains on the substance $N/N_0 = 1/2$. Thus, Eq. 2.2 will take the form of

$$\frac{1}{2} = e^{-\lambda t}$$

using a logarithm on both sides, denoting the time at this point $T_{1/2}$ and re-arranging for this term, indicating the half-life measured in s (seconds)

$$T_{1/2} = \frac{\ln 2}{\lambda}, \tag{2.5}$$

where $1/\lambda$ is the mean life $\bar{t}$ of the substance, or the time required for N to decrease by a factor of $1/e$. A graphic representation of the loss of atoms through time can be seen in Figure 2.3.

It should be noted that for each atom decayed a new radioactive nuclei may
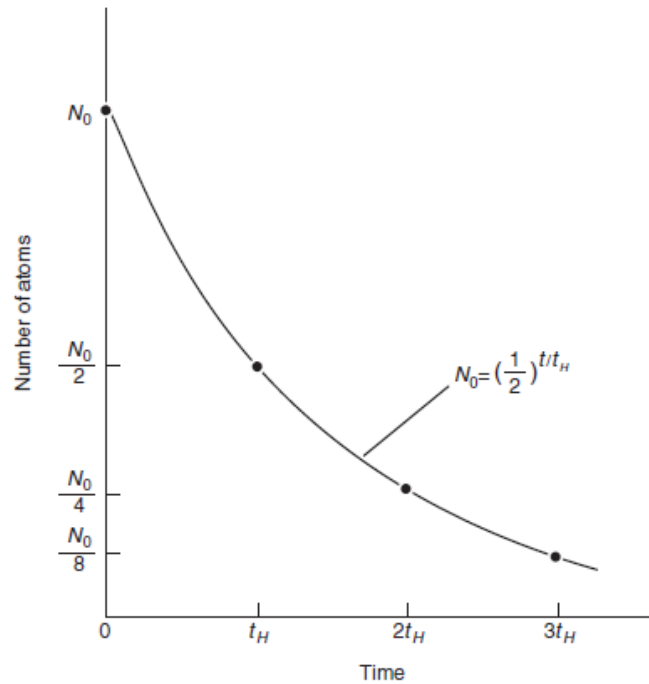
FIGURE 2.3: Exponential decay law: the number of atoms in a
substance as a function of time. At any t time, the ratio between
the present and initial atom number is $\frac{N}{N_0} = (\frac{1}{2})^{t/T_{1/2}}$ [54].

be formed, leading to a decay chain with activity and number of atoms dependent
on the atom parent. In the same manner, calculations can be made but will be
omitted in this paper.

Ionizing Radiation

When an unstable atom decay releases energy in the form of electromagnetic waves
or high-energy particles because of its de-excitation process, this energy is said to
be ionizing due to its ability to separate tight-bound electrons from its atom. Thus,
a spontaneous decay can emit alpha (α) particles, beta (β) particles, neutrons (n)
or protons (p), or go through electron capture. At the same time, these reactions
can be accompanied by electromagnetic waves like x-rays or gamma (γ) rays (which
depends on the origin of the process, if they originate from inside or outside the
nucleus). This is due to the excess of energy left in the nucleus (or due to internal
conversions) during these processes, which will be discussed later. Therefore, the

emission of energy will be dictated by the type of transformation that the atom is facing.

The different types of radioactive decay behave and occur with the following characteristics:

Neutron radiation. This process is initiated by the free neutrons product of nuclear fission, fusion reactions or beta decay. In these processes, ionization is not produced by neutrons. Instead, it is done indirectly by knocking or altering the nuclei while the neutron passes through matter. Neutrons can be scattered inelastically and produce γ-rays that induce ionization [55]. Since these particles do not have a charge, they can travel long distances before interacting; therefore, their penetrating characteristics are strong and they can only be stopped by low Z materials, like those with great concentrations of hydrogen (e.g., water or paraffin).

An example of this reaction can be seen with beryllium which is used for alloys of copper or nickel

$$^{13}\text{Be} \longrightarrow {}^{12}\text{Be} + \text{n}.$$
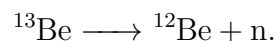
Alpha decay. The process occurs typically in a heavy nucleus when there is an excess of protons. Thus, to reduce the repulsive forces between positive particles, an α-particle is emitted; this is a helium ion that consists of two protons and two neutrons. Their energies range between 4-7 MeV and, due to their large mass, they are likely to interact with other particles in their surroundings (e.g., air) and lose all their energy [56].

An example of this decay reaction is the nuclear fuel ${}^{232}_{90}\text{Th}$

$$^{232}_{90}\text{Th} \longrightarrow {}^{228}_{88}\text{Ra} + {}^{4}_{2}\text{He}.$$
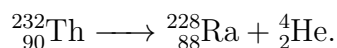
Beta decay. A β-ray is a high-energy electron or positron. In this process a transformation in the nucleon occurs, and is shown through three means [57]:

– β^- decay, for neutron-rich atoms or high-Z elements with a small mass, a neutron decays into a proton, an electron and an anti-electron-type neutrino ($n \longrightarrow p + e^- + \bar{\nu}_e$).

An example of the reaction is the decay of ^{198}Au, commonly used for seed implantation therapy

$$^{198}\text{Au} \longrightarrow {}^{198}\text{Hg} + \beta^- + \bar{\nu}_e.$$
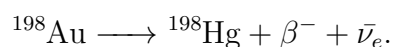
– β^+ decay, for proton-rich atoms or for elements with a mass difference larger than two electron masses at rest, where a proton transforms into a neutron by emitting a positron and electron-type neutrino ($p \longrightarrow n + e^+ + \nu_e$).

An example of this process is the radioisotope ^{13}N which is typically used in PET scanning

$$^{13}_{7}\text{N} \longrightarrow {}^{13}_{6}\text{C} + \beta^+ + \nu_e.$$
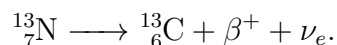
– Electron capture, for proton-rich atoms that capture an electron from an inner orbit, creating a proton and an electron-type neutrino ($p + e^- \longrightarrow n + \nu_e$).

An example of the electron capture reaction can be seen in the isotope ^{51}Cr normally used for labelling red blood cells

$$^{51}_{24}\text{Cr} \longrightarrow {}^{51}_{23}\text{V} + \nu_e.$$
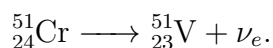
Gamma decay. As mentioned, γ-rays usually follow a β- or α-decay. Thus, in this reaction, a nucleus decays to a lower energy state of the same element by releasing a photon with wavelengths between 10^{-11} m and 10^{-13} m. The most common gamma sources are those isotopes that emit a beta-particle since they produce γ-rays with higher energies than those with alpha emissions [58]. Moreover, γ-rays and x-rays are similar since both are a form of electromagnetic radiation, but gamma-rays originate from the nucleus and x-ray processes are produced outside the nucleus. Due to the

high energies and product of second radiation, gamma's absorption characteristics are greater than β-rays; thus, materials with high-atomic numbers and densities (e.g., barriers of lead and concrete) are ideal absorbers.

An example of this reaction is the ^{60}Co decay, normally used for instrument sterilization

$$^{60}\text{Co} \longrightarrow {}^{60}\text{Ni} + \beta + \gamma.$$
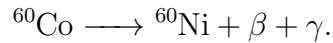
Interaction of Gamma-Rays with Matter

It is known that γ-rays have deep penetrating characteristics since photons are either absorbed or scattered in their pass-through matter. Therefore, the intensity of the rays will be gradually reduced or attenuated while the remaining photons are unaltered [59]. In their matter traversal, a probability of interaction or collision per unit path length exists. This probability is called the linear attenuation coefficient of the medium μ or macroscopic cross-section (i.e., the effective target area that considers a specific limp of a material), the quantity of which depends on the photon energy and the material's atomic number [60]. For a better understanding of the attenuation and diffusion characteristics of the γ-rays, let us assume that a narrow collimated beam of mono-energetic gamma-rays with an intensity I passes through a uniform material of thickness x, as depicted in Figure 2.4.

In this process, the intensity or number of photons in the beam will be reduced after traversing the material, producing a photon rate reduction of the following form

$$-dI/I = \mu dx \tag{2.6}$$

where dx represents a portion of the material with depth x. The integral form of the previous equation is

$$I(x) = I_0 e^{-\mu x}, \tag{2.7}$$

obtained by an initial intensity I_0 and an exponential decreasing factor dependent on the linear attenuation coefficient μ and the material thickness x [62]. Following the same concept as the radioactive decay law, the mean free path of a
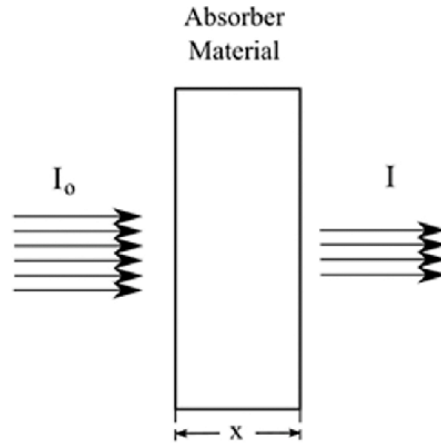
FIGURE 2.4: Passing of a γ-ray with initial intensity I_0 through an absorber material of thickness x, and a resulting intensity of I due interactions of the medium and the ionizing radiation [61].

gamma source (in this case, $1/\mu$) represents the average distance traveled by the particle before an interaction occurs. Additionally, for a material with density ρ, the attenuation coefficient can be expressed in terms of its mass m and microscopic cross-section σ (i.e., the effective target area of a single nucleus in the sample) [63].

$$\frac{\mu}{\rho} = \frac{\sigma_{total}}{m}. \tag{2.8}$$

Therefore, the expression for a compound is of the form

$$\frac{\mu}{\rho} = \sum_i \omega_i \frac{\mu_i}{\rho_i}, \tag{2.9}$$

where ω_i is the weight fraction of the i-th element.

As mentioned, gamma rays have the probability to interact with matter through absorption or scattering means. These processes are via Photoelectric Absorption, Compton Scattering and Pair Production. Each contribution is plausible at different energy ranges and, since there is no interference between them, a total cross-section for the γ-ray can be calculated by considering the

probability of interaction of each process:

$$\sigma_{total} = \sigma_{PE} + \sigma_{CE} + \sigma_{PP} \tag{2.10}$$

where $\sigma_{CE} = Z\sigma_C$ and Z is the number of electrons [60]. In the same manner, a N density of γ-rays probability of interaction can also be derived by defining the macroscopic cross-section, which is represented by the attenuation coefficient μ on γ-ray interaction notation. Therefore, a more general form of interaction probability can be stated in the following form

$$\mu = N\sigma = \mu_{PE} + \mu_{CE} + \mu_{PP}, \tag{2.11}$$

where N is the atom density and is calculated with $N = \frac{\rho N_A}{M}$ with N_A as Avogadro's number and M as the gram atomic weight [52]. And a mass attenuation coefficient defined with

$$\frac{\mu}{\rho} = \frac{\mu_{PE}}{\rho} + \frac{\mu_{CE}}{\rho} + \frac{\mu_{PP}}{\rho}. \tag{2.12}$$

The characteristics governing these interactions are outlined in the following list.

- **Photoelectric Effect (γ + atom $\longrightarrow$ e$^-$ + ion).** This effect dominates at low photon energies (around 100 keV), where the light will be totally absorbed by the atom involved in the interaction. When a photon of this energy range interacts with a high-Z element, all the energy carried by the γ-ray is transferred to an electron of this type of element, causing its ejection and leaving a vacancy. At the same time, an electron from an outer shell can occupy this place and emit an x-ray due to the de-excitation process, or transfer the energy to an outer electron and be ejected from the atom (i.e., Auger electron) [64].

- **Compton Scattering (γ + atom $\longrightarrow$ γ + e$^-$ + ion).** It dominates in ranges between 100 keV and 10 MeV. The process occurs when a photon interacts with an electron of an outer shell, leading to the photon being scattered and transferring part of its energy to the released recoiled electron [62].

- **Pair Production ($\gamma + $ atom $\longrightarrow$ e$^+$ $+$ e$^-$ $+$ atom).** For photon energies above 1.022 MeV, an incident photon or γ-ray is absorbed by a strong electric field (or Coulomb field) of a nearby charged particle, and transformed into an electron and a positron each carrying 0.511 MeV of energy. Both particles will eventually interact and annihilate while producing two energetic photons. [56].

Detection and Imaging of Gamma-Rays

Detection mechanisms make possible the measurement and analysis of radioactive substances. Their specifications depend on the energy ranges emitted by the sample, performance, and the application's desired resolution and efficiency. Overall, γ-ray detectors can be divided by their application purpose, where spectrometers are usually used to measure the incoming energy and transform it into an electric signal while imagers use the incoming energy to reconstruct images of the radiative object. The most common and utilized device for gamma imaging is the Anger Camera or Gamma Camera (γ-Camera), a device consisting of a collimator, a position-sensitive scintillator and photomultiplier tubes (PMTs) [65]. This section focuses on the interactions of γ-rays with the components of imagers that lead to data collection and processing. For specifications on imaging technologies and techniques, refer to Section 2.1.3.

Gamma-ray imaging techniques have the ability to measure and localize radioactive substances in a system. The data acquisition is performed by devices with the ability to convert the energy emitted by radiative samples into readable electrical signals that will later be transformed into images, see Figure 2.5 for reference.

The process is done, first, by obtaining the directionality of the sample through a collimator that will absorb γ-rays that are not parallel to the collimator's plates, delimiting the angle of incidence and resulting in image resolution improvement [67]. Common collimator materials are γ-ray absorbers like lead or tungsten discs.

Then, the projected image of the distribution of the rays passes through a filter and comes in contact with a crystal plane scintillator that will transform them into flashes of light [68]. An ideal scintillation device contains and has the
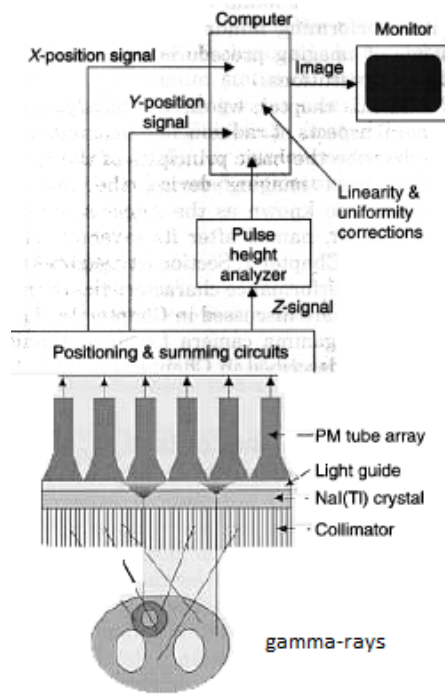
FIGURE 2.5: Configuration of gamma-ray imaging devices. A
γ-ray will pass through a collimator to determine the directionality
of the source, then those filtered photons will be absorbed by a
scintillator detector connected to a photomultiplier (PMTs) where
the interaction of the rays with the detector will result in energy
emission and then transformed into measurable pulses [66].

capacity to convert all the photon energy absorbed by the crystal into detectable
light, a ratio of transformed energy proportional to the deposited energy, a
medium transparent to the emitted wavelength, a short decay time, and an index
of refraction close to glass [69]. However, no crystal complies with all these
characteristics; thus, compromises arise for the desired and obtained outcome.
Scintillators are fabricated with different crystal materials that are commonly
divided into organic and inorganic. Each composition shows advantages according
to the type of source used. For example, organic scintillators have a good
performance measuring beta spectrum and detecting fast neutrons while
inorganic scintillators, with a high density and atomic number, easily detect γ-
and x-rays [70]. Therefore, the selection of an inorganic scintillator detector is

ideal for isotopes that emit γ-rays. The most common inorganic scintillator used is a sodium-iodide (NaI) crystal with a 0.1% of thallium (Tl) as its activator due to its good signal-to-noise ratio and resolution characteristics [70]. This device produces flashes of light by means of the crystal-lattice effect. The inorganic crystal inside of the scintillator consists of a three-dimensional structure with periodically repeated arranged patterns of atoms, where the pattern can be a single or group of atoms, or a single or group of molecules [71]. This pattern of atoms is repeated and arranged to form the characteristic shape of a crystal, where each atom is said to be joined by another atom with a straight line; thus, the atom, molecule or ion in the crystal represents a lattice point or site [72]. In addition, as previously stated, an atom has electrons distributed in its atomic orbitals, where the closest one to the nucleus is called the conduction band and the outermost is the valence band [73]. The electrons in the valence band are bound to lattice points but the ones in the conduction band have the freedom to move through the crystal, leading to interactions that provoke transitions from the valence to the conduction band or the exciton band, which leaves a vacancy in the valence state [74]. The exciton band is below the conduction band, and above and separated from the valence state by a forbidden gap. If the excited electron does not have enough energy to jump to the conduction band, a bound state or exciton is created between the electron and the vacancy, located in the exciton band [59]. These pairs travel all along the crystal until an activation center absorbs them as a whole. Independent of this, the electron-hole pair is also free to move individually, the hole will travel directly to the activation site and ionize it since the impurity energy is less than the lattice site. Meanwhile, the electron is free to move through the crystal until it encounters an ionized activator [75]. An activation center will create energy levels in the forbidden gap and are introduced by the impurities or activators [69]. Thus, the activation center acts as an excited state where the de-excitation to the activation center ground state will produce the emission of visible light; see Figure 2.6 for visualization of these energy levels. The time that the light is emitted will depend on the half-life of the excited state with two characteristic emission bands; one given by the activator and the other one given by the crystal lattice at short wavelengths [59]. Furthermore, it can be
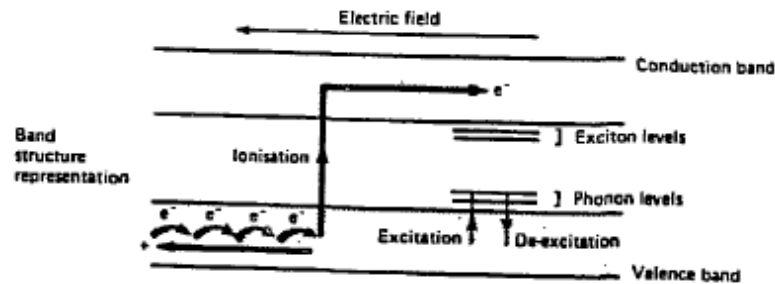
FIGURE 2.6: Band structure representation of a scintillator's crystal containing an activator [70]

inferred that γ-rays are not detected by a scintillator. In fact, the secondary electrons produced by the interaction of the ionizing source with the crystal are the initiators of the visible light production and obey the gamma-ray-matter interaction procedure, where each process (i.e., Photoelectric Effect, Compton Scattering and Pair Production) governs at a certain energy range.

Some devices may contain a plastic light guide between the scintillator and the photomultiplier tube to enhance the light collection process and improve uniformity. The light guide directs the flashes produced by scintillation processes away from gaps on the PMT, which is performed by etching a pattern in the plastic guide. However, light directionality can also be achieved by using hexagonal or square PM tubes arranged without gaps on the scintillation device, assuming good light dispersion at the PMT entrance window [76].

Moreover, for the last step of data acquisition and processing, the obtained flashes of light produced by the scintillation device will pass through a photomultiplier with the purpose of transforming weak light into measurable electrical signals without adding important amounts of noise. A PMT is formed by a photocathode, a set of dynodes and an anode; all enclosed in a glass structure under vacuum conditions to ensure acceleration of the electrons, see Figure 2.7.

The device serves as a sensitive detector connected to the bottom section of the scintillator. When the scintillation light enters the PMT, it comes in contact with a photocathode that will transform these photons into low-energy electrons by photoelectric interactions. The resulting photoelectrons are accelerated by an

Incident light

Semitransparent
photocathode

15

Photocathode
to dynode No. 1
electron optics

Typical
photoelectron
trajectories

14
14

14
14

14

14

2
4
1
3
5
6
7
Electron
multiplier
8
9
10
11
12 13

Vacuum
enclosure

1–12: Dynodes   14: Focusing electrodes
13: Anode   15: Photocathode
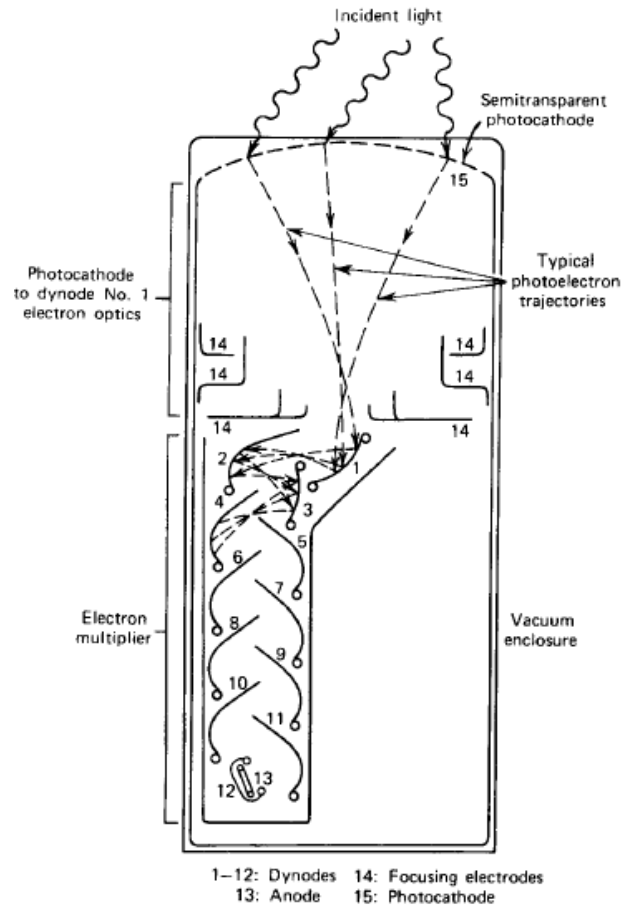
FIGURE 2.7: Configuration of a photomultiplier. A photocathode transforms the incoming light into electrons to later be accelerated through an electric field and directed to a dynode coated with Cesium-Antimony (Cs-Sb) or Silver-Magnesium (Ag-Mg). This process is repeated for the multiplication of the photoelectrons. Finally, the output is collected at the anode in the form of measurable pulses [69].

electric field produced by the positive and negative components of the system and then focused towards a dynode. The interaction between the stream and the plate will produce secondary electrons, obtaining a conversion of light into electrons. This process is repeated for every dynode leading to an amplification of the electron pulse by a factor of 10^8. The final charge or output will be collected at the anode, and because the amplification is linear, the output pulse height will be proportional to the original energy deposited in the scintillator [59][69][74].

Finally, these signals are sent to an electronic or digital position logic circuit, where a weighted average method is performed on the pulses for identification of the energy deposited in each event and the localization of its X and Y components, which are associated to a two-dimensional grid or pixel that will later conform an image [76]. Therefore, several events are needed to form or reconstruct an image and, in the same way, each pixel must contain an acceptable number of counts to obtain a tolerable signal-to-noise ratio. Nevertheless, this stage can be approached through different mathematical methods for image reconstruction purposes, treatment of missing data, reduction of noise or resolution improvement, and enhancement of image quality. Some methods include Iterative Algorithms and Filtered-Back Projection Algorithms, see Section 2.1.2 for more information.

Alternatively, spectrum analysis can also be performed with the output pulse resulting from the PMT processes. A graph of the count rate versus pulse height can be obtained and is referred to as the pulse-height spectrum [70]. Since the detection of the γ-rays is based on its interactions with matter where the obtained electrical signal is proportional to the energy deposited on the detection device, those interactions where the electron absorbs all the gamma energy are said to be the most efficient, that is the photoelectric effect. When this process occurs a well-defined pulse or peak will be seen in the spectrum. This peak is called photopeak and it represents the maximum energy or total absorption peak on the spectra. However, other interactions like Compton Scattering are not considered ideal, since its spectrum is continuous on the low energy side, where contributions to other processes are possible and superimpositions with other low-energy gamma sources may appear in the spectrum [74].

2.1.2 Image Processing

As presented in Section 2.1.1, ideal γ-ray imaging systems transform all the detected electromagnetic radiation produced by its interaction with matter (or detector) into measurable electric signals like voltage pulses that will eventually form an image. The amount of energy deposited and its location on a plane is obtained through beam directionality, conversion of radiation into visible light, and light enhancement; therefore, the pulses will go through digital signal processing for noise treatment, resolution or quality improvement and image reconstruction.

Reconstruction algorithms have their basis in the Radon Transform, a formulation derived in 1917 by J. Radon, with the purpose of recovering a function in any dimension from its integral form to a lower dimension [77]; hence, the inverse of the Radon Transform demonstrates that a 3D image can be composed of several two-dimensional (2D) projections. Nevertheless, several methods have been developed to overcome limits and complications characteristic of the design like the performance and image quality. Some examples are Fourier's Reconstruction, Filtered Back-Projection, and Radon Reconstruction. In this section, an overview of basic mathematical formulations and approaches is provided for an understanding of the data treatment and analysis that lead to image reconstruction. It is important to mention that, overall, two types of imaging can be performed: structural imaging and functional imaging. In structural imaging, transmission coefficients are obtained and used to analyze the internal structure of a sample; this method is commonly used in CT, where the sample is irradiated by an external source. On the other side, functional imaging is focused on the activity provided by the already radioactive sample, where the emission of photons within a particular time is collected to study the changes or behavior of the radioactive substances (typically employed in PET and SPECT) [78]. Both methods will be mentioned in this thesis since some reconstruction techniques are more suitable than others to obtain each imaging parameter.

Image Reconstruction

A signal carries data information, generally in the form of time-varying voltage, about the relationship between one parameter and another, producing a continuous signal. However, since the signal is processed or passed from a physical to a digital parameter, the parameters have to be quantized, leading to the production of discrete signals [79]. In this case, the signal obtained is in the form of a voltage pulse or burst of voltage due to the fast decay of the radioactive elements that produce a fast rise of the PMT's output signals; these signals are treated later by a pre-amplifier and an amplifier to convert the current to voltage pulses, adjust pulse shapes and remove noise [80]. The output data or signals have a mathematical representation in one-dimension (i.e., pulses) and two-dimensions (i.e., images), where delta functions, linear operations and integral forms are implemented for its processing and manipulation. For simplicity of this paper, Appendix A will review and present the mathematical tools for signal processing in one-dimension while this section presents the methodology used for image processing (i.e., two-dimensions) and basic concepts for the formation of images.

It has been stated that the process of image reconstruction requires the collection and treatment of some parameters characteristic of the object to be studied. These parameters contain all the necessary information to transform the physical input signal into digital images in 2D and 3D. Thus, it is desired to obtain sufficient data that allow decent image reconstructions. This means that the data obtained is always limited, and lack of information is an unavoidable situation. However, analytical and iterative reconstruction techniques are capable of compensating for these cases through mathematical formulations, where its limitations and strengths will be dictated by the system to be studied and the accessibility to ideal equipment. Overall, the distinction between these methods relies on the approaches used to reconstruct an image. While analytic systems propose a direct approach to image acquisitions, the iterative methods involve multiple steps and training of mathematical and computational systems [81]. In addition, analytical systems (sometimes combined with iterative systems) are usually employed in structural imaging due to their direct mathematical approach to the formation of an image [81] and, because radiation doses can be modified,

direct image quality enhancement is possible without extra computational work [82]. Meanwhile, iterative systems are preferred for photon statistics, beam spectrum and scattering because of its high spatial resolution and low noise, compared to analytical systems [82].

Analytical Reconstruction

Analytical reconstruction processes are the most common methods used in image processing due to their simplicity and direct application. This method is based on transforms or mathematical inversions of an object cross-sectioned and represented in a plane-xy. It is said that analytical reconstructions are yield efficient but due to their mathematical approximations, the output image may be blurred [83]. Some mathematical approaches are the following:

- **Fourier Transform**

  In image processing an image is considered to be a two-dimensional signal. Thus, following the same structure as Appendix A, let us define an arbitrary picture f and an operator O. And the notation $O[f]$ will represent the line operator O applied to an image f, if

  $$O\left[af + bg\right] = aO\left[f\right] + bO\left[g\right] \tag{2.13}$$

  is valid, considering a and b as constants, and f and g any picture. Therefore, it can be said that a picture is formed by a set of pictures, or a sum of point sources. The output of f can be determined by knowing the operator's output for an input of a point source, where the response due to a point source is a point spread function of O [84]. If the point spread is invariant then the function is independent of its location. These sums of point sources are finite and show non-uniform characteristics for non-zero values. Thus, to achieve an equal intensity (or brightness), these values must increase every time [85].

Moreover, let us define a sequence of pictures (or sum of point sources) with the function $\text{rect}(x, y)$ of the form (for the 1D version, see Appendix A)

$$\text{rect}(x, y) = \begin{cases} 0, & \text{elsewhere} \\ 1, & \|x\| \leq \frac{1}{2} \text{ and } \|y\| \leq \frac{1}{2} \end{cases} \tag{2.14}$$

with a representation shown by Figure 2.8.
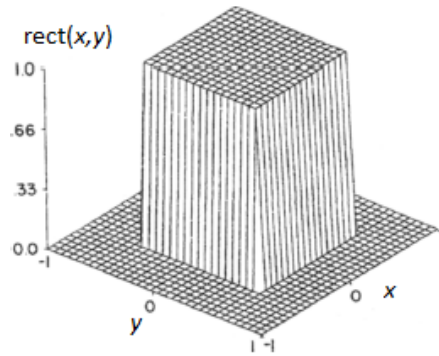
FIGURE 2.8: Two-dimension representation of function $\text{rect}(x, y)$ to show the Dirac delta behavior over the function, where the δ is given by the height of the function [86].

This graph is defined by

$$\delta_n(x, y) = n^2 \text{rect}(nx, ny), \tag{2.15}$$

where $n = 1, 2, \cdots$, and $\delta_n = 0$ outside of the x and y limits with n^2 has a constant value. Therefore, its height is denoted by

$$\int\limits_{-\infty}^{\infty}\!\!\!\int \delta_n(x, y)\, dx\, dy = 1. \tag{2.16}$$

In the previous equation, $n \to \infty$ and, as a consequence, δ_n has no limit. However, denoting one using the definition of Dirac's delta δ is convenient. Thus, $\delta(x, y) = 0$ for every (x, y) except $(0, 0)$, which is infinite, and $\delta(-x, -y) = \delta(x, y)$.

Additionally, because of the particular characteristics of the delta function, properties like *sifting* can be explained. Furthermore, let us define a general function $g(x, y)$ continuous at x and y, and

$$\int\limits_{-\infty}^{\infty}\!\!\!\int g(x, y)\delta(x - \alpha, y - \beta)\, dx\, dy = g(\alpha, \beta) \tag{2.17}$$

where δ is shift by (α, β) (i.e., $\delta(x - \alpha, y - \beta)$), and this property will measure the value of $g(x, y)$ at the point (α, β) [87].

Another property useful for smoothing processes is called *convolution* and is developed for shift-invariant operations (i.e., a shift for the independent variable of the input signal will correspond to a shift in the output signal) [88]. This property is denoted by $f * h$ and represented with the integral

$$g(x, y) = \int\limits_{-\infty}^{\infty}\!\!\!\int f(\alpha, \beta)h(x - \alpha, y - \beta)\, d\alpha\, d\beta. \tag{2.18}$$

In the previous equation, g is the product of two functions f and h, where $h(\alpha, \beta)$ is rotated $180°$ respect to the origin and shifted by (x, y) along the x and y directions. Additionally, the convolution property is commutative, meaning that $f * h = h * f$ [89]. This property can be proved with Equation 2.18 but will be omitted in this paper.

So far, it has been demonstrated that images can be defined in spatial coordinates $f(x, y)$. Nevertheless, alternative representations provide variety and simplification on formulae manipulation. For instance, Fourier Transforms allow image definition through its frequency, along with easy conversion between spatial and frequency domains without information loss [90]. Following the same strategy as Appendix A, an overview of the principal Fourier equations and properties will be provided; however, proof and derivations are omitted in this paper.

Let us define a spatial function $f(x, y)$ and its Fourier Transform $F(u, v)$ defined in the frequency domain, where u and v are described in terms of

cycles per unit length and known as spatial frequencies. Notice that a different terminology is used for the one-dimension notation. Despite this, conversion between annotations is possible by implementing $f = u = v = 2\pi\omega$ where f is the frequency and ω is the angular frequency in units of radians per unit of length [86]. So, the continuous Fourier Transformation in 2D will be stated by

$$F(u, v) = \iint\limits_{-\infty}^{\infty} f(x, y)e^{-j2\pi(ux+vy)} \, dx \, dy, \qquad (2.19)$$

where $j = \sqrt{-1}$ is the imaginary number, and the complex exponential represents the real (i.e., cosine function) and imaginary (i.e., sine function) components of the image. Thus, each component will depicture a pattern (e.g., a scale of grey or spectrum bands of light intensity data) parallel to its axis that goes through its respective spatial frequency. So for every value taken by u and v between 0 and ∞, a different spatial period in any direction on the pattern will be seen [90].

Additionally, using the previous equation, we can define a Fourier Transform expression for Equation 2.15. If $f(x, y) = \text{rect}(x, y)$, and solve for Fourier Transform, it will result on

$$F(u, v) = \frac{\sin \pi u}{\pi u} \frac{\sin \pi v}{\pi v}, \qquad (2.20)$$

with a representation given by Figure 2.9.

If a change of variable is applied to Equation 2.15 of the form $x' = nx$ and $y' = ny$, the Fourier Transform changes to $(1/n^2) \, \text{sinc}(u/n, v/n)$. Because the limit of this expression is the Fourier Transform of Dirac delta δ, when $f(x, y) = \delta(x, y)$ the Fourier Transform will be

$$F(u, v) = \lim_{n \to \infty} \text{sinc}(u/n, v/n) = 1. \qquad (2.21)$$
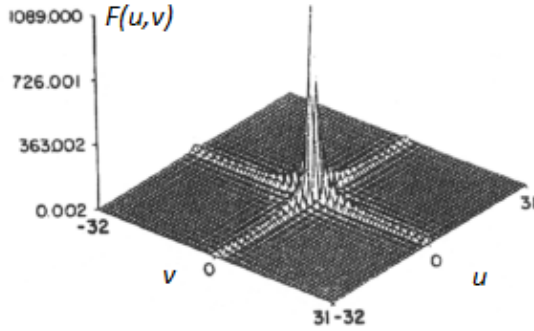
FIGURE 2.9: Representation of Fourier Transform $F(u,v)$ applied to the function $\text{rect}(x,y)$ where the terms u and v are in the spatial frequency domain, and the height of the graph will be defined by Dirac delta δ [86].

Furthermore, if the inverse Fourier Transform (IFFT) is defined by

$$f(x,y) = \int\!\!\!\int\limits_{-\infty}^{\infty} F(u,v)e^{j2\pi(ux+vy)}\,du\,dy, \qquad (2.22)$$

which is seen as a periodic linear combination of the patterns, while $F(u,v)$ acts as a weighting factor to measure the contributions of each component to the total sum. Thus, $F(u,v)$ is called the frequency spectrum of $f(x,y)$, and Equations 2.20 and 2.22 represent the Fourier Transform pair [91].

Useful image processing properties can be defined with 2D Fourier Transforms like linearity, scaling, shifting, rotation by an angle, rotational symmetry, 180° rotation, convolution, Parseval theorem, and others; however, only a few properties will be mentioned and explained in this thesis. In these formulations, the Fourier Transform of a function $f(xy,y)$ can be denoted by any of the following notations $F\{f\} = F\{f(x,y)\} = F(u,v)$.

Linearity: The Fourier Transform of a weighted sum formed by two sources is equal to the weighted sum of their individual transforms [92].

$$F\{af_1(x,y) + bf_2(x,y)\} = aF_1(u,v) + bF_2(u,v) \qquad (2.23)$$

Scaling: If a function, or signal, is spatially expanded by an α factor, then the spatial frequency will be compressed by the same factor in its Fourier Transform [91].

$$F\{f(\alpha x, \beta y)\} = \frac{1}{\|\alpha\beta\|}F(\frac{u}{\alpha}, \frac{v}{\beta}). \qquad (2.24)$$

Shifting: The product of a spatial domain signal $f(x, y)$ by an exponential with frequency domain, causes a shift in the frequency spectrum by spatial frequency factors u_0 and v_0 [92]

$$F\{e^{j2\pi(u_0 x + v_0 y)}f(x, y)\} = F(u - u_0, v - v_0), \qquad (2.25)$$

and for the spatial domain

$$F\{f(x - \alpha, y - \beta)\} = F(u, v)e^{-j2\pi(u\alpha + v\beta)}. \qquad (2.26)$$

Rotation by any angle: If the Fourier Transform is expressed in polar coordinates $F(\omega, \phi) = F\{f(r, \theta)\}$, and the function, or signal, is rotated by an α angle [86], then

$$F\{f(r, \theta + \alpha)\} = F(\omega, \phi + \alpha). \qquad (2.27)$$

Convolution: The convolution of two spatial domain functions is the product of their Fourier Transforms in the spatial frequency domain [93]

$$\int\!\!\!\int_{-\infty}^{\infty} f_1(\alpha, \beta)f_2(x - \alpha, y - \beta)\, d\alpha\, d\beta = F_1(u, v)F_2(u, v), \qquad (2.28)$$

and the convolution in the spatial frequency domain is

$$Ff_1(x, y)f_2(x, y) = \int\!\!\!\int_{-\infty}^{\infty} F_1(u - s, v - t)F_2(s, t)\, ds\, dt. \qquad (2.29)$$

Finally, to define the Finite Fourier Transforms (FFT) in 2D, let us introduce $f(m, n)$ as the samples of the function $f(x, y)$. So,

$$F(u, v) = \frac{1}{MN} \sum_{m=0}^{M-1} \sum_{n=0}^{N-1} f(m, n) \exp\left[-j2\pi \left(\frac{mu}{M} + \frac{nv}{N}\right)\right] \qquad (2.30)$$

has the spatial frequencies values of $u = 0,\ 1,\ 2,\ \cdots,\ M - 1$ and $v = 0,\ 1,\ 2,\ \cdots,\ N - 1$. And the Inverse Finite Fourier Transform (IFFT) is

$$f(m, n) = \sum_{u=0}^{M-1} \sum_{v=0}^{N-1} F(u, v) \exp\left[j2\pi \left(\frac{mu}{M} + \frac{nv}{N}\right)\right] \qquad (2.31)$$

for spatial domain values of $m = 0,\ 1,\ 2,\ \cdots,\ M{-}1$ and $n = 0,\ 1,\ 2,\ \cdots,\ N{-}1$.

Additionally, the convolution of two arrays can be formulated as a multiplication of the Fourier Transforms of the functions $f(m, n)$ and $d(m, n)$, and it is obtained through the cyclic convolution expression defined by

$$g(\alpha, \beta) = \frac{1}{MN} \sum_{m=0}^{M-1} \sum_{n=0}^{N-1} f(\alpha - m, \beta - n) d(m, n) \qquad (2.32)$$

where $\alpha = 0,\ 1,\ 2,\ \cdots,\ M{-}1$ and $\beta = 0,\ 1,\ 2,\ \cdots,\ N{-}1$, and their respective $f(m, n)$ and $d(m, n)$ functions are valid [86]. Thus, the previous equation stated in terms of their Fourier Transformations $F(u, v)$ and $D(u, v)$ with frequency domain is

$$g(\alpha, \beta) = \sum_{u=0}^{M-1} \sum_{v=0}^{N-1} F(u, v) D(u, v) exp\left[j2\pi \left(\frac{\alpha u}{M} + \frac{\beta v}{N}\right)\right]. \qquad (2.33)$$

- **Radon Transform**

  As mentioned, analytical methods are commonly used in structural imaging by obtaining the transmission coefficients necessary to quantify the number of rays that pass through a material. Thus, the goal of transmission tomography is to determine the density distribution of an attenuating medium [94]. A

long-time used reconstruction method is the Radon Transform, since it defines the total density as a function along a line, that will be part of a set of multiple density functions, used to make projections of an object [95]. Therefore, let us assume we have a sample that occupies a defined location in space (x,y,z), and this object is constantly irradiated by a beam of γ-rays (or x-rays). Since these rays do not have mass nor charge, they are not influenced nor altered by magnetic or electric fields; therefore, their trajectory will generally be in the shape of a straight line [56]. For simplicity, let us study only an area, or cross-section, of the sample which will be defined in a 2D or (x, y) plane. As mentioned, in this sample several straight lines are created and can be represented with the slope equation $y = mx + b$ or the point (m, b), where m is defined as the slope of the rect and b is its intersection point [96]; however, vertical lines are not considered in this type of formulation. Therefore, a point-normal form of a plane is more suitable for this situation where the line can be described by a point on a plane, that this line is traversing, and a normal vector analogous to the slope [97], see Figure 2.10.
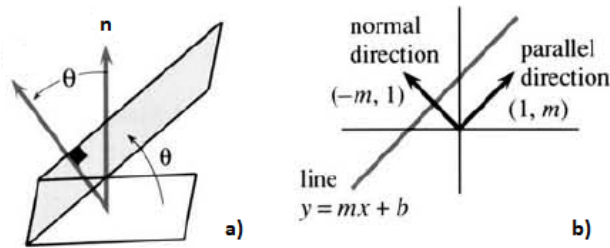
FIGURE 2.10: Figure a) represents a normal vector **n** with an angle aperture of θ in respect of a plane, and Figure b) pictures a normal vector with a line parallel to it over a plane, along with a representation of a line that traverses two points in a plane with its respective mathematical expression [97].

As depicted in part **b)** of this figure, there is an angle θ between the plane and the normal vector **n** with a possible aperture between 0 and 2π. The line at an angle θ is perpendicular to l, which intersects it at some point $(t \cos \theta, t \sin \theta)$ for any real number of t.

Since we want to write an equation for this line that is described in a three-dimensional plane, it is necessary to "flatten out" the surface or express its state as the function of independent parameters. This process is called parametrization [98]. Let us define a unit vector (i.e., a vector with a unitary length) as $(-\sin\theta, \cos\theta)$ perpendicular to the point $(\cos\theta, \sin\theta)$. Every point l will have the form $(t\cos\theta, t\sin\theta + s(-\sin\theta, \cos\theta))$, and the line can be expressed in terms of $x(s)$ and $y(s)$ for any number of s between $(-\infty, \infty)$.

Moreover, let us define an arbitrary point (x, y) in the plane that can be expressed with θ, t and s values in the form of

$$
\begin{aligned}
x(s) &= t\cos\theta - s\sin\theta \\
y(s) &= t\cos\theta - s\sin\theta
\end{aligned}
\tag{2.34}
$$

and with the solutions

$$
\begin{aligned}
t &= x\cos\theta + y\sin\theta \\
s &= -x\sin\theta + y\cos\theta.
\end{aligned}
\tag{2.35}
$$

Since we are taking the Radon transform of multiple lines at different angles θ, we can obtain multiple density functions of our sample [95] and by integrating each function, a projection through the object can be formed. Therefore, to represent the object in 2D, let us define the function $f(x, y)$ and its integral over the line as

$$
\int_l f(x, y) = \int_{-\infty}^{\infty} f(t\cos\theta - s\sin\theta, t\cos\theta - s\sin\theta)\, ds,
$$

or if we denote $P_\theta(t) = \int_l f(x, y)$ and use the delta function, we obtain the following formulation

$$
P_\theta(t) = \iint\limits_{-\infty}^{\infty} f(x, y)\delta(x\cos\theta + y\sin\theta - t)\, dx\, dy
\tag{2.36}
$$

Conversion Table	
Cartesian Coordinates	Polar Coordinates
$t = \sqrt{x^2 + y^2}$	$x = t\cos\theta$
$\theta = \tan^{-1} y/x$	$y = t\sin\theta$

TABLE 2.1: Conversion table for Cartesian and Polar coordinates where the values x and $y \in (-\infty, \infty)$, $t \geq 0$, and $\theta \in (-\pi, \pi)$ [100].

where $P_\theta(t)$ is the Radon transform of the function $f(x, y)$ and this value represents the measurements obtained by the detection device. This equation, where $P_\theta(t)$ has a constant θ, represents a combination of parallel ray integrals which is the simplest projection possible since it is formed by the addition of a set of line integrals [86].

As mentioned, to produce projections, it is necessary to compile or integrate a function f along a line. This function represents the density distribution of the attenuating medium while the line depends on t and θ values. The values act as input and the integral of f along different lines as the output, this process is the Radon transform which is denoted by $\mathcal{R}$ [99]. The transform can be applied to a variety of functions where, if we define a function f in a plane (x, y), the following expressions are valid $\mathcal{R}(f) = \mathcal{R}\{f(x, y)\} = \mathcal{R}f$ for any real number of (t, θ), in Polar coordinates, and with the equation

$$\mathcal{R}f(t, \theta) = \int_{s=-\infty}^{\infty} f(t\cos\theta - s\sin\theta, t\sin\theta + s\cos\theta) \, ds. \tag{2.37}$$

To visualize the Radon transform, it is useful to convert the Polar coordinates t and θ to Cartesian or Rectangular coordinates by using the Conversion Table 2.1.

Moreover, the values obtained from the transformation are related to a level of brightness for a continuum of grey values where 0 is black, 0.5 is neutral grey and 1 is white. This graph or type of visualization is a sinogram, and it depicts all the projections produced through different angles organized in a 2D image. The name is due to a sine wave resulting from the Radon transform

of an off-center point source and suggested by the symmetry $\mathcal{R}f(-t, \theta + \pi) = \mathcal{R}f(t, \theta)$ [101].

To construct a desired image using the Radon transform it is necessary to obtain all the information required by the processes. But scanning machines and imagers are only capable of providing a finite set of values. However, mathematical approximation models can be applied to address this lack of information. So, overall, there are only two cases to consider: 1) when the object is known, or 2) when the object is unknown. Nevertheless, in reality, we do not know with accuracy the resultant image for any case, and errors may occur in the data collection process [69]. Therefore, applying, testing and comparing imaging algorithms to known samples can provide feedback and a basis to locate inaccuracies and disparities between methods applied and images produced [102]. A solution commonly used in image reconstruction is to utilize a standard test image defined and constructed through a mathematical phantom; a process first introduced in 1974 by Shepp and Logan while trying to study the human brain [86]. This model or image test is carried out by choosing a known subject whose internal configuration can be structured through mathematical equations so no errors result in the data collection process. While reconstructing the image, the errors will be due to the algorithm [101]. Thus, this method tests the employed algorithm's capabilities to process and treat the data from the proposed phantom. The design of this mold consists of defining elliptical or square regions with a constant parameter on each region [86]. In this case, let us assume a constant density distribution of an attenuating medium where discs have been defined to denote these regions and, by using image processing properties like linearity, shifting and re-scaling we can obtain values for the Radon transform. This is done through the definition of quadratic expressions for x and y, and the determination of the lines l intersection [101]. The specifications of these algorithms are not mentioned but can be further revised in Feeman [101, Ch. 2]. Moreover, phantom and sinogram plots can be obtained with the exact formulas for the Radon transform of these phantoms, which are determined by the addition of the

attenuation coefficient functions of the different regions that conform the phantom (see Figure 2.11) [95].
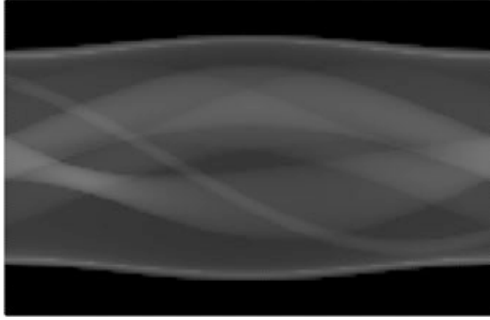
FIGURE 2.11: Sinogram of a phantom with elliptical regions defined by the equation $\frac{\hat{x}^2}{a^2} + \frac{\hat{y}^2}{b^2} = 1$ [101].

However, this paper is focused on emission tomography techniques, where the samples emit radiation in the form of γ-rays. The samples have this ability due to the insertion of radioactive materials into the system or by natural means. In medical procedures, radiation in a biological system is caused by the ingestion of radiopharmaceuticals. In industrial processes, it is caused by the injection of radioactive substances that act like tracers. While in nuclear fields, the radioactive substance is the sample itself, which is encapsulated in special containers to preserve safety and security measures and regulations. Therefore, in the analysis process of energy emission, the location and concentration of the isotope is determined; however, since the interaction between photons (emitted by the sample) and the medium is inevitable, energy will be lost in the detection process; thus, attenuation from this medium must be also considered. Hence, let us analyze this situation for a γ-ray emitted at a point (x_0, y_0) that travels in a straight line l until it reaches the detector. Following the notation previously used, let us define the parameter $s_0 = s$, so our parametrization values could be denoted by $(x, y) = (t \cos\theta - s \sin\theta, t \sin\theta + s \cos\theta)$ for an $s \geq s_0$. And, using Beer's law (i.e., a sample concentration is related to the measured intensity of an isotope [103]), the attenuation of this photon can be expressed by $\mathcal{A}_\mu(x_0, y_0, t, \theta) = \exp\left[-\int_{s \geq s_0} \mu(x, y) \, ds\right]$ and it is evaluated

through the line l. Thus, for a function f that represents a concentration in a point (x, y) with an attenuation coefficient of μ, its attenuated Radon transform will be

$$\mathcal{R}_\mu f(t, \theta) = \int_l \mathcal{A}_\mu(x, y, t, \theta) f(x, y) \, ds, \tag{2.38}$$

where t and θ are real numbers, and if the attenuation coefficient of the medium is negligible (i.e., $\mu(x, y) = 0$), then $\mathcal{A}_\mu = 1$ and $\mathcal{R}_\mu f = \mathcal{R}f$ as stated on Equation 2.37 [101]. So, the inversion of the attenuated Radon transform will allow the reconstruction of the isotope's activity distribution on the sample [94].

- **Back-Projection Transform**

  The Backprojected or Back-Projection Transform is considered one of the most simple and fundamental bases of image reconstruction because, by considering the attenuation coefficients of a sample denoted as $f(x, y)$, it assumes a homogeneous distribution for $f(x, y)$ on the object, where the attenuation is equal from all the points along the path [104]. So, let us assume a point in the plane (x_0, y_0) where several lines, or γ-rays, pass through at different angles θ, and can be expressed with $t = x_0 \cos \theta + y_0 \sin \theta$ for any real number of x_0, y_0 and θ. For every beam that passes through that point, energy is lost and it will provide the attenuation coefficient of a sample $f(x_0, y_0)$, where its values will be given by the Radon transform $\mathcal{R}f(x_0 \cos \theta + y_0 \sin \theta, \theta)$, for every angle [101]. Therefore, to obtain the attenuation coefficient of this point, every line integral (or a path) must be accounted through the average value

$$\frac{1}{\pi} \int_0^\pi \mathcal{R}f(x_0 \cos \theta + y_0 \sin \theta, \theta) \, d\theta. \tag{2.39}$$

Moreover, if a function $h = h(t, \theta)$ in polar coordinates is defined, it can be said that its transform or back projection at a point (x, y) in Cartesian

coordinates is

$$\mathcal{B}h(x,y) = \frac{1}{\pi} \int_0^\pi h(x\cos\theta + y\sin\theta, \theta)\, d\theta. \tag{2.40}$$

Thus, by using the values of the projection angle and distance, the attenuation can be spread equally among a set of pixels along the beam path; so, the projection values are "backprojected" into a pixel grid [85]. The process is repeated for every projection and the values in each pixel are combined, or summed, over all the projections. The visualization of this process after several runs is a blurred star with a circular dense point that represents the spectral density of the sample [101], see Figure 2.12.
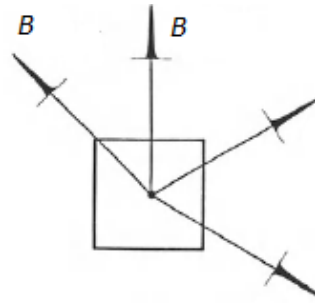
FIGURE 2.12: Backprojection functions B for different angles θ. Each contribution is integrated and, after several interactions, a blurred star-shaped image for a spectral distribution of the sample is shown [85].

Furthermore, combinations of these transformation theories can be implemented as additional methodologies for image processing. If the transformations are valid under a set of conditions, they can be employed in the following processes (this paper will only make mention of them):

Central Slice Theorem. In this theorem, the Fourier Transform and Radon Transform are used to obtain a relationship between a line and the projected image through the Fourier Transform in 2D of the image function at an angle θ [5].

Filtered Back Projection. This method can be used with Fourier and Radon transforms combined with Backprojection. It follows the same methodology as the back projection transform but, in this case, a set of filtered projections are used. This filtration is done by convolution filters, or a kernel, where the brightness value of a pixel becomes a function of an intensity-weighted average of the surrounding pixels, producing softer images [85][86].

Iterative Reconstruction

Iterative reconstruction algorithms are characterized by their multi-step reconstruction process. This method differs from the analytical reconstruction due to the initial discretization of the problem, which will delimit the system to a finite set of unknowns from a finite set of equations that can be solved by iterations [83]. Iterative methods provide a more defined and realistic model of the sample, they can simplify and take into account complex parameters in the formulation like photon attenuation or position-dependent resolution [86]. Additionally, the image noise is minimum in comparison to transformation techniques but, for every iteration, the noise increases [78]. Another important limitation is the high computational processing capacity needed to solve the system of equations. Iterative methods include algorithms like Algebraic Reconstruction Technique (ART) and Statistical Reconstruction, additional ART variations are also part of this classification like Simultaneous Iterative Reconstructive Technique (SIRT) and Simultaneous Algebraic Reconstruction Technique (SART), beside iteration methods like the Kaczmarz's method and the Method of Least Square.

- **Algebraic Reconstruction Technique (ART).**

   Iterative methods consider a finite amount of information from the beginning of the process, where an image is limited and constructed by a 2D grid arranged with pixels, or picture elements. Each pixel has a value taken from a scale in terms of a normalized maximum intensity. This variation of intensity represents the density or attenuation coefficient of the

FIGURE 2.13: Two-dimensional grid of $K \times K$ where every box represents a pixel with an assigned position and intensity value [101].

sample. Thus, let us define the grid $K \times K$ by enumerating each pixel box as depicted in Table 2.13, where the pixels will have a basis function of the form $b_1, \cdots, b_{K^2}$, and b_k is defined by

$$b_k = \begin{cases} 1 & \text{if } (x, y) \text{ is inside pixel } k \\ 0 & \text{if } (x, y) \text{ is not inside pixel } k \end{cases}$$

for $k = 1, 2, \cdots, K^2$. By assigning the intensity value x_k to the k-th pixel, the following expression can be stated

$$\tilde{f}(x, y) = \sum_{k=1}^{K^2} x_k \cdot b_k(x, y) \tag{2.41}$$

for each point (x, y) inside of the grid. And, by applying the Radon transform, the previous equation can be expressed in terms of polar coordinates with the form

$$\mathcal{R}\tilde{f}(t, \theta) = \sum_{k=1}^{K^2} x_k \cdot \mathcal{R}b_k(t, \theta). \tag{2.42}$$

The values $\mathcal{R}\tilde{f}(t, \theta)$ are the measurements given by the detection device for

a finite set of samples, or lines l, where every line has a t and θ value [101]. Therefore, Equation 2.42 can be rewritten as a system of equations where $\mathcal{R}\tilde{f}$ is the length of intersection of the line l with a pixel number k, and $r_{jk} = \mathcal{R}\tilde{f}(t_j, \theta_j)$ has the form

$$p_j = \sum_{k=1}^{K^2} x_k \cdot r_{jk} \tag{2.43}$$

for a $j = 1, \ldots, J$. The previous equation describes a set of J linear equations in K^2 unknowns $(x_1, \ldots, x_{K^2})$, since generally J and K^2 are of the 10^5 order, this system is large. Additionally, every transform will produce an equation and each pixel will correspond to an unknown (i.e., intensity value) but if there are more equations than unknowns, the system is overdetermined. And if there are more unknowns than equations, the system is undetermined [86]. Due to this, high demands on computational systems appear in this method, making this technique less viable for commercial systems.

Moreover, to find approximate solutions for the system of equations defined, different iteration methods are employed like Kaczmarz's method and least squares approximations.

Kaczmarz's Method.

This iteration method tries to approximate a solution to the system described in Equation 2.41 by expressing it in a matrix form $J \times K^2$, where r_i is the i-th row of a matrix A and p_i corresponds to the i-th coordinate vector $\mathbf{p}$. Thus, it can be written in the form $A\mathbf{x} = \mathbf{p}$ which is equivalent to $\mathbf{r}_i \cdot \mathbf{x} = p_i$ for $i = 1, \ldots, J$. This method produces a chain of vectors that will satisfy one $\mathbf{r}_i \cdot \mathbf{x} = p_i$ equation. In other words, describes an affine space (i.e., it generalizes the properties of a euclidean space where it is independent of distance and angle) [105]. In more detail, this process starts with an initial guess for $\mathbf{x}$ that we will call $\mathbf{x}^0$ and then assign it an intensity value $\mathbf{x}^{0,0} = \mathbf{x}^0$. By determining

the vector $\mathbf{x}^{0,j-1}$ we can define a projection for $\mathbf{x}^{0,j-1}$ of the form

$$\mathbf{x}^{0,j} = \mathbf{x}^{0,j-1} - \left(\frac{\mathbf{x}^{0,j-1} \cdot \mathbf{r}_j - p_j}{\mathbf{r}_j \cdot \mathbf{r}_j} \right) \mathbf{r}_j. \qquad (2.44)$$

Since the matrix has J rows, the vector $\mathbf{x}$ will have $\mathbf{x}^{0,1}$, $\mathbf{x}^{0,2}$, ..., $\mathbf{x}^{0,J}$ values. Then, the same process must be followed for the vector $\mathbf{x}^1$, and it starts by defining $\mathbf{x}^1 = \mathbf{x}^{0,J}$ and $\mathbf{x}^{1,0} = \mathbf{x}^1$, so the values $\mathbf{x}^{1,1}$, $\mathbf{x}^{1,2}$, ..., $\mathbf{x}^{1,J}$ will also be obtained. These multi-steps are repeated for every $\mathbf{x}$ until the desired output is achieved. Because the convergence is slow, a lot of iterations are necessary to achieve a decent approximation. However, if the system has no solution, then the output pattern could be static or chaotic [101].

- **Statistical Reconstruction.**

  The main characteristic of this method is its noise treatment and control with statistical functions to provide image quality. In image processing, the term noise is given to the presence of components that are not part of the original set-up or, in terms of statistical behavior, it represents measurements of fluctuations caused by random processes [85]. Therefore, let us redefine the matrix interpretation for Equation 2.43 of the form $\mathbf{p} = A\mathbf{x} + \bar{\mathbf{b}} + \mathbf{n}$, or

  $$p_i = \sum_{j=1}^{I} A_{ij} x_j + \bar{b}_i + n_i \qquad (2.45)$$

  where the extra terms $\bar{b}_i$ is an additive noise-free contribution and n_i is the noise contribution for an $i = 1, \ldots, I$. Thus, in this case, it is desired to find $\mathbf{x}$ values with statistical models for $\mathbf{n}$. While dealing with noise, it is difficult to obtain an exact reconstruction; therefore, these problems are treated as optimization tasks [83]. If the behavior of the noise is known, Bayesian statistics can be applied (i.e., model of statistical inference where the prior knowledge of the event might lead to the probability of occurrence of the same event) [106]. So, by using the Least Square method, it is possible to find approximations for the $\mathbf{x}_j$ values, assuming that the noise has a Gaussian

behavior with a mean zero and fixed standard deviation σ that does not depend on the position [83]. Thus, the probability function to measure the noise value p_i, that has an expected value of $\sum_j A_{ij}x_j + \bar{b}_i$, is of the form

$$\mathcal{P}_{LS}(p_i | \sum_j A_{ij}x_j + \bar{b}_i) = \frac{1}{\sqrt{2\pi}\sigma} \exp\left[-\frac{\left[p_i - \left(\sum_j A_{ij}x_j + \bar{b}_i\right)\right]^2}{2\sigma^2}\right]. \quad (2.46)$$

And the probability function to measure the complete sinogram noise $\mathbf{p}$ is

$$\mathcal{P}_{LS}(\mathbf{p}|\mathbf{x}) = \mathbf{P}_L S(\mathbf{p}|A\mathbf{x} + \bar{\mathbf{b}}) = \prod_i \mathbf{P}_L S(p_i | \sum_j A_{ij}x_j + \bar{b}_i). \quad (2.47)$$

By maximizing the logarithm of $\mathcal{P}_{LS}$, the objective function L_{LS} are

$$\begin{aligned}
L_{LS} &= -\sum_i \left(p_i - \left(\sum_j A_{ij}x_j + \bar{b}_i\right)\right)^2 \\
&= -\left(\mathbf{p} - \left(A\mathbf{x}' + \bar{\mathbf{b}}\right)\right)'\left(\mathbf{p} - \left(A\mathbf{x}' + \bar{\mathbf{b}}\right)\right)
\end{aligned} \quad (2.48)$$

where the prime symbol indicates transpose. And, the first derivatives respect p_i to zero for all j is

$$\begin{aligned}
A'\left(\mathbf{p} - A\mathbf{x} - \bar{\mathbf{b}}\right) &= 0 \\
\mathbf{x}\left(A'A\right)^{-1} A'\left(\mathbf{p} - \bar{\mathbf{b}}\right)
\end{aligned} \quad (2.49)$$

where $A'A$ is non-singular, A is a discrete projection and A' is its discrete back-projection. Thus, $A'A$ will behave as a blurring filter and, for ideal parallel-beam projection, the expression is shift-invariant and equivalent to the convolution process. Due to this, $(A'A)^{-1}$ can represent the shift-invariant deconvolution and be calculated with Fourier Transforms [83]. However, direct inversion of $A'A$ is not convenient; thus, iterative optimization is needed to find the values of Equation 2.48. The iteration algorithm can be given by the steepest gradient ascent

$$p^k \approx -\mathbf{H}^{-1}\Delta L(\mathbf{x}^{k-1}) = -\mathbf{H}^{-1}\mathbf{d}^k, \quad (2.50)$$

where **H** is the Hessian and represents the matrix of the second derivative of L [107], and its elements can be calculated with

$$H_{jk} = -\sum_i A_{ij} A_{jk} \approx -(A'A)[j,k].$$ (2.51)

2.1.3 Gamma-Emission Tomography

In the previous section, it was emphasized the importance of collecting sufficient data of the object of study for its processing and manipulation through mathematical methods, which results in significant pulses or images that contain all the information of its internal and external features. Following this, as mentioned, these natural signals (i.e., signals obtained from the interaction of radiation with matter) are transformed into quantitative form by imagers composed of a directional system (i.e., a collimator), and a detection device. These imagers are arranged in respect of a sample under specific configuration features to ensure maximum data capture. Overall, the configuration will depend on the object and purpose of the study. The imager's function is to capture signals; thus, the system configuration needs a source capable of emitting them, and the class of source will depend on the characteristics and conditions of the study. For example, if the sample is a natural radiation emitter, the source will be the sample itself but, if the sample is non-radioactive, an external ionizing energy source can be used. In both cases, configurations and sample-source motion vary; additionally, equipment and material specifications change in relation to the penetration characteristics of the radioactive source used. In this case, the focus is on samples that emit radiation in the form of γ-rays due to their high-penetration and low scattering attributions, in addition to their constant release during and immediately following the fission process in nuclear systems, and great adaptability in medical and industrial fields by smoothly controlling their range of emission and directionality. Therefore, in this section, three different techniques commonly used for γ-ray emission tomography are presented (i.e., Tomographic Gamma Scanning (TGS), Single Photon Emission Computed Tomography (SPECT) and Limited-Angle Tomography (Laminography)), since it

has been made clear that cross-sectional study of a sample provides more accurate results in imaging processes.

Single-Photon Emission Computed Tomography (SPECT)

The SPECT system is one of the most common methods used in medical imaging for heart, brain and bone studies. And, recently used for fuel inspection in nuclear systems. However, its application is not as frequent as other imaging techniques due to attenuation problems that difficult the quantification of the isotope's distribution in the sample. Nevertheless, variations have been developed to compensate for these difficulties. As the name indicates, this technique measures photons, or γ-rays, emitted by a sample, using a gamma camera mounted in a special support and rotated between 180° and 360° around the sample [108], see Figure 2.14. Although, the most preferred configuration is positioning two cameras separated by 90°, to reduce exposure time and enhance image sensitivity [35]. Since not all samples naturally emit radiation, it is common to use radiopharmaceuticals (i.e., safe digestive agents containing radioactive substances) like thallium-201, iodine-123 and indium-111, in injectable or oral form, to study biological systems [30]; while radiotracers (i.e., chemical compounds where one or more atoms are replaced with radioisotopes) like 137-Cs/137m-Ba, 99-Mo/99m-Tc and 113-Sn/113m-I, in gas, liquid or solid form, are used to study industrial systems [109]. On the other hand, samples that naturally emit radiation can be found in nuclear systems, present in the vicinity of reactor vessels during power operation like Co-60 and Fe-59 (commonly produced by activation products in the structural components of the reactors) [110]. In recent years, variations of SPECT techniques have been employed in fuel behavior analysis to demonstrate cladding integrity during normal operations, irradiation time and accident performance in a power plant [111]. This is, due to the constant changes in fuel performance, a consequence of power production by fission processes, and the general interest to increase fuel efficiency and burnup [112]. Moreover, the isotopes contained in the sample will decay and emit radiation (from the sample's location) in the form of γ-rays, which will be detected by the gamma camera. As mentioned, this camera captures and

processes all the incoming data from the radioactive substances for conversion to measurable digital signals. These signals are later used and manipulated by mathematical methods to produce projections of the sample and reconstruct a 2D or 3D visualization. In this case, the activity or decay of the isotope is proportional to the concentration of the sample at that point; thus, the integral line will be represented by the γ-ray (see Section 2.1.2). And, if the detector or imager device is moved adjacently, another ray parallel to the prior one can be determined [86]. Therefore, rotations of the device or sample are necessary to generate the projections. Moreover, reconstruction techniques for emission tomography are more complex than the ones employed in transmission tomography. This is due to extra considerations in the emission models like isotope distribution in the sample and attenuation of γ-rays; while in transmission models only solutions for the attenuation coefficient are necessary. Therefore, a combination of analytical and iterative reconstruction methods is commonly employed to treat attributes like the attenuation coefficient. Usually, the Filtered Back-Projection (FBP) is used as a deterministic model and the Statistical relationships like the Poisson mass distribution function are used to consider and treat stochastic effects [78]. Nevertheless, individual applications of the reconstruction methods are valid in SPECT systems since each method, depending on the object of study, provides essential information about the object. As seen in [113] where, by comparing FBP and Maximum Likelihood Expectation Maximization (MLEM) reconstructions over a fuel assembly, it has been shown that FBP has high image intensity with low image resolution while MLEM has a low intensity but better quantitative analysis, and both of their reconstruction time is comparable. Additionally, combinations of traditional (i.e., FBP) and modern machine learning methods (i.e., Neural Networks (NN)) have allowed superior correction of scattering and collimator effects while studying hepatic scans as demonstrated by Dietze *et al.* [114]. Generally, in SPECT configuration, the gamma camera moves around a static sample to obtain different angular directions and produce images in vivo of radioactive distributions [83]. This movement must be controlled and adequate since too fast or too slow detection motion around the sample may create errors in the projections as in [115]. And,

as mentioned, positioning of up-to three gamma cameras in an assemble is possible, but there is concern for truncation in the projections; thus, acute and wide angular coverage can be applied to overcome this [35].
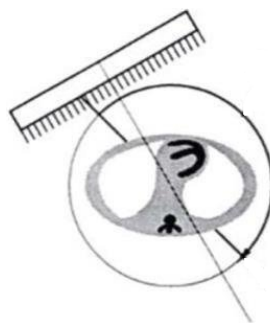
FIGURE 2.14: Diagram of a Single-Photon Emission Computed Tomography (SPECT) configuration, where the rectangular area represents a gamma camera that rotates between 180° and 360° around the circular sample [116].

Tomographic Gamma Scanning (TGS)

The Tomographic Gamma Scanning (TGS) technique is considered a next generation type of tomographic gamma scanner, due to its combination of 3D characteristics for SPECT methods, which handle isotope distribution and attenuation coefficients, and high-resolution gamma-ray spectrometry. Therefore, it shares several configuration and data treatment features with SPECT techniques. The TGS has its origin around 1990 in Los Alamos National Laboratory, as an attempt to assay waste drums from a non-homogeneous approach [117]. The configuration proposed consisted of a 75-Se gamma source (used to obtain transmission coefficients), a high-resolution germanium detector (HPGe), and a mobile sample (waste drum) with a rotation of 3 rpm and position translation [118], see Figure 2.15. This technique combines emission and transmission tomography methods to overcome errors obtained in traditional Segmented Gamma Scanning (SGS) (i.e., a technique that analyses emissions from circular cylindrical discs) due to volume averages over the entire volume that led to not reliable estimations. Nevertheless, the sample (the waste drum)

contains isotopes like plutonium or uranium, whose gamma-rays are counted and mass estimation is obtained; these rays are detected by the HPGe detector and corrections are made to the count rates for the attenuation of the medium between the sample and the detector [118]. Furthermore, as studied by Mu *et al.* [119], more affordable detectors like NaI combined with a detection array of fan-beam have shown good responses to this technique; although, modifications on the collimator must be done to ensure uniformity of the γ-rays. As mentioned, this technique was developed to study waste drums, where the most common radioactive substances contained are 239-Pu, 235-U and 137-Cs, as the ones studied in [117] and [119]. Since this method is more sophisticated than SPECT, high performing reconstruction methods must be used. The first approaches used iterative reconstruction techniques, by combining ART for transmission coefficients and Expectation Maximization (EM) for attenuation coefficients [117]. Nevertheless, there is an interest in the development of alternative options that could improve positioning and activity accuracy, as done by Zheng *et al.* [120], and faster reconstruction times with high image quality in machine learning mechanisms, like in [121]. Finally, the versatility and accurate performance of iterative systems implemented on cross-sectional imaging techniques and, combined with the high penetrating characteristics of γ-rays in TGS systems, have encouraged other industrial fields to apply and explore image reconstruction methods that could improve Non-Destructive Testing (NDT) analysis. For instance, Haraguchi *et al.* [122] performed this type of analysis in a tall industrial distillation column through a traditional gamma camera approach and a TGS method, where the procedure not only exhibited possibilities of a 2D image reconstruction, but revealed malfunction in the columns that are difficult to observe in 1D scanning processes.

Limited-Angle Tomography

Laminography is a modified type of tomography technique usually seen as a generalization of a Computed Tomography (CT) method. It is commonly used for samples with large ratios or planar dimensions where the object's projections are obtained layer by layer. Most of the configurations involve a source, a detector
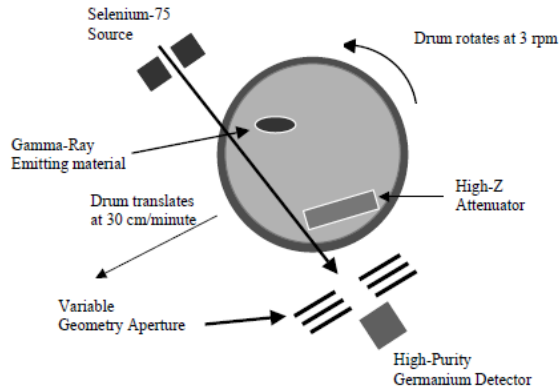
FIGURE 2.15: Tomographic Gamma Scanning (TGS) configuration, where a Se-75 source is used for transmission images while the γ-ray source is contained in a waste drum that rotates at 3 rpm; the detector is a fixed semiconductor made of germanium [118].

and a sample, however, attempts to modify this technique in order to be applied with an emission tomography approach that only consists of a detector and a natural or artificial radioactive source as in [123] have been recorded; in addition, different angles can be performed according to the necessities and objectives of the study. For instance, in the inspection of ultra-thin and small samples, it is convenient to maintain a static position of the object between the source and the detector, which can follow a circular motion to avoid blurring as in [124] whereas, in samples with large dimensions, a limited-angle tomography approach with a source and a detector performing a linear motion is better suited [125], see Figure 2.16. An x-ray source is typically used in laminography but, its polychromatic nature may cause beam hardening artifacts (i.e., when x-rays of low-energy are absorbed more than high-energy x-rays) in the images produced as in [126], thus a monochromatic beam is suggested to avoid this outcome. In other cases, for high-flux reactors or pulsed-neutron facilities, the use of neutron beams (or gamma-rays) is preferred due to their high-penetrating characteristics as in [127]. Since this method shares scanning features with CT, similar image reconstruction techniques can be employed where iterative methods like ART are used due to the high-quality images produced and the addition of "a priori" information [128]. Nevertheless, a combination of iterative algorithms and weight functions to

reduce artifacts on reconstructions as in [126], has produced better results than only implementing a direct imaging reconstruction process.
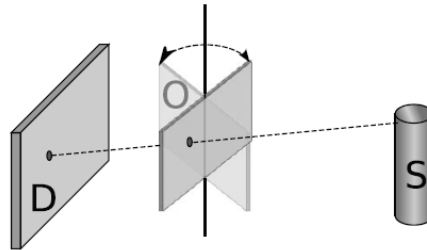
FIGURE 2.16: Limited-Angle Tomography or Laminography. The detector D and the source S can move in a linear trajectory around an object O that is inclined at an angle smaller than 90° [125].

It is known that CT is a well-established transmission imaging technique that reconstructs internal structures of objects by scanning them over a 360 degree ratio. But, as mentioned, this complete scan is not always feasible due to dimensional or positioning limitations; thus, a limited-angle tomography technique is considered a good approach to overcome these limitations by compromising data from acquisition angles and implementing more sophisticated reconstruction techniques. However, in nuclear systems or waste analysis, emission tomography is ideal to reconstruct emission (or activity) maps of the sample. Nevertheless, additional information like the medium attenuation coefficients and isotope distribution must be considered in the final analysis, which leads to extra computational work and scarce use as an imaging technique.

2.2   Objectives and Work Statement

It has been clear that since the discovery of x-rays (i.e., ionizing radiation and imaging technique), the curiosity of humanity to study the unexplored has no limits. The physical and measurable processes behind radiation permit a different perspective of known systems and allows the study of unknown systems, by using and exploiting the natural phenomena of radiation and its interaction with a medium. Chapter 2, has attempted to present and describe the physical processes

governing these events, along with the configuration and principles of quantifiable devices and methods that transform the phenomenon into significant measurable data for its analysis and interpretation. Since this knowledge could lead to descriptions of internal and external features of a body of interest, its development has permitted qualitative and quantitative advantages in science and engineering fields.

The most utilized tomographic techniques employ a transmission tomography approach to analyze a sample; however, for analysis of natural or induced radioactive samples, where attenuation is a consideration, like the radionuclides produced in a reactor core or fuel assembly, products of the irradiation process of the fuel and source of high energy gamma-rays and highly penetrating neutrons, this approach is not feasible nor accurate due to the limited position angles obtained in the scanning process. Therefore, the main goal of this thesis is to facilitate the data acquisition process in an emission tomography approach with a limited-angle imaging technique, since as seen in [123] for a fixed nuclear fuel configuration, high fidelity of the gamma-ray flux at central regions can be obtained utilizing this technique. Thus, applications for on-site data measurements of large objects are needed. In order to overcome the limitations encountered by on-site analysis of samples (e.g., space restrictions and/or mobility of the sample), a flexible yet accurate way of mounting that allows and facilitate the detector motion, without moving the detector itself (relative to the mount), around the sample with well-defined angles is proposed in this thesis.

As mentioned, avoidance of poor performance and human error, coupled with concerns of radiation exposure, leads to a preference for mechanical and self-reliant configurations. Thus, this thesis delineates and corroborates the feasibility of the structure support for a field-deployable detector device, that could provide flexible, accurate and stable means of motion to the detector during the tomographic scanning process. In order to delineate the support and its motions, a mathematical model must be developed to describe and define the object as a 3D figure that occupies a space in a coordinate reference system, where it can be represented by tangible and physical measurements; thus, a change on its original state will lead to a transformation or motion of the

structure that can also be represented by these quantities. Additionally, to corroborate the feasibility of the support and accuracy, a computational simulation of the proposed tomography system, as depicted in Figure 2.17, must be done to verify that the necessary motions can be performed by the support, in order to provide enough projections such that a sparse matrix reconstruction could be applied on further studies.
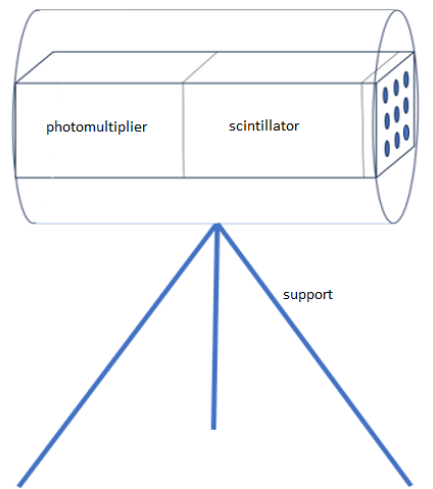
FIGURE 2.17: Proposed detector device layout represented by a gamma camera, that is conformed of a collimator placed in front of a scintillator detector and connected to a photomultiplier; which is mounted in a suggested tripod shape structure.

Chapter 3

Mathematical Model

As mentioned, the goal of this thesis is to delineate the support structure for a field-deployable detector device utilized in the analysis and inspection of samples with considerable dimensions; which, overall and at this stage of the study, consists of a movable type of gamma camera and a sample that radiates gamma-rays. In the attempt to achieve this goal, it is necessary to simplify and follow a process that will serve as guidance and support. This suggested method is the Engineering Design Process, which presents a series of steps to follow to solve a problem from an engineering point of view [129], see Figure 3.1. Since the main emission tomography system is constituted of two components (i.e., a detector and a sample) that can be seen and treated as separate elements for better organization and understanding of this project, the design process can be applied individually to these components without altering the final outcome. Notice that in this Chapter, the gamma camera is generally referred to as a detector device for generalization and practical purposes since the focus is on its motion and geometry. Nevertheless, in this thesis, only the delineation of a field-deployable detector device (i.e., a detector device and a support), which proposed layout can be seen in Figure 2.17, is realized in order to validate the support's feasibility as a form of motion of the detector that does not require any motion of the detector itself (relative to the mount). Therefore, to define and accurately represent the motion of the detector device and the support, a mathematical model must be done. The expressions obtained in this model are a result of the governing equations from the components (e.g., linear transformations for the motions and equilibrium forces that describe the static equilibrium state on the proposed layout), of sub-models like the definition of physical quantities and

their relation, and of assumptions and constraints given by the support shape and the required scanning motions around an object of interest [130].
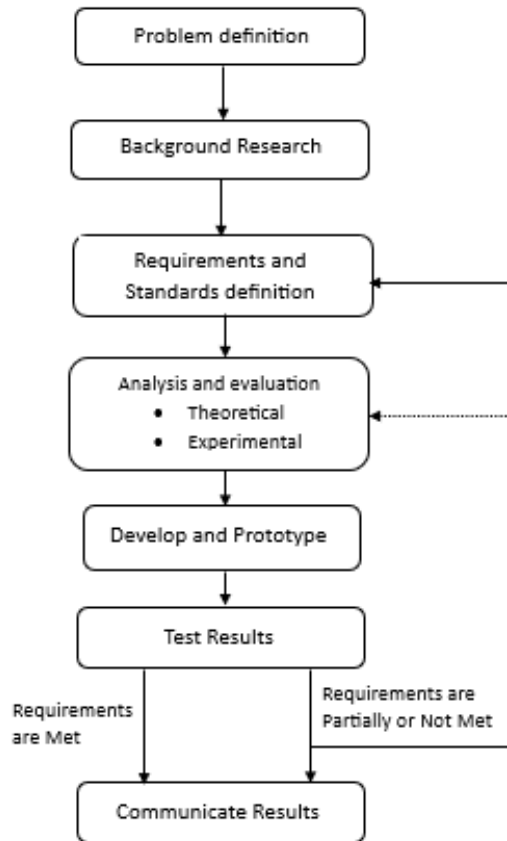
FIGURE 3.1: Workflow of a design process; see [129] for further details.

3.1   Detector Device

By following the design process, let us define the problem and requirements needed for the detector, which are stated in Table 3.1 (the background fundamentals can be reviewed in Chapter 1 and 2).

To comply with these requirements, an assembly of a cylindrical detector mounted on a movable base is proposed.   The device is desired to mimic a cross-sectional scanning motion (typically used in tomographic techniques), where

Stage	Specifications
Problem definition	Delineate a field-deployable detector device capable of capturing γ-rays of large samples.
Requirements	Detection of γ-rays. Self-reliant detector motion around the sample. Angular motion with respect to the center of the sample. Flexible and accurate detector motions.

TABLE 3.1: Definition of problem and requirements.

a detection device moves around a sample in order to get cuts or slices of the same sample; thus, to construct or follow a three-dimensional matrix of positional measurements for the detector, a complete or partial rotation around the sample must be performed. In this case, the base is composed of three stainless steel legs that have the capacity to support the detector, and to retract or elongate (see Figure 3.2).

Moreover, this section will be divided on three parts, according to the components of the field-deployable detector device as illustrated in Figure 2.17. Section 1) Head, covers the motions performed by the detector device or head of the support; section 2) Base, covers the motions of the support that has a three-leg stand structure; and section 3) Assembly, overviews the entire field-deployable detector device assembly (i.e., tripod and head of the tripod).

3.1.1 Head

The elements of the field-deployable detector assembly (see Figure 2.17), hereinafter referred to just as the assembly, can be represented through quantities with unvaried properties like the mass and length, and variables like the position and direction. In other words, they can be represented by scalars and vectors, where the latter one has a magnitude and direction, and is depicted by an arrow or a line [131]. As mentioned in Table 3.1, the head or detector of the assembly has the ability to perform a motion in the form of a circle around a fixed axis at a
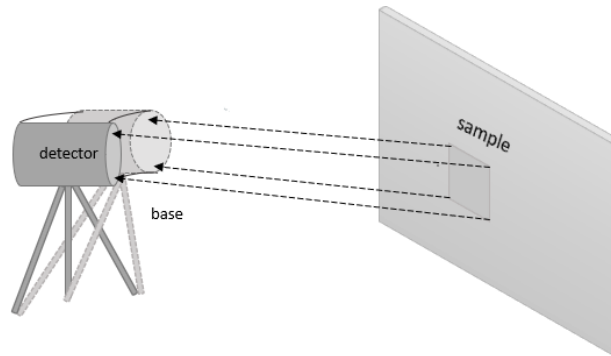
FIGURE 3.2: Suggested configuration of the field-deployable limited angle tomography system, which head or detector structure can be seen in Figure 2.17.

constant speed and its position will be constantly changing. Thus, it describes a uniform circular motion. This constant motion produces an acceleration that is directed to the "pivot" point or center point of the rotational system (or circular path), so there is a perpendicular force to this path, called centripetal force, and also directed to the center point [132]. Now, let us represent the detector device or head of the support in a plane with a vector $\mathbf{r}$, which is defined in a Polar coordinate system and uses the radial distance r and the angular direction θ of the detector to indicate its coordinates, see Figure 3.3.
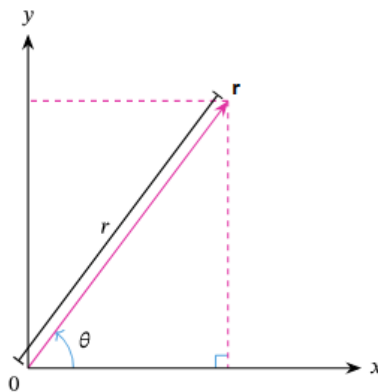
FIGURE 3.3: Definition of a vector $\mathbf{r}$ over a plane, where r is the length of the vector and θ is the direction angle [133].

If the detector $\mathbf{r}$ starts changing direction, then it is said that there is an angular displacement $\Delta\theta$ or rotation. But if every point that describes the detector changes

its position to a new one, then there is a shift in the origin of the coordinate system or a translation [100]; which is explained in more detail later in this thesis. As described in the previous chapter, this Polar coordinate system can be expressed in terms of Cartesian coordinates (x, y), where x and y represent a distance from a point; see Table 2.1 for conversion expressions and domains. Therefore, the rotation and translation of the detector can be explained in 2D and 3D Cartesian coordinates and be described by linear transformations.

A linear transformation is the mapping (i.e., the association of an element in a given set with another element in a different or same set) $\mathbf{V} \to \mathbf{W}$ between two vector spaces [84][131]. This space is determined by a set of elements or vectors and scalars that follow the operations of vector addition and scalar multiplication [84]. Thus, they satisfy the axioms for vector addition of associativity, commutativity, identity element and inverse elements (which represent the same vector with the same magnitude but opposite direction); and for the scalars multiplication of associativity, identity element, and distributivity in respect of vector addition and field addition [100]. Since the vector spaces are finite and they have a basis defined by $\{\mathbf{v}_1, \mathbf{v}_2, \ldots, \mathbf{v}_n\}$ for the space $\mathbf{V}$ and $\{\mathbf{w}_1, \mathbf{w}_2, \ldots, \mathbf{w}_m\}$ for the space $\mathbf{W}$, then every linear map or transformation can be represented by a matrix [84]. Let us define a matrix A of $m \times n$ dimensions, where the linear transformation or mapping from $\mathbb{R}^n \to \mathbb{R}^m$ is expressed by $f(x) = A\mathbf{x}$. To visualize this expression, let us remember that if every vector $\mathbf{v} \in \mathbf{V}$ and the coefficients $\lambda \in \mathbb{R}$, then $\mathbf{v} = \lambda_1 \mathbf{v}_1 + \cdots + \lambda_n \mathbf{v}_n$ is valid. For the linear transformation $f : \mathbf{V} \to \mathbf{W}$, where

$$f(\mathbf{v}) = f(\lambda_1 \mathbf{v}_1 + \cdots + \lambda_n \mathbf{v}_n) = \lambda_1 f(\mathbf{v}_1) + \cdots + \lambda_n f(\mathbf{v}_n),$$

and the basis of $\mathbf{W}$, the new set of vectors will be

$$f(\mathbf{v}_j) = f(a_{1j} \mathbf{w}_1 + \cdots + a_{mj} \mathbf{w}_m),$$

where $j = 1, \ldots, n$.

Hence,

$$
\begin{aligned}
f(\mathbf{v}) = {} & f(\lambda_1 \mathbf{v}_1 + \cdots + \lambda_n \mathbf{v}_n) \\
= {} & \sum_{j=1}^{n} \lambda_j f(\mathbf{v_j}) = \sum_{j=1}^{n} \lambda_j \left(\sum_{i=1}^{m} a_{ij} w_i \right) \\
= {} & \sum_{i=1}^{m} \left(\sum_{j=1}^{n} a_{ij} \lambda_j \right) w_i
\end{aligned}
$$

Then,

$$
f_{\mathbf{v}} =
\begin{bmatrix}
\sum_{j=1}^{n} a_{1j} \lambda_j \\
\vdots \\
\sum_{j=1}^{n} a_{mj} \lambda_j
\end{bmatrix}
=
\begin{bmatrix}
a_{11} & \cdots & a_{1n} \\
a_{21} & \cdots & a_{2n} \\
\vdots & \vdots & \vdots \\
a_{m1} & \cdots & a_{mn}
\end{bmatrix}
\begin{bmatrix}
\lambda_1 \\
\lambda_2 \\
\vdots \\
\lambda_n
\end{bmatrix}
\tag{3.1}
$$

where the A matrix has dimensions $m \times n$ such that $A_{ij} = a_{ij}$, thus $f(\mathbf{v}) = A\mathbf{x}$.

Before defining and mathematically express a rotation, translation and scaling transformation, it must be clarified that not all these motions are linear transformations if they are not centered in the origin. Thus, a method to represent these motions with matrix multiplication is using projective geometry and expressing these matrices in homogeneous coordinates, which is a coordinate system that treats all points in the projective plane (i.e., a surface space without boundary that adds a line at infinity where the edges of the plane meet) the same [134][135], and by adding an extra coordinate w it will scale the dimensions x, y and z; thus, to represent the point (x,y), not scaled, in homogenous coordinates, w takes the value of one and is represented by (x,y,1).

Moreover, let us remember that the centripetal force is a net force that maintains the circular motion of an object and is directed toward its axis of rotation. However, to initiate this circular motion, a force must be applied over the object at rest. Let us assume that initially our detector $\mathbf{r}$ is not moving but at some point, a force $\mathbf{F}$ is applied or acts on it, which will produce a change in its angular displacement $\Delta\theta$ and, consequently, an angular acceleration ω. The measure of this applied force is called torque τ and its direction will depend on the direction of the force applied to the object's axis [136]. To explain this

measurement, let us define the pivot point (or rotation axis) at the center or half of the detector length, this is $r/2$, where to start a rotational motion, a force is applied at the extreme of the detector, as seen in Figure 3.4. Since the detector is
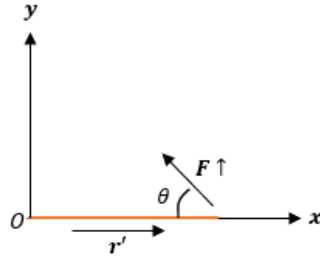
FIGURE 3.4: Perpendicular force **F** applied to the detector **r** at a direction given by the angle θ. The origin is defined at half of the detector's length and **r'** represents the vector that goes through the axis of rotation and the force applied.

defined by a vector **r**, with magnitude r, the vector distance between the pivot point and the applied force at the end of the detector length will be called **r'**, and is perpendicular to the force applied. Thus, the torque can be defined by

$$\tau = \mathbf{r'} \times \mathbf{F} = \frac{1}{2}rF\sin\theta, \tag{3.2}$$

where θ is the angle between the force vector and the distance vector. Thus, if the rotation is applied clockwise (i.e., in the direction in which the hands of a clock move), the torque is negative but if it is counterclockwise (i.e., in the opposite direction in which the hands of a clock move), the torque will be positive. Nevertheless, it must be mentioned that ideally, the detector must not move since it is desired for the motions in the assembly to be performed only by the support or base structure; however, the possible detector motions are stated in this thesis in case alignment or repositioning of the detector is needed.

Rotation

Moreover, let us utilize the previous vector and matrix notation to explain the displacement of the detector. All the mentioned rotations in this section will refer to

the movement of the detector device in a fixed coordinate system (unless indicated) called active transformations; however, the rotation of a coordinate system with respect to a fixed object (i.e., passive transformation) can be also described by this notation. If we assume that the detector's vector $\mathbf{r}$ is originally positioned in the Cartesian plane at the point $(x, y) = (r \cos \theta', r \sin \theta')$, where r is the length of the detector and θ is the direction angle of the detector, as pictured in Figure 3.3. The matrix form is

$$\mathbf{r} = \begin{bmatrix} x \\ y \end{bmatrix} = \begin{bmatrix} r \cos \theta' \\ r \sin \theta' \end{bmatrix}. \tag{3.3}$$

for an angle θ moved counterclockwise (see Figure 3.5), then the new vector $\mathbf{r}'$ will be given by

$$\mathbf{r}' = \begin{bmatrix} x' \\ y' \end{bmatrix} = \begin{bmatrix} r \cos(\theta' + \theta) \\ r \sin(\theta' + \theta) \end{bmatrix},$$

using trigonometric identities, we have

$$\begin{aligned} \mathbf{r}' &= \begin{bmatrix} r \cos \theta' \cos \theta - r \sin \theta' \sin \theta \\ r \sin \theta' \cos \theta + r \cos \theta' \sin \theta \end{bmatrix} \\ &= \begin{bmatrix} x \cos \theta - y \sin \theta \\ y \cos \theta + x \sin \theta \end{bmatrix} \end{aligned} \tag{3.4}$$

or

$$\begin{bmatrix} x' \\ y' \end{bmatrix} = \begin{bmatrix} \cos \theta & -\sin \theta \\ \sin \theta & \cos \theta \end{bmatrix} \begin{bmatrix} x \\ y \end{bmatrix} \tag{3.5}$$

and this matrix operation has the form of the linear transformation denoted by $f(\mathbf{x}) = A\mathbf{x}$ that is equivalent to the matrix linear transformation, $T(\mathbf{x}) = A\mathbf{x}$, where T is the transformation matrix and A is the rotation matrix $R(\theta)$ [100][131].
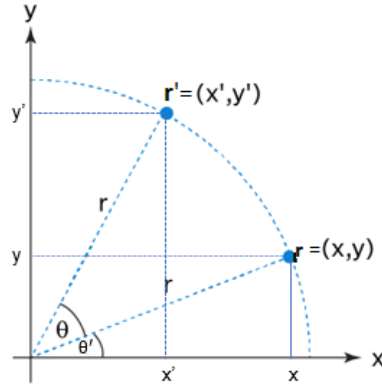
FIGURE 3.5: Rotation of a vector **r** at the position (x, y) with a directional angle of θ' in a xy-plane by an angle θ [137].

Expressing this in terms of homogeneous coordinates and for a coordinate system of (x, y, z), the rotational matrices respect each axis will be of the form

$$
\begin{aligned}
R_x(\theta) &= \begin{bmatrix} 1 & 0 & 0 \\ 0 & \cos\theta & -\sin\theta \\ 0 & \sin\theta & \cos\theta \end{bmatrix} \\
R_y(\theta) &= \begin{bmatrix} \cos\theta & 0 & \sin\theta \\ 0 & 1 & 0 \\ -\sin\theta & 0 & \cos\theta \end{bmatrix} \\
R_z(\theta) &= \begin{bmatrix} \cos\theta & -\sin\theta & 0 \\ \sin\theta & \cos\theta & 0 \\ 0 & 0 & 1 \end{bmatrix} .
\end{aligned}
\tag{3.6}
$$

Additionally, multiple rotations can be applied at the same time to a vector. This is represented by a matrix product from right to left, where the first rotation is the last matrix on the right side, and the last rotation is indicated by the first matrix

of the left side [100], and is represented by

$$R = R_z(\gamma)R_y(\beta)R_x(\alpha)$$

$$= \begin{bmatrix} \cos\gamma & -\sin\gamma & 0 \\ \sin\gamma & \cos\gamma & 0 \\ 0 & 0 & 1 \end{bmatrix} \begin{bmatrix} \cos\beta & 0 & \sin\beta \\ 0 & 1 & 0 \\ -\sin\beta & 0 & \cos\beta \end{bmatrix} \begin{bmatrix} 1 & 0 & 0 \\ 0 & \cos\alpha & -\sin\alpha \\ 0 & \sin\alpha & \cos\alpha \end{bmatrix}.$$

If R is applied to a vector $\mathbf{v}$, the vector $\mathbf{v}$ will be first rotated by an angle α in respect of the x-axis, then the new vector $\mathbf{v}'$ will be rotated by an angle β in respect of the y-axis, resulting in a new vector $\mathbf{v}''$ that will be rotated around the z-axis by an angle γ. For inverse rotations, the rotation angle θ must be moved clockwise. The combinations where rotations are in respect of three different axis are called Tait-Bryan rotations, if the first and last rotation are in respect of the same axis then they describe the proper Euler angles [138].

Every rotation represents a specific movement of the detector. If we place the detector in a 3D space where the z-axis runs in an upward direction and the x-axis is pointing towards the observer then, R_x has a *yaw* motion, R_y a *pitch* motion and R_z a *roll* motion [138]. It must be considered that a gamma camera has an entry point or window considered to be the "front" of the detector and must be always pointing in the direction of the object of study while the "back" is connected to the data processor. In this configuration, the detector is centered on the y-axis and the sample is positioned facing the device over the same axis. Therefore, we can delimit the angle's domain of this device in the following way:

- **Roll motion R_z:** Since this motion does not change the up, down or lateral directions of the detector, the rotation is not useful and can be omitted.

- **Pitch motion R_y:** This motion produces an up and down movement. Because we want to capture useful data from the radiative sample, there is a point where this detector will not be facing the sample nor capturing any data. Thus, the remotest points are $-\pi/2 = -90°$ and $\pi/2 = 90°$, so $\beta \in (-\pi/2, \pi/2)$.

- **Yaw motion** R_x**:** The motion domain is similar to the *pitch* but with the difference that the movement is lateral. Thus, following the same reasoning being of the previous motion, $\alpha \in (-\pi/2, \pi/2)$.

Translation

A translation is a type of linear transformation that occurs in an affine space. Thus, every point in the object is moved or translated to a new position where the length of parallel lines is preserved but the length between points and angles between lines might not be [105][131], since in the affine space there is no point that marks an origin thus no vector has a fixed origin and no vector can be uniquely associated to a point, see Figure 3.6.
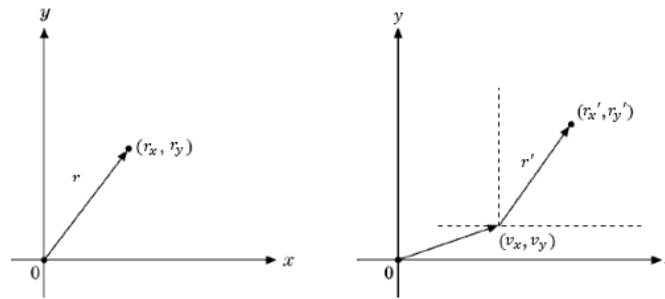
FIGURE 3.6: Translation of a vector $\mathbf{r}$ to a position (r'_x, r'_y) in a xy-plane by a vector $\mathbf{v}$ [100].

In this case, we will have a translation when the detector moves through the z-axis (height), y-axis (backward and forward), and x-axis (laterally). Thus, let us define this motion by setting a reference or fixed vector $\mathbf{v}$, referred to as the translation vector, where the detector's vector $\mathbf{r}$ indicates its initial position, so the transformation matrix will be expressed of the form $T(\mathbf{r}) = \mathbf{r} + \mathbf{v}$. If the detector is located at a point (x, y, z) and is moved by a translation vector to a point (x', y', z'), then the *translated* vector will be of the form $T(x, y, z) = (x + x', y + y', z + z')$. Even though this motion is not a linear transformation, it can be represented in a matrix form utilizing homogeneous coordinates. Although, because in this case, we do not have any fixed points, we have to use homogenous coordinates. Thus, for a vector of the form $\mathbf{v} = (v_x, v_y, v_z)$, we can use $\mathbf{v} = (v_x, v_y, v_z, 1)$ homogeneous

coordinates. And, following the matrix equation, we will have

$$T_{\mathbf{v}}\mathbf{r} = \begin{bmatrix} 1 & 0 & 0 & v_x \\ 0 & 1 & 0 & v_y \\ 0 & 0 & 1 & v_z \\ 0 & 0 & 0 & 1 \end{bmatrix} \begin{bmatrix} r_x \\ r_y \\ r_z \\ 1 \end{bmatrix} = \begin{bmatrix} r_x + v_x \\ r_y + v_y \\ r_z + v_z \\ 1 \end{bmatrix} = \mathbf{r} + \mathbf{v} \tag{3.7}$$

where $T_{\mathbf{v}}$ is the 4×4 matrix and represents the translation matrix for a fixed point $\mathbf{v}$. And, the inverse of this matrix is expressed by reversing the vector's $\mathbf{v}$ direction $T_{\mathbf{v}}^{-1} = T_{-\mathbf{v}}$ [100]. In this case, the translation domain will depend on the sample's dimensions and the leg's maximum and minimum length.

3.1.2 Base

Previously, it was stated that the assembly has a base in the shape of a tripod, which is constituted by three cylindrical legs with spherical ends. This base is expected to realize the translation motion of the detector by changing (or stretching) the length of its legs. Therefore, let us define the legs and tripod geometry in 2D and 3D, assumptions and limits for this section. Here, the motions are first described for one leg then, assuming that every leg has the same characteristics, the motion for the entire tripod is done; however, the detector is not considered in the figures or motions until the support is fully described.

One Leg Motion

If one leg is expressed by a vector $\mathbf{t}$ on the xy-plane, with a length denoted by t and a direction angle respect the x-axis as θ (see Figure 3.3 for reference of a vector in a plane), then its Cartesian point will be given by $(x, y) = (t_x, t_y) = (t\cos\theta, t\sin\theta)$ with a matrix interpretation of the form

$$\mathbf{t} = \begin{bmatrix} t_x \\ t_y \end{bmatrix} = \begin{bmatrix} t\cos\theta \\ t\sin\theta \end{bmatrix}. \tag{3.8}$$

To achieve a translation movement on the detector, it is necessary for the legs of the base to change length dimensions, this is, that they expand or contract.

However, the increase of dimensions must be only projected in the height or longitude of the leg. This type of linear transformation is a special case of Scaling performed for different scale values or fixed points, thus it is referred to as a Non-Uniform Scaling transformation [131], since the scaling factors are not equally applied and at least one factor is different than the others, see Figure 3.7. Similarly as the translation transform, this scaling occurs in an affine space where
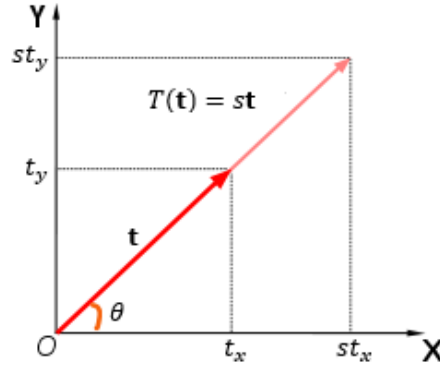
FIGURE 3.7: Scaling of a vector **t** to a position $s\mathbf{t}$, where s is the scaling factor and the original point is located at (t_x, t_y) with a magnitude or length of t.

the straight lines and parallel lines are preserved but the angles are not, as shown in Figure 3.6. In a non-uniform scaling, the lengths, areas and volumes of the object are varied by a factor relative to the direction of scale [135]. So, the scaling quantities will be determined by the set $S = (S_x, S_y, S_z)$ for each point of $\mathbf{t} = (t_x, t_y, t_z)$. It can also be understand as the quantity S_x that is changing or stretching the vector t in the x direction, the S_y factor in the y-direction, and so on. Thus, to obtain the scaled vector, let us define this transformation of the form $T(\mathbf{t}) = S\mathbf{t}$ with a matrix

$$T(\mathbf{t}) = \begin{bmatrix} S_x & 0 & 0 & 0 \\ 0 & S_y & 0 & 0 \\ 0 & 0 & S_z & 0 \\ 0 & 0 & 0 & 1 \end{bmatrix} \begin{bmatrix} t_x \\ t_y \\ t_z \\ 1 \end{bmatrix} = \begin{bmatrix} S_x t_x \\ S_y t_y \\ S_z t_z \\ 1 \end{bmatrix} = S\mathbf{t}, \tag{3.9}$$

where S is the Scaling matrix 4×4 and $T(\mathbf{t})$ is the resulting transformation. Following this, if $S_x = S_y = S_z$ then the scale is uniform and every point is scaled on the same terms. If any S scalar is less than 1, then the object or vector is contracted. If $S > 1$, the object is stretched or elongated [131]. To obtain the inverse of this transformation let us analyze the scalar matrix, for

$$S = \begin{bmatrix} S_x & 0 & 0 & 0 \\ 0 & S_y & 0 & 0 \\ 0 & 0 & S_z & 0 \\ 0 & 0 & 0 & 1 \end{bmatrix} = S(S_x, S_y, S_z) \tag{3.10}$$

the inverse of S is

$$S^{-1}(S_x, S_y, S_z) = S\left(\frac{1}{S_x}, \frac{1}{S_y}, \frac{1}{S_z}\right), \tag{3.11}$$

where $1/S = S^{-1}$ indicates the reciprocal of each scale factor [100].

Furthermore, let us apply this scaling concept to one leg of the base. As mentioned, the translation motion is dictated by the extension or contraction of the legs that form the base. So, the scaling transformation of one leg affects the detector's position. However, for a coordinate system positioned at the center of mass of the leg (see Figure 3.8), we are only interested in the scaling of the cylinder's length t, thus, its radius will remain the same. Therefore, the scaling is
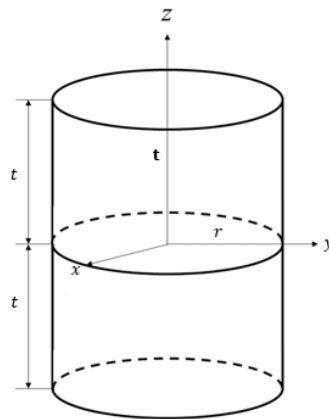
FIGURE 3.8: Leg of the base represented by a cylinder and a vector $\mathbf{t}$ on a 3D system, where the z-axis represent the height, and x and y the radius.

(A) Cylindrical coordinates

(B) Cylindrical coordinates with unit vectors [139]
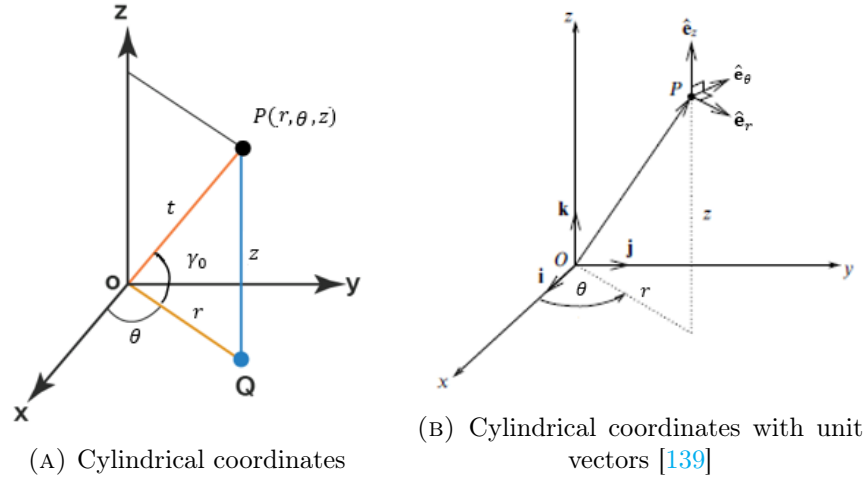
FIGURE 3.9: Leg vector **t** with magnitude t (orange line) delimited by a point P in cylindrical coordinates, where Q indicates a point in the xy-plane. The coordinate r is the line between the origin and the point Q (yellow line), θ is the angle between the x-axis and r, and z is the distance between point P and Q (blue line). The angle γ_0 is the direction angle of the leg over the xy-plane in respect of r.

not uniform and it only affects the height (or z-axis) of the cylinder. It is expressed by the Scaling matrix S of the form

$$S = \begin{bmatrix} 1 & 0 & 0 & 0 \\ 0 & 1 & 0 & 0 \\ 0 & 0 & S_z & 0 \\ 0 & 0 & 0 & 1 \end{bmatrix} \tag{3.12}$$

with a new scaled vector $\mathbf{t}' = (t_x, t_y, S_z t_z)$, where the S_z can be any real number. In this case, this number will be delimited by the sample's dimensions.

It is evident that the representation in Polar coordinates for this situation is no longer useful so, let us represent this leg by a vector **t** in a 3D space with the Cylindrical coordinates $P(r, \theta, z)$, where r is the radial distance from the origin to a point in the xy-plane, θ is the angle between r and the x-axis, and z is the height of the leg above the surface or the distance between the plane xy and its point P (see Figure 3.9a). And the conversion between Cartesian and Cylindrical coordinates can be seen on the Table 3.2. And, Equation 3.12 will have the following form in

Coordinates Conversion Table		
	Cartesian	Cylindrical
Cartesian	x	$x = r\cos\theta$
	y	$y = r\sin\theta$
	z	$z = z$
Cylindrical	$r = \sqrt{x^2 + y^2}$	r
	$\theta = \arctan(y/x)$	θ
	$z = z$	z

TABLE 3.2: Conversion table for Cartesian and Cylindrical coordinates [100].

Polar coordinates

$$S = \begin{bmatrix} 1 & 0 & 0 & 0 \\ 0 & 1/r & 0 & 0 \\ 0 & 0 & S_z & 0 \\ 0 & 0 & 0 & 1 \end{bmatrix}. \tag{3.13}$$

If we consider that the space where the leg is positioned is a room, following Figure 3.9a and Table 3.2, for a coordinate system whose origin is over the surface of the room, the leg is positioned at an angle γ_0 above the surface and z is the height between the floor and the leg's position over the surface. Assuming the leg is represented by a line or a vector, the scaling may occur in the directions (x, y, z), for Cartesian coordinates, or (r, θ, z), for cylindrical coordinates, where the origin is considered to be the lower extreme of the leg that is in contact with the xy-plane in the Cartesian coordinate system. In Figure 3.9b, the unit vectors indicate the direction of the motion of the unit vectors (r, θ, z) thus we can infer that if the leg is extended or scaled, they will follow the direction of these components. Also, notice that if the length of the leg varies, it will affect other positions or coordinate values in the system (see Table 3.2 for the relationship between coordinates) so, for each case, some important relations have been expressed (the Cylindrical coordinate system was used to better understand the following mathematical expressions but the motions and scaling factor directions are better explained in Cartesian coordinates for this case).

- **Up and Down.** For this motion, the scaling factors for r and θ remain on their original scale, thus $w = 1$, while the S_z takes any values greater than zero in order to extend the leg's length. In this case, the r value remains constant but its direction angle γ_0 and height z change. If we know the r and new length st value, where s is the scaling factor, the relationships $\gamma_0 = \arctan{(r/st)}$ and $z = st \sin{\gamma_0}$ can be used to obtain the height of the leg in a direct form.

- **Lateral.** For this case, we want to alter the leg position over the x-axis or in the θ direction (for cylindrical coordinates, see Figure 3.9b)so the height factor S_z and S_r are one but the S_θ varies. In this case, the leg is changing its position in the x-direction so the r and γ_0 may vary, but the height remains the same and the length of the leg is know, so $\gamma_0 = \arcsin{(z/t)}$ and $r = t \tan{\gamma_0}$.

- **Back and Front.** In this case, if the S_r factor has a value different than one, that is that it shrinks or elongates, while the $\hat{e}_z$ and $\hat{e}_\theta$ directions remain constant. The leg position, in a cartesian coordinate system, will vary for the x and y components. Thus, to obtain the height and angle with respect to the surface, the equations stated on the ***Lateral*** case remain the same.

The scaling factor for all the cases depend on the other legs' conditions and the sample's dimensions, which will be explained in the following sections.

Three Legs (Tripod)

Before defining the geometry of the base, let us define a tripod and the purpose of its use. A tripod is a portable three-leg stand used to support and maintain the stability of an object. The most common materials employed in the fabrication of a tripod for laboratory and field environments are stainless steel or aluminum, with a diameter for each leg of around $20 - 30 \, \text{mm}$ and a tripod length above the surface of minimum $1000 \, \text{mm}$.

So far, we have described one leg in a cylindrical system and reviewed the motion that it has to perform, as a single element of the base, to obtain a translation

(A) Top or bottom reference frame of the tripod

(B) Lateral reference frame of the tripod
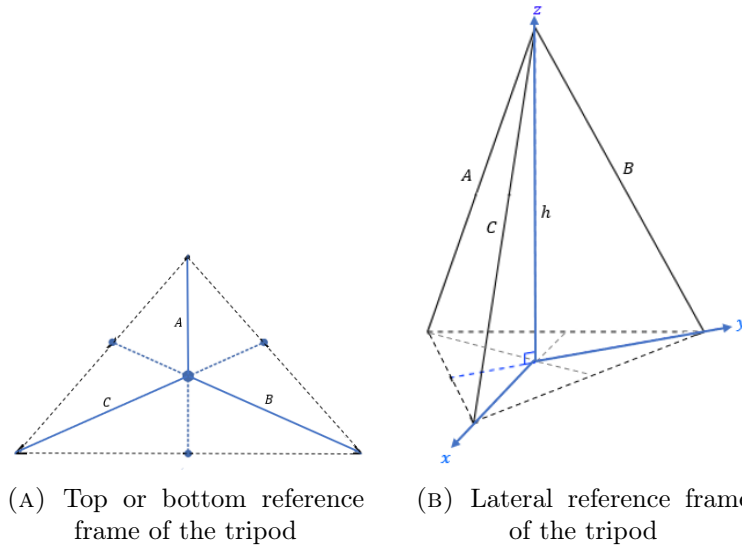
FIGURE 3.10: A) Definition of the tripod in a plane (triangle), where the blue lines represent the legs. B) Definition of the tripod on a 3D Cartesian coordinate system (triangular pyramid) at a height h; the medians serve as a reference point for the axis x and y.

response from the detector. However, the complete base accounts for the motion of three legs so let us describe the geometry and features of a three-cylindrical leg structure to allow the analysis of the effect that one leg has over the entire configuration in Section 3.1.3. This said, the following section will delineate the geometry of this stand and delimit its main parameters, where a detailed 2D and 3D geometrical representation of this figure is done for a better understanding of the support.

A tripod can be described in its simplest form, as a triangle. Analyzing this structure from a top or bottom perspective, we will observe three lines that join at a point. If each end-point is connected to the next one, we will form a triangle, see Figure 3.10a. Notice that extending the lines that define the triangle to the next parallel midpoint segment will form a median and the already defined intersection will be the orthocenter of the triangle [140]. In the same way, if this structure is observed laterally in a perspective where the three legs are visible, and if the adjacent end-points are connected, then a triangular pyramid will be drawn, see Figure 3.10b. At the same time, this pyramid can be seen as the composition of

four triangular faces, where each face has its own centroid that can be used as a reference or origin point to delineate a three-dimensional Cartesian space as shown in Figure 3.10b.

By defining this structure in a Cartesian space, it will be possible to describe each leg in a length and angle relation, where these dimensions can be measured in real scenarios. Therefore, let us visualize one leg in a 3D Cartesian space as depicted in Figure 3.11 to determine its characteristic equations.
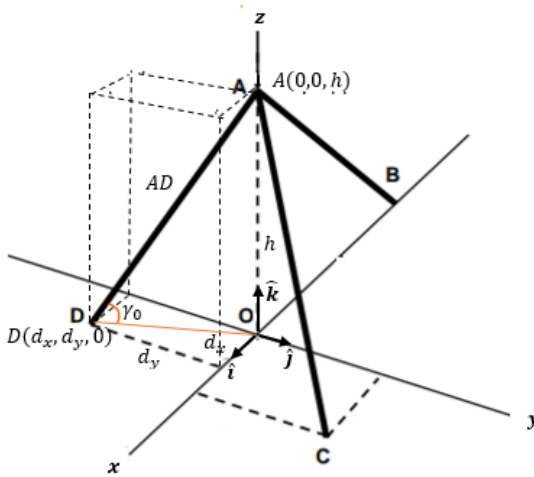
FIGURE 3.11: Tripod in a Cartesian coordinate system with unit vectors $(\hat{\mathbf{i}}, \hat{\mathbf{j}}, \hat{\mathbf{k}})$, and represented by a line that connects the points D and A.

The previous figure represent the three legs as lines that connect their position (B, C, D) on the plane xy to a high point A. Thus, let us analyze one line to describe the parameters of the rest. Here, the line segment that connects the initial point D and the final point A is described with the parameters d_x for the length of the point D respect x-axis, d_y for the distance respect the y-axis, h for the height of the leg or tripod, AD to indicate the length of the line, and γ_0 for the leg's direction angle respect the surface. The parameters AD and h can be measured in practice, so the relation $\gamma_0 = \arcsin(h/AD)$ can be calculated to measure the direction angle of the leg. However, the components or dimensions for d_x and d_y are more difficult to obtain in real arrangements. To avoid this, let us apply the Pythagoras theorem to find the distance d between the origin and the point D and

determine $d = AD \cos \gamma_0$, so the components d_x and d_y could be calculated with the following relations for a known directional angle of the distance d respect the x-axis

$$d = \sqrt{d_x^2 + d_y^2}$$
$$d_x = AD \cos \gamma_0 \cos \theta \qquad (3.14)$$
$$d_y = AD \cos \gamma_0 \sin \theta.$$

Moreover, let us define the mathematical interpretation of this line segment by obtaining the relation between the location of the top A and end D points of the leg. The equation of a line is used to provide all the necessary information about a segment at any point or slope existent in it, and it is determined by the relation $y = mx + b$ where m is the slope of the line or the change ratio between the vertical and horizontal components, b is the intersection of the line with the axis y, and the variable components (x, y) represent any point of the line in respect the x and y axis [131], for a 2D coordinate system. However, in this case, we depict this line in a 3D space through the three components (x, y, z). Also, let us remember that for simplicity we have been referring to this leg as a line but, in fact, it is a line segment with orientation (i.e., direction). The justification for the assumption that the legs can be represented through vectors will be shown later on. This said, we desire to find the vector equation that describes the mapping of the point D to the point A. So, if we define a starting point $P_0(x_0, y_0, z_0)$, an endpoint $P(x, y, z)$, and a vector $\mathbf{v} = a\hat{\mathbf{i}} + b\hat{\mathbf{j}} + c\hat{\mathbf{k}}$ that goes in the same direction as the line that connects these points. Then, we can define a vector $\mathbf{P_0P}$ given by

$$\mathbf{P_0P} = (x - x_0)\hat{\mathbf{i}} + (y - y_0)\hat{\mathbf{j}} + (z - z_0)\hat{\mathbf{k}}. \qquad (3.15)$$

Even though this vector goes in the same direction as $\mathbf{v}$, they might not have the same magnitude. Thus $\mathbf{P_0P}$ is a multiple of the directional vector $\mathbf{v}$, or

$$\mathbf{P_0P} = t\mathbf{v}$$
$$= t(a\hat{\mathbf{i}} + b\hat{\mathbf{j}} + c\hat{\mathbf{k}}), \qquad (3.16)$$

where the parameter $t \in \mathbb{R}$ and $(\hat{\mathbf{i}}, \hat{\mathbf{j}}, \hat{\mathbf{k}})$ are the unit or directional vectors of each component. By using Equation 3.15 in 3.16 we will obtain the following system of equations for each component

$$
\begin{aligned}
x &= x_0 + at \\
y &= y_0 + bt \\
z &= z_0 + ct
\end{aligned}
\tag{3.17}
$$

which has the general form of $\mathbf{r} = \mathbf{P_0} + t\mathbf{v}$, and by rearranging this set of equations in terms of their parameter t we can find the symmetric form of the equation of the line

$$
\frac{x - x_0}{a} = \frac{y - y_0}{b} = \frac{z - z_0}{c}.
\tag{3.18}
$$

If we apply the conditions of our system delimited by Figure 3.11 to the Equations 3.15, 3.16, 3.17 and 3.18, we will obtain the following expressions for the line equation

$$
\text{Vector} \quad \mathbf{r} = (d_x\hat{\mathbf{i}} - d_y\hat{\mathbf{j}}) + t(-d_x\hat{\mathbf{i}} + d_y\hat{\mathbf{j}} + h\hat{\mathbf{k}})
$$

$$
\text{Parametric} \quad
\begin{aligned}
x &= d_x - td_x \\
y &= -d_y + td_y \\
z &= th
\end{aligned}
$$

$$
\text{Symmetric} \quad t = \frac{d_x - x}{d_x} = \frac{y + d_y}{d_y} = \frac{z}{h}
$$

$$
\text{Direction Vector} \quad \mathbf{AD} = -d_x\hat{\mathbf{i}} + d_y\hat{\mathbf{j}} + h\hat{\mathbf{k}} = (-d_x, d_y, h)
$$

Furthermore, additional information can be obtained from this configuration. As mentioned, a vector can be described in terms of unit vectors that represent a spatial and relative direction for each of its components [135]. Therefore, following this context, it is possible to determine the relationship between a vector and each axis via directional angles. These angles or directional cosines are merely a component of the unit vector and are used to indicate the direction that an object or a line has in a 3D space by stating the relationship between two lines that intersect

(A) Directional angles for a vector **v** [100].

(B) Directional angles for the vector DA
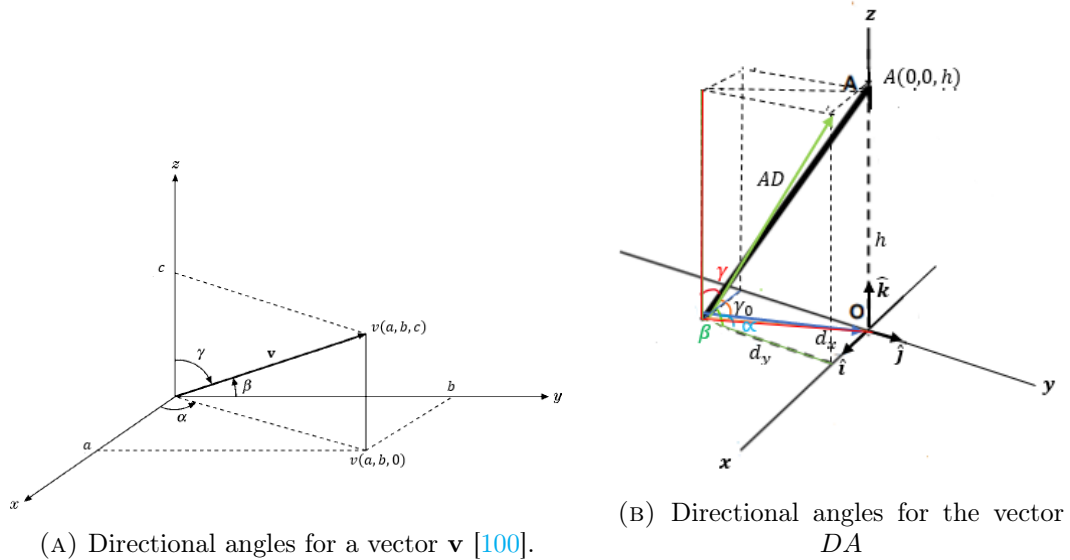
FIGURE 3.12: Definition of the directional angles for a A) vector **v** and B) leg vector AD, where the blue and green arrows are a projection of the vector **v** over the x and y planes to show the directional angles location in a plane. Notice that the directional angles must be defined from the origin to a point in the system.

at some point (e.g. a coordinate axis and a line perpendicular to it) [100][131]. This interpretation is only another representation of the direction of a vector with respect to each axis (x, y, z) that could simplify or add information about the system. To define them let us consider a random point in the 3D Cartesian space, where its position vector (i.e., a vector that represents the position of the point in relation to an arbitrary point of origin O) forms positive angles (i.e., counterclockwise) between the planes (x, y), (y, z) and (x, z) that are called directional angles and defined by α, β and γ [100], see Figure 3.12a. Notice that the angles defined in Figure 3.12a are independent of the previous notation used.

Consequently, the coordinates for any $P(x, y, z)$ point can be represented in a relationship between the directional angles and the magnitude of the directional

vector **v**

$$x = l||v||$$
$$y = m||v||$$
$$z = n||v||,$$

where l, m and n are the directional cosines since they represent a cosine function of each directional angle, and $||v|| = \sqrt{a^2 + b^2 + c^2}$. Thus, for a point $v(a, b, c) = a\hat{\mathbf{i}} + b\hat{\mathbf{j}} + c\hat{\mathbf{k}}$ and following Figure 3.12a we can define

$$
\begin{aligned}
l &= \cos\alpha = \frac{\mathbf{v}}{||\mathbf{v}||}\hat{\mathbf{i}} = \frac{a}{\sqrt{a^2 + b^2 + c^2}} \\
m &= \cos\beta = \frac{\mathbf{v}}{||\mathbf{v}||}\hat{\mathbf{j}} = \frac{b}{\sqrt{a^2 + b^2 + c^2}} \\
n &= \cos\gamma = \frac{\mathbf{v}}{||\mathbf{v}||}\hat{\mathbf{k}} = \frac{c}{\sqrt{a^2 + b^2 + c^2}}.
\end{aligned}
\tag{3.19}
$$

Since the line that connects our point with the origin has a length or magnitude of v, we can relate this to the previous equations

$$\cos^2\alpha + \cos^2\beta + \cos^2\gamma = \frac{a^2}{v^2} + \frac{b^2}{v^2} + \frac{c^2}{v^2},$$

and by rearranging terms and using the magnitude $v = \sqrt{a^2 + b^2 + c^2}$, we obtain

$$\cos^2\alpha + \cos^2\beta + \cos^2\gamma = 1 \tag{3.20}$$

with $l^2 + m^2 + n^2 = 1$ which corroborates that l, m and n are the direction cosines of the unit vector for a Cartesian system, and α, β and γ are the directional angles of the vector **v**.

Applying these definitions to our system and defining the directional cosines of the vector $\mathbf{AD} = (-d_x, d_y, h)$ with $||\mathbf{AD}|| = AD = \sqrt{(-d_x)^2 + (d_y)^2 + (h)^2}$ we

obtain

$$\cos\alpha = \frac{-d_x}{\sqrt{(-d_x)^2 + (d_y)^2 + (h)^2}} = -\frac{d_x}{AD} \quad \Rightarrow \quad d_x = -AD\cos\alpha$$

$$\cos\beta = \frac{d_y}{\sqrt{(-d_x)^2 + (d_y)^2 + (h)^2}} = \frac{d_y}{AD} \quad \Rightarrow \quad d_y = AD\cos\beta \qquad .$$

$$\cos\gamma = \frac{h}{\sqrt{(-d_x)^2 + (d_y)^2 + (h)^2}} = \frac{h}{AD} \quad \Rightarrow \quad h = AD\cos\gamma$$

The previous set of equations provides an additional approach for the measurement of the distances d_x and d_y (see Figure 3.12b) and, if we compare the directional angle for the z-axis with the relations obtained for Figure 3.11, we will notice that the directional angle γ is related to the direction angle γ_0 since both angles are in reference to the z-axis or height h. Let us remember that the Cartesian coordinate system and its unit vectors $\hat{\mathbf{i}}$, $\hat{\mathbf{j}}$ and $\hat{\mathbf{k}}$ are perpendicular and orthogonal since their coordinates (x, y, z) are planes that intersect at right angles (i.e., angles with an aperture of $\pi/2$) [100]. Therefore, we can relate the angles obtained for the z-axis of the form $\gamma = \frac{\pi}{2} - \gamma_0$, and the same reasoning can be applied to the angles θ and β for the x-axis, leading to $\theta = \frac{\pi}{2} - \beta$ (see Equations 3.14).

All the legs in the system can provide the same information and be expressed with their characteristic parameters for their location in the space, so the previous equations will only vary in signs and angles definition. However, the directional cosines will not be affected since the cosine function is even, which suggests that the sign of the directional angle is irrelevant to the definition. Additionally, some conditions defined for the DA leg apply to every other leg position in the 3D coordinate system. These are:

- $h > 0$: In the coordinate definition of any leg its height will always be greater than zero, implying that the position of the leg on the surface has only x and y coordinates.

- **Intersection point** $(0, 0, h)$: For every leg in every possible configuration, the point where all the legs meet is $(0, 0, h)$, which means that these

coordinates are standard to describe the location of the end of the leg unless a motion is performed.

3.1.3   Assembly

In the previous section, methods to represent the leg's position in a 3D Cartesian space were developed in order to determine measurable quantities in theoretical and experimental environments, so transformation matrices of the leg's motions could be expressed and could represent possible detector positioning around the sample. Therefore, it is necessary to add and consider all these individual contributions in entirety to explain the functioning and performance features of a three-leg support. This said, let us remember that a tripod's main function is to provide support and stability to some other weight; in this case, a detector device that we have been previously referred to as the head of the tripod since it is positioned in its upper part. This section will connect the individual components and concepts described in the previous section to explain and model the proposed field-deployable detector assembly.

Static

As mentioned, the two main goals of a tripod are to bring support and stability to an object. In the physics world, support in a structure refers to the transfer of weight to the ground to bring stability to the object supported on it while stability acts as a measurement of how likely an object will lose balance or will stop being steady and fall when a force acts upon it [132]. Therefore, the goal is to conserve a balanced force relation between the weight and the tripod base. To achieve this, is important to review and reference Newton's Laws:

- **First Law.** If a body is at rest or moving at a constant velocity in a straight line, it will remain at rest or keep moving at this constant velocity unless a force is acted upon it.

- **Second Law.** Quantitative description of the change of momentum over time of a body when a force acts upon it, which will be equal in magnitude and direction to this rate change.

- **Third Law.** The relationship between two bodies that interact is due to the force that they apply to each other since it is equal in magnitude but opposite in direction [132][136].

Thus, a general set of assumptions and conditions can be formed with the previously stated:

1. The detector and base components (three legs) can be represented in the form of vector forces that have magnitude and direction. The detector force is $\mathbf{F_v}$ and the force in each leg $\mathbf{F_a}$, $\mathbf{F_b}$ and $\mathbf{F_c}$.

2. The configuration of the detector and tripod is said to be static and isolated since no other external forces are acting on it. This is that the vector sum of the external forces must be zero $\sum \mathbf{F} = 0$, where $\mathbf{F} = (F_x, F_y, F_z)$.

3. The object is in rotation equilibrium since at a static state there is no rotation then the external torques are $\sum \tau = 0$, where $\tau = (\tau_x, \tau_y, \tau_z)$.

Then, if conditions 1. and 2. are satisfied, the assembly is in static equilibrium. Notice that we are using the $\mathbf{F}$ symbol to denote forces, and each force has a component or direction in the (x, y, z) axis. Additionally, let us assume that the mass in the entire detector is concentrated in its center of mass (i.e., a position relative to an object, obtained through an average of all its parts considering its position and weight) or centroid, thus the gravity force is pointing downwards [136]; Figure 3.13 shows the configuration and force diagram of a suggested assembly configuration.

Following the previous assumptions and Figure 3.13 we can determine a general expression for the contribution of the forces on a tripod.

$$\sum \mathbf{F} = \mathbf{F_a} + \mathbf{F_b} + \mathbf{F_c} + \mathbf{F_v} \tag{3.21}$$

$$\mathbf{F_a} + \mathbf{F_b} + \mathbf{F_c} + \mathbf{F_v} = 0 \tag{3.22}$$

$$\mathbf{F_a} + \mathbf{F_b} + \mathbf{F_c} = -\mathbf{F_v}, \tag{3.23}$$

where all the forces have components in x, y and z, which can be expressed in terms of unit vectors or directional cosines; except for the force exerted by the
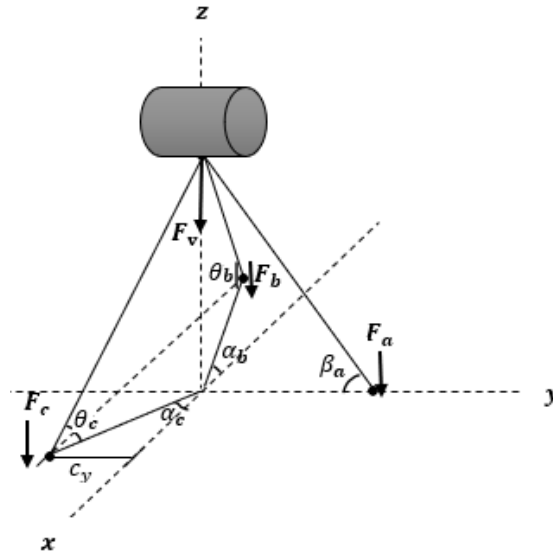
FIGURE 3.13: Diagram of a suggested tripod display over a Cartesian system with the applied forces: $\mathbf{F_a}$, $\mathbf{F_b}$ and $\mathbf{F_c}$ for the forces exerted by the three legs, and $\mathbf{F_v}$ for the force of the detector; and, includes relevant directional angles for the different legs' positions and dimensions.

detector $\mathbf{F_v}$, whose only direction is over the z-axis. Also, we can express each vector component in a matrix form with its dimensions

$$\begin{bmatrix} \mathbf{F_a} \\ \mathbf{F_b} \\ \mathbf{F_c} \end{bmatrix} = \begin{bmatrix} a_x & a_y & a_z \\ b_x & b_y & b_z \\ c_x & c_y & c_z \end{bmatrix}$$

$$\mathbf{F_v} = \begin{bmatrix} v_x & v_y & v_z \end{bmatrix}.$$

(3.24)

Since the total $\mathbf{F}$ has components in x, y and z it is possible to find quantities like the magnitude and direction of the force being applied to the detector, additional to the relation between the detector's position and the legs. And, let us remember that the matrix coordinates have a range of values and can also be expressed in terms of directional angles.

Transformations

Finally, with all the prior information, it is possible to delineate a relation between the detector and base motions. As seen, the detector and base perform different motions with various purposes. The tripod's movements are performed to re-locate or re-position the detector in a new line segment or cross-section area of the sample while the detector's rotation is done for scanning purposes. These movements are never performed simultaneously and, while the base structure may affect the positioning and direction of the detector with respect to the sample, the detector's motion will not affect the tripod's location nor arrangement. When referring to stretching and translation motions, the force vectors can also be described in these terms as an increase or decrease of the force applied and as the change of direction for the applied force. Also, this relation can be defined by analyzing the point of concurrency or point of intersection (i.e., a point where nonparallel lines meet, forming an intersection [135]) of the leg vectors and the detector considered as lines in the space. Therefore, the general relation between the change of length of the legs and the position of the detector can be expressed by locating the concurrency point of the three lines that represent the legs. This point is where three or more lines meet and, in this case, these lines are represented by the following set of equations

$$
\begin{aligned}
a_1x + b_1y + c_1z &= 0 \\
a_2x + b_2y + c_2z &= 0 \\
a_3x + b_3y + c_3z &= 0
\end{aligned}
\tag{3.25}
$$

where in order to know if they are concurrent or meet at a single point, the previous equations expressed in their matrix form must have a determinant zero; this is because the area formed with the concurrent lines is zero, as seen in the Equation 3.26.

$$
\begin{vmatrix}
a_1 & b_1 & c_1 \\
a_2 & b_2 & c_2 \\
a_3 & b_3 & c_3
\end{vmatrix} = 0
\tag{3.26}
$$

The determinant of a square matrix is a single number that can be related

to the area or volume of a region since the matrix entries are real numbers that represent the linear mapping of vectors.

Now, the equations for the legs 1 and 2 must intersect or meet at the same point with the leg (or line) 3. So, if we assume that they intersect at the point $P(x_1, y_1, z_1)$, then the first two equations will be satisfied. Thus, the solution of the new equation set in Equations 3.27 for the variables x_1, y_1 and z_1 in terms of the coefficients presented in Equation 3.26 will indicate the intersection point of these lines. At the same time, this point is where the detector device is positioned in the three-leg support.

$$
\begin{aligned}
a_1 x_1 + b_1 y_1 + c_1 z_1 &= 0 \\
a_2 x_1 + b_2 y_1 + c_2 z_1 &= 0 \\
a_3 x_1 + b_3 y_1 + c_3 z_1 &= 0
\end{aligned}
\tag{3.27}
$$

Moreover, if a translation, scaling or rotation is performed in the system, the transformations will be represented individually for each leg, and the addition of them will form the new positioning matrix for the tripod support; which is expressed in Equation 3.28 with homogeneous coordinates, applying a translation given by T which matrix can be seen on Equation 3.7.

$$
T_1 \begin{bmatrix} a_1 \\ b_1 \\ c_1 \\ 1 \end{bmatrix} + T_2 \begin{bmatrix} a_2 \\ b_2 \\ c_2 \\ 1 \end{bmatrix} + T_3 \begin{bmatrix} a_3 \\ b_3 \\ c_3 \\ 1 \end{bmatrix} = \begin{bmatrix} a_1 + v_1 & b_1 + w_1 & c_1 + u_1 \\ a_2 + v_2 & b_2 + w_2 & c_2 + u_2 \\ a_3 + v_3 & b_3 + w_3 & c_3 + u_3 \\ 1 & 1 & 1 \end{bmatrix}
\tag{3.28}
$$

where the sets v_1, v_2, v_3, w_1, w_2, w_3 and u_1, u_2, u_3 are the translation factors. Therefore, the change of one leg will affect the rest due to the symmetry and intersection point that they share.

Additionally, if the system is analyzed intuitively considering that in every case the initial position corresponds to a tripod whose legs form a 45° angle with the surface (i.e., the direction angle $\gamma = \pi/2$), the following hypothesis for the possible actions and reactions of the assembly are obtained:

1. By translating (with a positive or negative factor) all legs in the same quantity with respect the z-axis, the entire assembly will change height without changing position in (x, y); directional angles might vary.

2. Translating (positively or negatively) one or two coordinate components (these are (x,y,z)) one or two legs in the same direction by the same amount, and maintaining the same height, will translate the detector's position in relation to the chosen direction. The directional angles and legs' lengths might vary.

3. Translating (positively or negatively) one or two coordinate components in different directions and maintaining the same height, will translate the detector's position in the selected directions. The directional angles and legs' lengths will vary.

4. Translating one leg's position in the z-axis will change the detector's directional angle with respect to the (x, y) plane.

Chapter 4

Computational Model

The invention of the computer was a consequence of the need to reduce time while solving mathematical systems, promoting its accuracy and decreasing human errors. This need and purpose has not changed over the years, an increase in knowledge and advances in technology have required better and faster computational performances for experimental and theoretical applications. Therefore, a computational model can be seen as an additional path to corroborate and study a complex physical and mathematical system for the visualization and manipulation of data that is not physically accessible. Following this, a computational simulation of an emission tomography system with a field-deployable detector is described in this chapter as an alternative approach verified the theoretical performance of the previous possible motions or transformations for the tripod and its legs. Since we have seen and proven that the combination of mathematical expressions and physics laws enable the description of a physical system, we desire to transform those parameters into visible and interactive means. however, the following simulation is merely an example and exercise to verify the feasibility of a field-deployable detector, in order to corroborate that accurate positioning of the system with respect to a sample will allow data useful data acquisition. Thus, image reconstruction and source distribution statistical errors were not a focus in this thesis nor had a significant impact on the validation process.

In this thesis, a computational toolkit commonly used in high-particle fields like nuclear, medicine and space, is implemented to describe and visualize the assembly proposed. Geant4 is an object-orientated programming framework

based on C++ language of free use with open library resources for research purposes. The system includes physical and mathematical quantities, operations and units, geometry, tracking, detector response, run management, visualization and interactive user interface [141]. This platform is supported by CMake (an open-source build manager that generates a system's build files [142]) for compiling and installing directory files that will contain Geant4 libraries, headers and support files, and Visual Studio 2019 (an integrated development environment for software application [143]) in Windows operating systems as a compiler platform [144]. In addition, it uses WIN32 OpenGL (a cross-platform application programming interface used for image processing of 2D and 3D vector graphics [145]) for visualization, ROOT for data analysis and Notepad++ as a text editor. Geant4 has available pre-defined functions and classes (i.e., a fundamental section of a code that has its own methods and variables) written and structured in a C++ format. Due to the extensive documentation and tools available, multiple files are created to accelerate compilation time since only the necessary information is utilized, to give structure and organization, and to separate interface from implementation [143]. In C++, the programs are built in two processes:

1. Source files (a .cpp or .cc file) are created and compiled separately, where one .cpp file is not aware of other .cpp files, but intermediate files called objects are created for each source file compiled so when all documents have been compiled and *linked*, the final main program will be generated.

2. Header files (a .h or .hh file) work as the *link* between source files to recognize other available files or make the interface visible for their use while keeping the implementation in its own .cpp file.

Additionally, text files like CMakeLists (a .txt file) contain executable creation commands and path directions between programming systems and the additional library files, whereas macro files (a .mac file) are used for automatization and visualization commands [146].

The purpose of this simulation is to provide a visualization platform for the emission tomography system proposed, as well as an analysis and validation tool

for the detection device support (tripod) described and characterized in Chapter 3. Thus, one main program is developed and utilized to construct an array of the detection device, where the detector can be re-positioned to any location of the system by employing the mathematical relations obtained in the previous section and, in this form, detect the emitted γ-rays by the sample; it is expected for the device to reconstruct the gamma source and register the energy deposited by them. For the development of this simulation, ten classes – with their respective source and header files – were created to delineate the parameters, attributes, actions and physics processes that our simulation will follow. These files are available in Appendix B while the text and macro files utilized for visualization and running initialization commands are shown in Appendix C; notice that there is an Extra Text File C.1 that contains a standard calling and path connection between CMake, Geant4, and files creation and location for executable and simulation files. Moreover, this Chapter will outline and justify the parameters chosen for developing and designing the emission tomography system, which will be divided into three sections: the Sample, the Detection Device (which includes the detector device and support), and the System Configuration.

4.1 Sample

As mentioned, an emission tomography system is constituted by a sample that emits radiation by itself, this is a sample that contains a radioactive material like a waste drum or a nuclear reactor. In this case, we are interested in samples that emit γ-rays due to their non-invasive, high penetrating and manageable directionality characteristics. In nuclear systems, this tomographic approach is often used to validate, study and analyze the system's conditions. For instance, a nuclear facility induces fission processes to produce electrical power from the energy – heat – released in these reactions. This fission reaction will occur when a free neutron collides with a larger nucleus like natural uranium (which is composed of 0.7 % Uranium-235 and 99.3 % Uranium-238) or Plutonium-239, resulting in the release of neutrons, gamma-rays, energy and unstable fission products that will continue to decay, additionally, the activation products that

result from the capture of a neutron by stable nuclei in coolant and reactor structures will decay in the form of alpha, beta or gamma emissions; thus, these products and radioactive elements are held within a specific container called vessel or calandria for CANDU (Canada Deuterium Uranium) type reactors. Because of the high penetrating characteristics of the high-energy gamma-rays and high-speed neutrons, in addition to the unstable nature of the isotopes contained, multiple measures and conditions must be maintained and promoted during all the life cycles of a nuclear facility. For example, these delineations require anticipated limits for possible deformation in the nuclear systems due to irradiation conditions, monitoring of variables and systems that can affect the fission process, and establishment of geometric models of the reactor core, internals and vessel(s). So, they must be supported by experimental data and measurements obtained through adequate and qualified analysis techniques [147]; for more information see the REGDOC-2.5.2, Version 2 or consult the CNSC (Canadian Nuclear Safety Commission) website. Furthermore, CANDU reactors are also capable of producing isotopes like Cobalt-60, which is employed in sterilization processes for medical equipment and food irradiation. Canada is one of the major Co-60 producers in the world since, for its production, the CANDU adjuster rods are substituted by neutronically equivalent Co-59 adjusters that will interact with the free neutrons contained in the reactor and produce high rates of Co-60 due to CANDU's high neutron flux and optimized fuel burn-up. However, in this exchange process, several conditions and requirements must be assessed like a minimum impact on station efficiency and reactor operations, shielding requirements during reactor operations and removal, and transportation and shipment offsite [148]. Therefore, in the same manner as in power production, inspection and internal analysis of the systems involved in these processes via quantitative and qualitative methods is necessary.

So, with the previous stated, a sample containing a Co-60 isotope was selected for analysis in this simulation. Besides the importance of Co-60 in the nuclear industry in Canada, easy access and common utilization, this substance was preferred due to its high intensity and highly penetrating gammas emitted. This artificial isotope with 27 protons and 33 neutrons decays via a β^- decay to an

excited Nickel-60, as indicated in the following reaction

$$\text{Co}_{27} \longrightarrow \text{Ni}_{28} + \text{e}^- + \bar{\nu}_\text{e}.$$
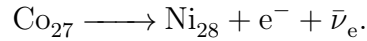
In this process, Co-60 emits an electron with an energy of 315 keV, an antineutrino, and an excited daughter Ni-60 that will emit one or two gamma rays with energies of 1.1732 MeV and 1.3325 MeV to reach a stable state. Around 1132 Ci (Curies) or 42 TBq (terabecquerels) can be emitted by one gram of Co-60; where, according to the IAEA, activities of Co-60 sealed sources for gamma irradiators and industrial gamma radiography range from 4 to 150,000 TBq, and activities in the range of one to tens of kBq are used for education and calibration purposes [149]. Thus, when handling or using radioactive substances, it is important to maintain and follow the effective dose limits determined by the regulatory institutions in Canada. The CNSC recommends following an effective dose limit for the public of 1 mSv in one calendar year, for a nuclear worker this limit is 50 mSv in any one year, and for the most exposed workers like industrial radiographers is 5 mSv per year [150]. These dose limit calculations are realized by considering the source of ionizing radiation as a point source. This is if the source is small enough to be considered a point in a space in relation to another point in the same space, where the distance between these points is at least ten times the largest dimension.

In this simulation, a Co-60 source of 3 kBq or 81 nCi, equivalent to around 0.30×10^{-18}g, is designed as the object of study in the suggested emission tomography system and contained in a 100×150 cm planar aluminum structure with 1 cm thickness. In Geant4 an event is a basic unit of simulation that represents a set of tracks and contains all the primary particles utilized in one event in order to obtain and register information about them. In this case, 30 particles are set up per event and 100 events are simulated, where assuming that this single run occurs in one second, all 3,000 particles will have decayed. Thus, to recreate this isotope's radioactive decay with the previously specified characteristics using pre-defined Geant4 classes, the following header and source files were created: **System2Construction** for the geometry and material definition of the sample; **Physics** for the definition of the physics processes

followed in the radioactive decay, which are invoked by the classes *G4EmStandardPhysics.hh*, *G4OpticalPhysics.hh*, *G4DecayPhysics.hh* and *G4RadioactiveDecayPhysics.hh*; **Generator** for the creation and definition of the Co-60 particle using *G4GeneralParticleSource*, which includes a pre-defined list of decays and their daughters, along with parameters that will define the main parameters of the source which can be called through commands in a separate .mac file; and **sim.cpp** for the initialization and visualization of the program. In addition, the text files **vis.mac** and **run.mac** are defined for visualization specifications, and for definition of the type of isotope, source position and type, respectively. See Appendix B and C for reference.

4.2   Detection Device

4.2.1   Gamma Camera

In emission tomography, a type of gamma camera is typically utilized to analyze the object of study. As mentioned in Chapter 2, which defines the main components and characteristics of this device, a gamma camera consists of a collimator, a detector (e.g., a scintillator) and a photomultiplier, where each component satisfies a particular task in the radiation detection process.

In this project, since we are interested in obtaining images of the activity distribution of an isotope that emits high-energy γ-rays, a detector device with adequate material properties must be selected. In emission tomography, this type of data is captured through a special detection device called an Anger camera, which is the most frequently used gamma-ray imager (i.e., a gamma-ray detection device that records and forms an image of the radionuclides within a sample). This gamma camera or Anger camera, in the name of its inventor Hal Anger, is composed of a collimator that will give directionality to the γ-rays, a detector that will absorb and measure its energy, and a photomultiplier that will transform the incoming data into measurable electric pulses which will conform the distribution map of the activity in the sample.

As mentioned, the objective of the detector is to absorb and measure the energy of the emitted γ-rays; thus, a device capable of transforming the energy detected into measurable quantities with high absorption capabilities is desired. In nuclear fields, an inorganic scintillator detector is commonly used in gamma cameras due to its high efficiency, high density, fast operation, low cost and variability [151]; particularly, sodium iodide (NaI) detectors. In this case, the sample to be analyzed is Co-60, a multi-gamma emitting radioactive source. So, a detector with a high energy resolution like a High Purity Germanium (HPGe) is recommended due to its accurate distinction between the closely spaced gamma lines; however, this device must be cooled at liquid nitrogen temperatures and its cost is high [69]. Although, NaI(Tl) (Thalium doped Sodium Iodide) arrays of scintillator crystals also allow distinction between simultaneously emitted gammas if they are absorbed by separate crystals in the arrangement [152]. Sodium Iodide detectors are commonly used for low and intermediate energy levels but large detector dimensions and relatively thick entrance windows allow good measurements for high-energy γ-rays [153][154]. Following this, a rectangular array of 2×4×16 inches or around 5×10×41 cm of individual NaI(Tl) rectangular detectors, conformed of 99.8% NaI and 0.2% Tl, were designed in Geant4. This design is based on the research realized by Sandia National Laboratories [152] and Pacific Northwest National Laboratory [154] for the design, characterization and performance of NaI(Tl) array detectors, and Saint-Gobain crystal scintillation products. Furthermore, the entire crystal arrangement is conformed of twelve NaI(Tl) crystals with a width of 20 cm (four crystals arranged horizontally), a height of 30 cm (three crystals arranged vertically), and a depth of 41 cm. The main function of a scintillator is to convert all the incoming ionizing radiation into optical photons that will be later transformed into electric signals by the photomultipliers; thus, the initial energy deposition and the output signal will affect the energy resolution of our device [155]. As a consequence, the number of optical photons detected by the PMT will depend on the properties of the scintillation material, energy deposition, and surface properties such as the dimensions of the sensing area or the material's ability to absorb, reflect or transmit light. The NaI(Tl) scintillator properties like

its density (3.67 g/cm^3), maximum wavelength of emission (415 nm), refractive index (1.85), decay time (250 ns), and light yield (38 photons/keV) is added to the properties of our crystal in the materials and properties section of the source file ***System2Construction***, and obtained from the Material Sheet of Saint-Gobain Crystals [151]. Since this scintillation light must be channeled or directed to the PMT for its conversion to electrical signals, we want to reduce any light loss to avoid the reduction in signal-pulse height, the decrease of low-energy sensitivity and energy resolution [70]. Therefore, a reflective coating is placed around each scintillator to reflect the energy back to it. In addition, the when a gamma finish can be modified to increase the internal reflection [70], to add this coating and characteristics to the scintillator in the simulation, a class named *G4Opticalwhen a gamma* is utilized. This class allows the specification of the object's physical when a gamma and models the interactions with it [156]. In this case, a "skin surface" surrounding the logical volume (the scintillator and the PMT) is assigned through the class *G4LogicalSkinSurface*, where the UNIFIED model is selected to describe the physics processes of an optical photon that interact with the properties of a dielectric surface; and, it manages the surface finish and reflector coating. A dielectric-metal surface is selected to simulate a mirror-type property, where the processes will be controlled by the surface finish, reflectivity and efficiency; here, the predetermined reflectivity is one and will reflect all the photons that interact with this surface. Additionally, to ensure absorption or reflection at the surface, a rough (ground) finish is preferred. Moreover, to allow or guide the scintillation light to enter the PMT, a glass window is placed between the scintillator and the PMT. The reflective coating does not get in contact with the scintillator and the PMT because transmission of scintillation light is desired in this area [70]; thus, a material like beryllium (Be) or aluminum are typically used for this component. So, a 2 mm thick Al entrance window with reflectivity of 8% for visible light was added to the system. See the materials and properties section in the ***System2Construction*** class in Appendix B. Finally, this device must be covered by an aluminum (Al) casing for protection from external light, atmospheric moisture and possible external damage, while it shields the crystal from alpha and low beta radiation [157]. For

this simulation, the Al casing will be covering the individual scintillator crystal with a case of 0.05 cm for each side, and the crystal array, entrance glass and photomultiplier to avoid interference between these optical components, thus a cylindrical Al casing of radius 12.75 cm and length of 66.60 cm is defined in the class ***System2Construction***.

Furthermore, the device responsible for transforming all the incoming photons into measurable electric signals is the photomultiplier (PMT). This device is conformed of a photocathode, an electron-optical input system, an electron multiplier and an anode grid, that are enclosed in a vacuum tube made of glass. One of the main parameters to consider while selecting a PMT is the emission spectrum of the detector device, since it directly affects the PMT's sensitivity [158]. Following the research performed by Sandia National Laboratories [152] and Saint-Gobain existent products, cylindrical photomultipliers for each scintillator of 8.9 cm and length of 25 cm were selected for this simulation. However, due to geometry difficulties and process specifications, rectangular photomultipliers of 5×10×66.4 cm were designed. As mentioned above, the objective of this device is to obtain measurable data in the form of a current pulse (or wave) from the γ-rays emitted by the sample. Nevertheless, in Geant4, a particle that goes through a detector is treated as a classical particle (i.e., a point-like object with defined momentum and position), and not like a wave function [159]. So, to overcome this, a special class called *G4VSensitiveDetector* is employed to perform an approximation of the detector and the PMT functions of absorbing, detecting and measuring the incoming energy of the emitted photons. When this class is assigned to a volume, it generates "hits" for every single step of every single track, where the hits can provide information of the detected particle like its position and time, energy deposition of a step, and track ID; at the same time, a hit can accumulate information of each volume for all steps of all tracks like the sum of deposited energy or the volume ID [159]. Following this, a volume or shape for the photomultiplier is created for visualization purposes but the functions and processes are managed by the class ***SensitiveDetector***, which invokes the main class *G4VSensitiveDetector*; see Appendix B. In the designed class ***SensitiveDetector***, the detector position is

obtained with the class *G4VTouchable* since it gives a unique identification number for the detector element inside of the main world [156]. Thus, for a simulation of a screen conformed of detectors where the step or moment when the photon enters or gets in touch with the volume that defines the detector, the class *G4VTouchable* will be able to obtain and print the exact detector location that the photon hit. Consequently, the volume considered the sensitive detector as the volume that encloses the scintillator and photomultiplier.

The last component designed for the suggested gamma camera is a collimator. A collimator is utilized to separate the γ-rays that travel in a straight line from the ones that do not; in other words, it defines a parallel direction for the γ-rays. This device allows the acquisition of accurate spatial information concerning our sample, where this information works as the connection between location, sample and activities, and it will graphically represent the source, location and form in which each event occurs [160]. A collimator has the shape of a plate made of a high Z material (or gamma absorber) with a number of holes or apertures. The collimator's thickness, type of material, shape and dimension of the apertures, and distance between apertures will define the properties of the device like its resolution, field-of-view (FOV) and efficiency. Since we are dealing with high-energy γ-rays, a material with a high atomic number is necessary, so those not useful gammas get completely absorbed by the material; thus, materials like lead (Pb), tungsten (W) and platinum (Pt) are used. The most utilized material in collimators is lead due to its low-cost, easy manufacture and high density yet, materials like tungsten have a higher atomic number, which reduces the collimator's required thickness but becomes more difficult to cast or machine; however, they can be more effective in the γ-ray absorption process [69]. Moreover, it can be said that there are four types of collimators: pinhole, parallel hole, diverging and converging. The most widely utilized collimator is the parallel hole, it makes a projection of the same size as the source distribution, and consists of holes or apertures parallel to each other and perpendicular to the crystal scintillator [160]. The distance between each aperture is called septa, and its objective is to capture most of the rays that are not traveling in a straight line so, for high-energies, this distance is greater than for low-energies; and, it is preferred that no more than 25 % of the radiation be absorbed [161]. Then,

to determine the entrance aperture several parameters must be considered like the hole shape, length and diameter. These apertures can have circular, hexagonal, rectangular and triangular geometries, where the hexagonal geometry is considered the most efficient because it fills most of the space – compared to other shapes – with equal size units [160]. The size of the holes will determine the resolution of the collimator thus, for high resolutions there are more and smaller holes per area, leading to a lower sensitivity [69]. As a consequence, compromises, limitations and ranges must be defined according to the objective of the study and the equipment used. In the simulation for this collimator (see the Collimator section of the class **System2Construction**), a parallel hole collimator made of 20 mm of tungsten was chosen to ensure the absorption of unwanted γ-rays. It contains cylindrical holes with an aperture of 4 mm, which is based on the paper by Razavi *et al.* [162] for the characterization of low, medium and high energy collimators. This plate is placed in front of the scintillator with one entrance per scintillator array, thus a matrix of 3×4 holes is depicted per detector.

4.2.2   Tripod (Support)

Studies that utilize an emission tomography approach need an array configuration of detectors at different angles of the sample to capture data to the greatest extent, so estimations of activity distributions could be made. Depending on the shape, dimensions and mobility of the sample, two data acquisition techniques can be employed, where a stationary technique could be used for objects with comparable dimensions to the detector's field of view and with systems that utilize several detectors placed around the sample, and a scanning technology where there is a need for generation of more views or angles due to limited detector dimensions. While performing scanning motions, the detector or sample movement must define an accurate and precise pattern around the object of interest to reduce poor temporal resolution and to provide a good signal-to-noise ratio. In this case, we are interested in γ-ray samples held in containers of considerable dimensions; thus, a limited angle gamma emission tomography system can be employed for its analysis, where the field-deployable detector device will move around the sample. It is said that the approach is limited when

the sample's dimensions are exceedingly large for the detector's field of view, and the mobility and orientation of the sample are constrained, so the number of obtained angles is partial. In this case, to physically compensate for these constraints, a mechanical mounting support for the detector device is proposed; in order for the system to provide additional detector positions, and is a consequence of the tripod's legs' independent transformations or motions. The suggested support or base will consist of three stainless steel legs capable of maintaining stability and supporting the weight of the gamma camera; for more specifications on the supporting stand review Chapter 3.

In this simulation, the supporting device was designed by creating three cylinders of 100 cm of stainless steel with 1 cm of diameter and one sphere of the same diameter as the legs. It is important to mention that Geant4 predetermined 3D Cartesian coordinate system, position the positive y-axis upwards, the positive x-axis to the right, and the positive z-axis facing the viewer; and, the predetermined position for any figure is at the center of the main volume, where the center of each shape is at half of its own volume (e.g., a cylinder of 100 cm is originally positioned at the center of the main world, where 50 cm are in the positive side of the x-axis and the other 50 cm are in the negative side of this axis). Since the three legs share the same point of reference, they will rotate in reference to the same y-axis, one leg will perform a rotation of $2\pi/3$ radians, a second leg a rotation of $4\pi/3$ radians, and a third one a $6\pi/3$ radians rotation. Then, to give height to this configuration, a rotation with respect to the x-axis is necessary. The angle of rotation is chosen to be $\pi/4$ to delineate a standard and equal angle distribution between the directional angles of the system; however, due to the initial reference point, the angle of rotation is -$\pi/4$ radians and the new height is around 70.71 cm. Finally, to re-arrange these cylinders in a desired tripod shape, linear transformations must be applied using the angles that describe the system and its length. The resulting position matrix for each leg is delineated in Appendix B in the class ***System2Construction***. Lastly, to place together these volumes, a class named *G4UnionSolid* for boolean solids (i.e., two solids formed by a boolean operation: union, intersection or subtraction [156]) is utilized. Because this class only allows the union of two volumes, if we want to

maintain the defined position matrices for each leg, the union must be done separately since the origin and coordinates of the combined solid are the same as those of the first solid [156]. Therefore, a sphere of the same diameter as the cylinders is defined to combine and place the first leg with its respective position matrix, later the second leg is joined to the first union, and finally the third leg is joined to the second union, resulting in a tripod or triangular pyramid shape with an apex in the point (0,0,0) or origin.

4.3 System Configuration

The previous sections of this chapter have outlined, described and defined important parameters for each component of a gamma-emission tomography system for large dimensional samples. Therefore, this last section will place together the sample of interest and the detection device with its support (tripod) designed for visualization and testing of the expected and desired behavior of each component.

To summarize, emission tomography is a non-destructive analysis technique commonly utilized for the inspection and cross-sectional visualization of systems, to analyze their functionality or natural behavior. The overall configuration of this system contains a radioactive sample and a detector device, where the latter must acquire as much data as possible from the object of study. This information can be obtained through different means, either by placing multiple detector devices around the sample or by the motion of the detector or sample. The goal of this process is to obtain information about the sample from different positions or angles, where the data can represent the spatial distribution of properties of the radioactive substance. Therefore, the data acquisition process is of great importance. In cases where the detector device is moving around the sample and the latter is static, a defined pattern must be followed by the detector, ideally in a complete 360 degree range around the sample; however, this is not always possible, especially for in-situ analysis. For example, in nuclear systems, a desired object of study is the reactor core whose dimensions are around 6 m in length and 6.3 m in diameter for CANDU-6 type of reactors, or the calandria, which

contains the reactor core, with dimensions of 6 m long and around 7.6 in diameter. So, a complete analysis is difficult to perform or not possible, thus only partial information is obtained. Nevertheless, a limited-angle tomography approach can be utilized to overcome this limitation, where the optimization of iterative image processes can compensate for the imaging artifacts consequence of the limited data [125]; additionally, utilization of mechanical mounting supports can provide flexibility and accessibility to detector devices for in-situ analysis, besides of accurate and precise positioning of the device. Following this, we are interested in the delineation, characterization and visualization of a mounting support for the detector device employed in a limited-angle tomography technique for the analysis of large gamma-emitting samples, frequently found in nuclear facilities; where this support could provide accuracy and flexibility to the detector positioning in the data acquisition process.

In this Chapter we have previously described and computationally designed, in an object-oriented platform called Geant4, the individual components of a gamma emission tomography system. So, to visualize and evaluate the performance of each component and the analysis system, a set of actions are tested utilizing the computational simulation of the entire system. These actions will test the suggested tripod's mobility by utilizing the mathematical expressions described on Chapter 3, and will evaluate the ability of the detection system to capture information from the radioactive sample. Therefore, a main volume or "world" of $3 \times 3 \times 3$ m filled with air is designed to contain and locate an aluminum planar container of 100×150 cm with 1 cm of thickness that holds a gamma-emitting source of 3 kBq of Co-60, a gamma camera of 67.2 cm length and around 36.53 cm of diameter attached to a three-leg stainless steel support of 70.71 cm height when opened at an angle of $\pi/4$ radians in respect to the surface and with a $2\pi/3$ radians angle between each leg or a distance of around 173.20 cm at the surface level. Moreover, distances of 50, 40 and 30 cm between the sample and gamma camera were chosen deliberately; by considering that the field-of-view (FOV) of a parallel-hole collimator is of the same size as the collimator's area, the image projected will be the same size as the source distribution onto the detector; and, the source-to-collimator distance will not change the total counting rate due to the mutual cancellation of hole size

and radiation transmission effects [76]. Furthermore, to cover 180 degrees (or the entire front side) of the container, a distance of minimum 50 cm is required since the sample is 100 cm wide. See Appendix B, ***System2Construction*** for reference.

Chapter 5

Results and Discussion

Throughout Chapter 2, Chapter 3 and Chapter 4, multiple definitions, and mathematical and computational methods have been presented to delineate, characterize and visualize a limited-angle emission tomography system that could be used to analyze and reconstruct the activities of a gamma source (e.g., a Co-60 isotope, widely utilized in medical fields for sterilization of products and, in its majority, produced by CANDU reactors) maintained in large containers. Thus, several scenarios were created to observe and analyze the ability of the gamma camera to localize the radioactive source, register the energy deposited, and to re-position its location in the volume by means of transformations applied to the leg's matrix position, and in reference to the mathematical model previously defined. Therefore, this Chapter outlines and discusses important quantities obtained in each case and the possible interpretation or relation to the objective stated for our model. However, a Geant4 simulation is not the only method at hand with the ability to verify the field-deployable detector system's positioning. For instance, there are mathematical-based softwares that focus on predicting and evaluating the behavior of a system or design. Nevertheless, Geant4's ability to simulate particle interactions with matter was preferred in order to obtain further insights into the tomographic approach, along with its capacity for inputting extended and user-defined mathematical expressions, to visualize the transformation matrices and detector positionings.

As stated, the objective of the design of a detector and sample in a computational simulation is to observe and analyze the ability of a pre-defined gamma camera, that utilizes a tungsten collimator and an array of NaI(Tl)

scintillators, to reconstruct the isotope's distribution on the sample and register the energy deposited in the device by means of a limited-angle emission tomography system. Therefore, four cases were determined according to different source distributions:

1. Case 1. A plane circular 3 kBq source of 3 cm diameter, positioned at the point (0,0,0).

2. Case 2. A plane square 3 kBq source of 3×3 cm, positioned at the point (40,70,0).

3. Case 3. Two plane circular sources of 1.5 cm radius and 1.5 kBq each, positioned at the points (25,0,0) and (-25,0,0).

4. Case 4. A cylindrical volume of 1.5 cm radius and 1 cm height of 3 kBq and placed at the point (0,0,0).

For Cases 1 and 2, the center of the detector was placed parallel and aligned with the position of the sources while for Case 3 and Case 4, an array of one row of detectors was placed around the sample. In all cases, the distance between the sample and the gamma camera was 50, 40 and 30 cm. Moreover, in this simulation, the energy deposited per particle in the gamma camera was registered using the ***Event*** class, the initial source distribution was reconstructed with the class ***Tracking*** and the **run.mac** file for source and running specifications, the position where the photon hits the detection device is registered by the class ***SensitiveDetector***, and the captured information and creation of histograms is done through ***Run***.

5.1 Case 1

A plane circular source of radius 1.5 cm with activity of 3 kBq was defined in the **run.mac** file and placed at three different distances; and, figure 5.1 depicts the Co-60 source dispersion on the 100×150 cm container. At 50 cm only 24 particles of 36,526 entries deposited energy in the system. However, the lowest energy registered was 6.31 keV for the detector at a distance of 40 cm; and the highest energy was 962.38 keV for the 30 cm distance, which registered 65 particles.

Following the same trend, at the distance of 50 cm only 556 photon positions were captured while at the shortest distance, a location of 1,668 photons was achieved; see the histograms in figure 5.2 for each distance.
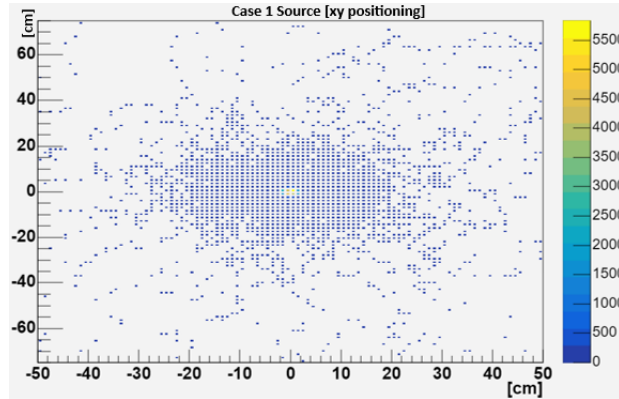
FIGURE 5.1: Histogram of the x and y positions of a 3 kBq Co-60 source with 44,245 entries, distributed in a plane circle of 3 cm diameter.

(A) Detector at a distance of 50 cm

(B) Detector at a distance of 40 cm

(C) Detector at a distance of 30 cm
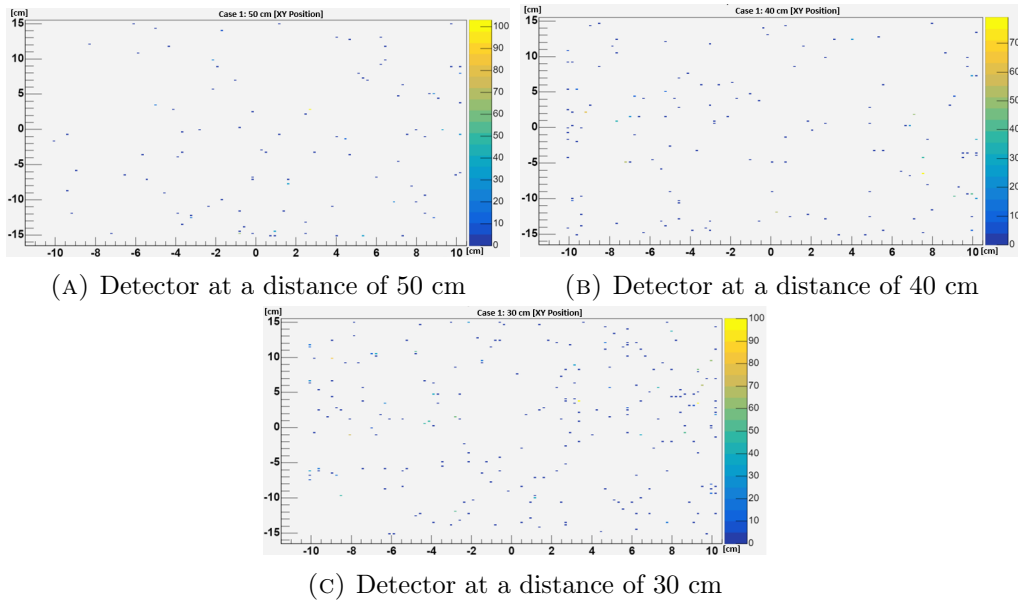
FIGURE 5.2: Histograms of the x and y positioning of the photons detected for Case 1 by a gamma camera of 20.3×30.2 cm.

To obtain the previous results, a rearrangement of the gamma camera and the tripod was needed since, initially, the camera's center was positioned 88.97 cm above the surface. Thus, the new positioning is at a height of 75 cm, assuming that the aluminum container is positioned on the surface; this is, the source center is 75 cm above the surface. To achieve this, a Scaling matrix (see equation 3.9) in the z direction with a factor of 0.80 was applied to each leg, where aperture angles of $\pi/4$ radians in respect to the surface and angles of $2\pi/3$ radians between each leg were maintained. And, the system configuration in figure 5.3 was obtained for this case.
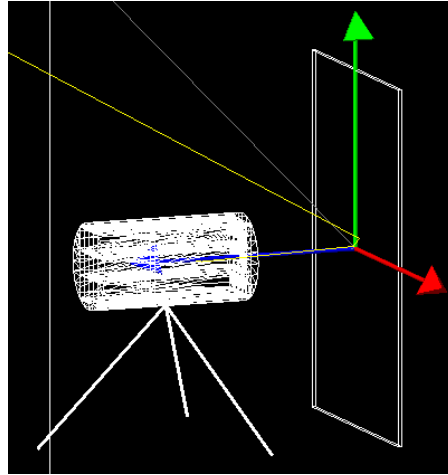
FIGURE 5.3: System configuration for Case 1. The gamma camera and sample's center are parallel to each other and 50 cm apart, where one Co-60 particle emits two gamma rays (yellow beams), one beam enters the detection system while the other is lost in the exterior (main world).

Notice that in the **System2Configuration** a Scaling matrix was not defined since only a scaling factor applied to the leg's length was necessary to obtain the new height.

5.2   Case 2

For a plane square source of 3×3 cm with an activity of 3 kBq at 30 cm (see figure 5.4), 66 particles were captured but at 50 cm, with only 0.07% energies deposited

of 35,911 entries, a peak of 1,078.97 keV was registered. However, 1,180 and 1,174 photon positions were captured at 30 cm and 40 cm respectively, and only 910 were obtained for 50 cm (see figure 5.5).
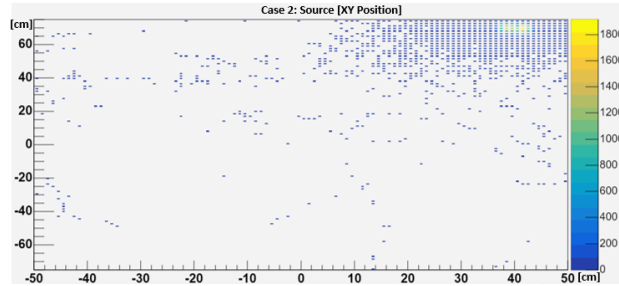
FIGURE 5.4: Histogram of the x and y positions of a 3 kBq Co-60 source with 46,988 entries, distributed in a plane square of 3×3 cm.

To reposition the gamma camera, several methods could be applied but only two are described:

- If the initial angles are maintained, the legs must be stretched and translated. For this case, the stretching factor is given by 1.79 and the translation of the

(A) Detector at a distance of 50 cm

(B) Detector at a distance of 40 cm

(C) Detector at a distance of 30 cm

FIGURE 5.5: Histograms of the x and y positioning of the photons detected for Case 2 by a gamma camera of 20.3×30.2 cm.

entire system is described by the Translation matrix in equation 3.7 applied on the x-axis by 40 cm.
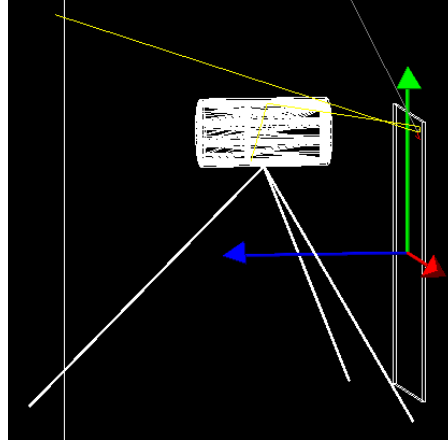
FIGURE 5.6: System configuration for Case 2. The gamma camera and sample's center are parallel to each other at the point (40,70,50), where one Co-60 particle emits two gamma rays (yellow beams). One beam is lost in the exterior while the other interacts with the aluminum container and is re-directed to the gamma camera; the grey beam represents an emitted anti-neutrino and the red beam is an electron.

In the same form as the Stretching matrix, the Translation matrix is represented by the positioning vector of the tripod's physical volume at the point 40 cm on the x-axis, see the section Placement in **System2Construction**.

- If one directional angle is maintained and two are changed, stretching of three legs and translation of one leg is needed. In this case, re-definition of the angles, length of the legs and re-positioning in the x-axis is necessary. To perform the change in the angles, the Rotational matrix (see equation 3.6) in the x-direction is applied to the angles 31.49 degrees or 0.1749π radians for one leg, and 69.81 degrees or 0.3878π radians for the second. On the other hand, the new length of both legs was obtained using the new angle and the equations delineated in 4 these two parameters. Finally, for the third leg, a translation of 40 cm and a stretching factor of 1.79 is utilized; see figure 5.7.
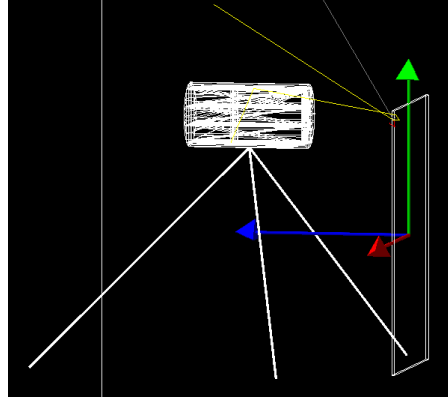
FIGURE 5.7: System configuration for Case 2. The gamma camera and sample's center are parallel to each other at the point (40,70,50), where one Co-60 particle emits two gamma rays (yellow beams). Notice that the two front legs have different directional angles and lengths while the leg from the back remains the same, in comparison to figure 5.6.

Since in this case, the angle and lengths had to be re-defined, it was preferred to calculate the angle and length utilizing the equations obtained in 4, and apply directly to the leg's positioning matrices. No changes were applied to the original matrix however, the first leg re-positioning had correction errors due to its change in the x-axis. Moreover, if the system is desired to be placed at the point (-40,70,50), the same angles and lengths defined for the point (40,70,50) are used but exchanged between the first and second leg.

5.3 Case 3

In this case, two plane circular sources of radius 1.5 cm and activity of 1.5 kBq each were positioned at the points (25,0,0) and (-25,0,0); see figure 5.8 for visualization of the sources distribution on the container.

The energy deposition for the three distances had entries of 58,026, 63,135 and 69,092 for 50, 40 and 30 cm respectively, where the highest energy deposition is obtained at 50 cm with a value of 1,504.93 keV; however, the 40 and 30 cm had their highest peak at 979.86 and 920.66 keV. In this arrangement, one row of nine, seven and five gamma cameras were positioned around the sample at 50, 40 and
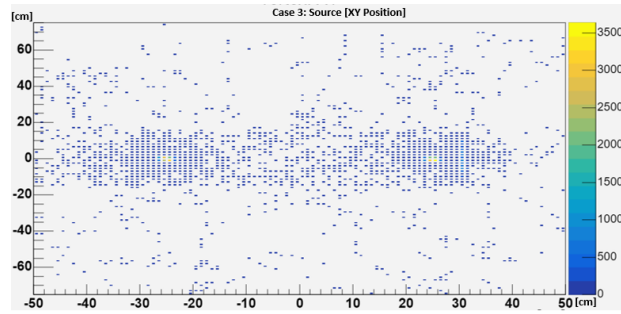
FIGURE 5.8: Histogram of the x and y positions of two 1.5 kBq
Co-60 sources with 58,688 entries, distributed in a plane circle of 1.5
cm radius each.

30 cm each. Each detector was placed next to the other with a gradual rotation of 7.74, 6.19 and 4.64 degrees for 50, 40 and 30 cm. And, the number of devices was determined by the dimensions of the camera and the distance between each detector and the center of the sample. So, at a distance of 50 cm, nine detectors were able to cover around 157 degrees of the container's width. Nevertheless, for 40 cm only 125 degrees were covered but a capture of 4,468 photon positions was achieved. Finally, with approximately 52.35 cm covered, entries of 7,338 photon positions were registered at a 30 cm detector and sample distance. Figure 5.9 shows the respective histograms for the x and y photon positions at each case.

5.4 Case 4

Lastly, in Case 4, a cylindrical Co-60 source of 3 kBq with a 1.5 cm radius and 1 cm height was positioned at the point (0,0,0) for its analysis. In figure 5.10, the source distribution for its x and y positions is represented by a histogram. Following the same detector arrangement as Case 3, the number of entries for 50 cm was 56,549 with its highest energy at 841.23 keV, for 40 cm at 750.53 keV and the lowest energy at 0.67 keV, and for 30 cm with 63,701 entries a peak of 732.81 keV was registered. In the same form, at 30 cm 4,127 photon positions were registered but only 2,482 were obtained at 50 cm; see the figure 5.11 for reference.

(A) Detector at a distance of 50 cm

(B) Detector at a distance of 40 cm

(C) Detector at a distance of 30 cm

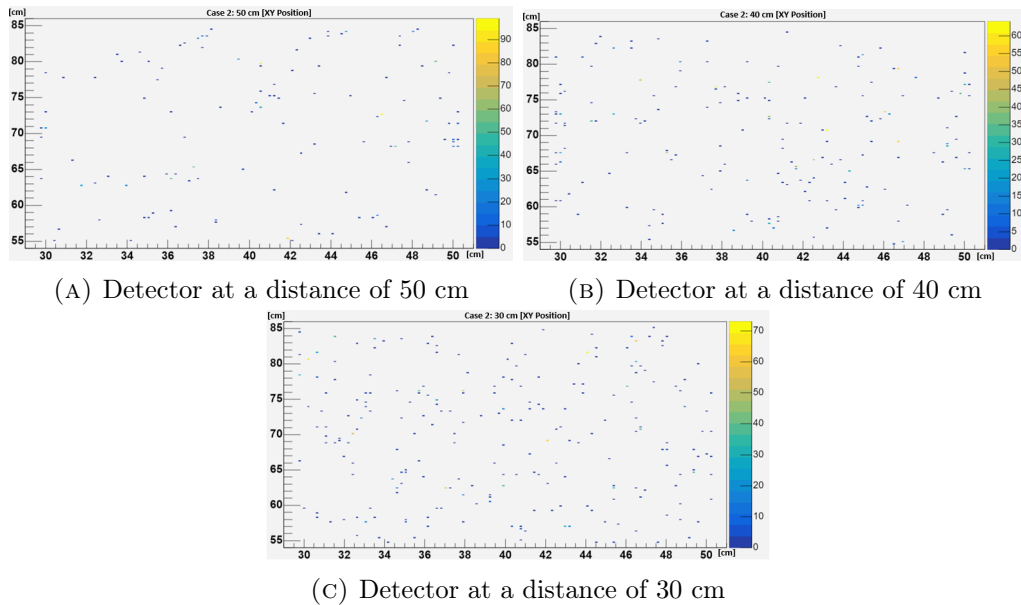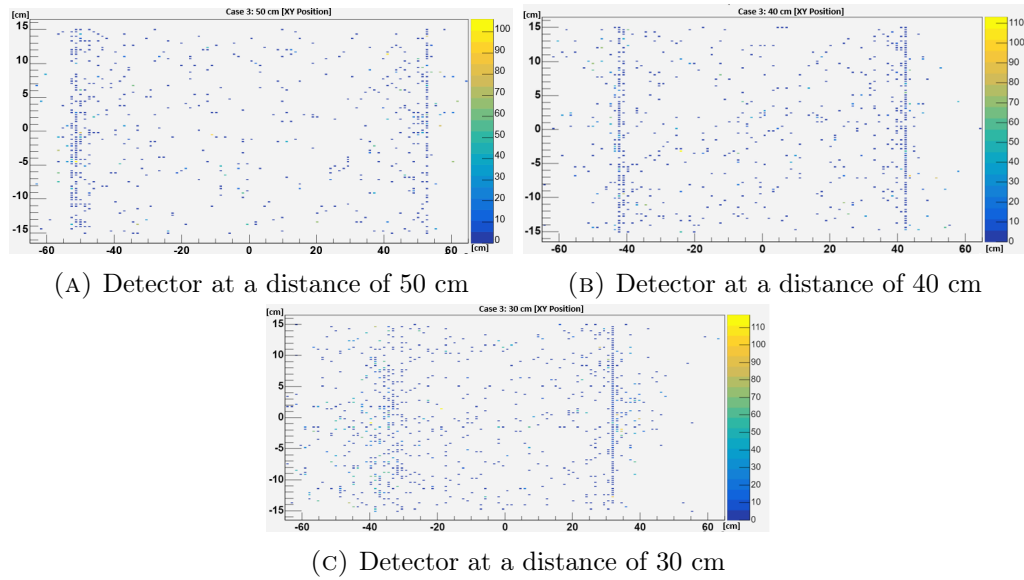FIGURE 5.9: Histograms of the x and y positioning of the photons detected for Case 3 by a gamma camera of 20.3×30.2 cm.
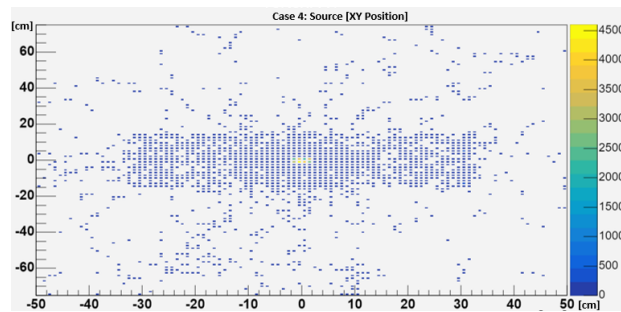
FIGURE 5.10: Histogram of the x and y positions of one 3 kBq Co-60 sources with 54,334 entries, distributed in a cylinder of 1.5 cm radius and 1 cm height.

(A) Detector at a distance of 50 cm

(B) Detector at a distance of 40 cm

(C) Detector at a distance of 30 cm
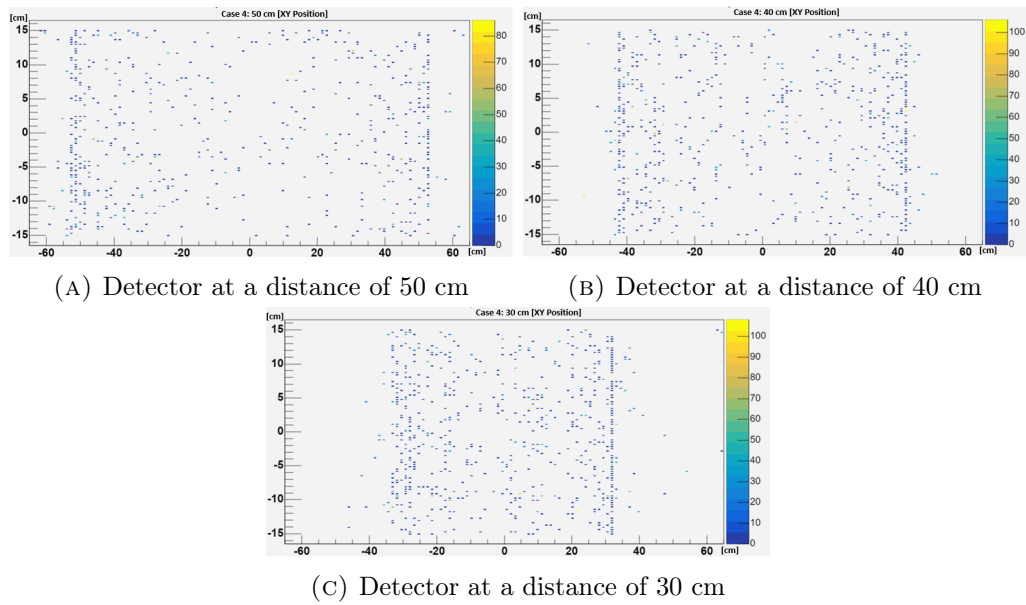
FIGURE 5.11: Histograms of the x and y positioning of the photons detected for Case 4 by a gamma camera of 20.3×30.2 cm.

Chapter 6

Conclusion

Overall, as mentioned, the objective of this thesis has been to delineate a support structure for a detection device utilized in an emission tomography system for in-situ analysis of gamma samples, which are typically held in specific large containers. It is expected for this tripod support to provide flexibility and accuracy to in-site measurements, and not alter nor intervene with the gamma camera performance. Therefore, a mathematical model that characterizes the support and camera, and a computational simulation that visualizes and manipulates the support and camera were designed to evaluate their performance. Following the typical Engineering Design Process, background research, requirements and standards, and analysis and evaluation steps were implemented throughout the development of this work. The background research is presented in Chapter 1 and Chapter 2, the requirements and standards have been outlined along with the theory in Chapters 1 and 2, and the analysis and evaluation have been developed through Chapter 3 and Chapter 4 while Chapter 5 has outlined the results obtained.

Following this, four cases are suggested in Chapter 5 to analyze and evaluate the proposed methods; where linear transformations due to the tripod's motion were required, and capture and registry of photon's position and energy deposition utilizing the functions of a gamma camera were determined. All the cases, except Case 4, describe plane sources of a maximum 3 cm diameter or length to obtain at least a ten-times difference between the sample-detector distance and the source emission area. This is, to approximate these sources to a point source where the maximum energy delivered will be 32.49 pSv per second at 30 cm, which is around

1.02 mSv per year and is below the effective dose limit of 50 mSv for radiation workers. Moreover, since we are dealing with an unstable atom, dispersion due to interactions with the medium and natural decay of the isotope will be observed throughout the container. Thus, for each case, a histogram of the initial source xy positioning is depicted by the figures 5.1, 5.4, 5.8, and 5.10. Even though all figures appeared to be distributed through all the 100×150 cm container's area, a concentration point marked by yellow tones is limited to a range of 3 cm, and delimiting the photon's origin. Furthermore, it is evident that greater quantities of photon positions and energy depositions are registered for closer distances between the sample and the gamma camera, which leads to better source definition and, therefore, better spatial resolution and high sensitivity (count rate). For Cases 1 and 2, the detection device had to be re-adjusted to a centered position in parallel to the radioactive source. Thus, linear transformations and formulations determined in Chapter 4 were utilized for the specification of stretching factors, rotational angles, and translations. Yet these formulations are precise, and a wide possibility of configurations are possible, a set of limitations must be set or a leg's parameter must remain constant to create a motion pattern. Moreover, in Cases 3 and 4, a constant rotation with respect to the y-axis around the sample was performed to determine the extent of angles obtained at a 50, 40 and 30 cm distance. It is noticed that for Case 3, at a distance of 30 cm better distinction between sources is achieved; however, in Case 4, is clear that a great area is covered by a distance of 50 cm, but a major photon count is perceived on the left side of the sample which can be attributed to a detector array that covers a greater extent of the right side of the sample.

Additionally, it must be mentioned that contrast resolution, spatial resolution and sensitivity are important factors in an emission tomography system, which are affected by the detector size, collimator dimensions, material and design, photomultiplier sensitivity and compatibility with the detection device, sample dimensions and thickness, distance between gamma camera and sample, and others. Therefore, an active exchange and compromise between dimensions, materials and goals must be accepted. Following this, a further and detailed study of the gamma camera design is desired to set boundaries and enhance

possible limitations or weaknesses that have not been noticed through this work. In addition for experimental and physical analysis of the suggested method that will provide real and tangible results to in-situ measurements.

Finally, as mentioned, a Geant4 simulation is not the only verification tool available and applicable for the validation of the detection device assembly. Thus, in the same form, the shape of the support is not the only way of obtaining flexible and accurate detector positioning but, due to the better support than a two-leg stand and easier parametrization than a four or five-leg stand along with its easily adaptable legs and control, this design was chosen. Nevertheless, the intention of this work is to suggest a self-reliant mechanical support that could facilitate the data acquisition process in a tomography system but limitations, restrictions and uncertainties will be always found since no system is ideal for every type of analysis. Thus, further study and comparison with traditional scanning techniques must be performed in order to obtain a full validation of its usage in the nuclear energy industry. However, the system design has shown accurate and flexible movement on the detector device with a simple, manageable and easy-to-transport support, characteristics that are an ongoing interest in safeguards measures for on-site inspections; therefore, it can be said that further study of the feasibility and performance of this field-deployable detector device would be advantageous and beneficial to the nuclear industry.

Bibliography

[1] *Iaea safeguards overview*, 2014. [Online]. Available: https://www.iaea.org/publications/factsheets/iaea-safeguards-overview.

[2] U. Busch, *Wilhem Conrad Röntgen. A Shining Life for Science*. Remscheid: Birkhäuser, 2020, ISBN: 978-3-030-72242-5.

[3] E. Beckmann, U. Bush, F. Duck, A. Thomas, and R. V. Tiggelen, "The story of radiology," European Society of Radiology (ESR), Austria, Tech. Rep., 2014.

[4] N. L. Mishra, "125th Year of the discovery of x-rays," Science Reporter, Navi Mumbai, Tech. Rep., 2021.

[5] H. E. Martz, C. M. Logan, D. J. Schneberk, and P. J. Shull, *X-Ray Imaging. Fundamentals, Industrial Techniques, and Applications*. U. S.: CRC Press, 2017, ISBN: 9780849397721.

[6] R. F. Mould, "The early history of x-ray diagnosis with emphasis on the contributions of physics 1895-1915," *Physics in Medicine & Biology*, vol. 40, no. 11, p. 1741, 1995. DOI: 10.1088/0031-9155/40/11/001.

[7] P. Sprawls, "Film-screen radiography receptor development a historical perspective," *Medical Physics International*, vol. Special Edition, no. 1, pp. 56–81, 2018, ISSN: 2306-4609.

[8] U. Ewert, U. Zscherpel, and K. Bavendiek, "Replacement of film radiography by digital techniques and enhancement of image quality," *e-Journal of Nondestructive Testing*, 2007, ISSN: 1435-4934.

[9] E. Carter, B. Swarbrick, and Harrison, "Rapid identification of cellulose nitrate and cellulose acetate film in historic photograph collections," *Heritage Science*, vol. 8, no. 51, 2020, ISSN: 2050-7445.

[10] Y. V. Kuznetsov, *Principles of Image Printing Technology.* Springer Cham, 2021, ISBN: 978-3-030-60955-9.

[11] M. Sarfraz, *Digital Imaging.* Rijeka: IntechOpen, 2020, ISBN: 978-1-78985-600-2. DOI: 10.5772/intechopen.83239.

[12] A. R. Weeks, *Fundamentals of Electronic Image Processing.* U.S.A.: Wiley-IEEE Press, 1996, ISBN: 9780470544709.

[13] B.-A. Jönsson, "Henri Becquerel's discovery of radioactivity − 125 years later," *Physica Medica*, vol. 87, pp. 144–146, 2021, ISSN: 1120-1797. DOI: https://doi.org/10.1016/j.ejmp.2021.03.032.

[14] R. A. Serway, C. J. Moses, and C. A. Moyer, *Modern Physics.* U.S.A.: Brooks/Cole - Thomson Learning, 2004, ISBN: 0-534-40624-6.

[15] N. Pasachoff, *Marie Curie and the science of radioactivity*, [Website], Center for History of Physics, 2000.

[16] P. Radvanyi and J. Villain, "The discovery of radioactivity," *Comptes Rendus Physique*, vol. 18, no. 9, pp. 544–550, 2017, Science in the making: The Comptes rendus de l'Académie des sciences throughout history, ISSN: 1631-0705. DOI: https://doi.org/10.1016/j.crhy.2017.10.008.

[17] M. Malley, "The discovery of the beta particle," *American Journal of Physics*, vol. 39, no. 12, pp. 1454–1461, 1971. DOI: 10.1119/1.1976694. eprint: https://doi.org/10.1119/1.1976694.

[18] L. Gerward, "Paul Villard and his discovery of gamma rays," *Physics in Perspective*, vol. 1, no. 4, 1999. DOI: 10.1007/s000160050028.

[19] H. Paetz gen. Schieck, *Key nuclear reaction experiments : discoveries and consequences* (IOP expanding physics). IOP Publishing, 2015, ISBN: 9780750311731.

[20] C. Anderson, X. Ling, D. Schlyer, and S. Cutler, "A short history of nuclear medicine," in Apr. 2019, pp. 11–26, ISBN: 978-3-319-98946-4. DOI: 10.1007/978-3-319-98947-1_2.

[21] J. D. Rogers, "The neutron's discovery - 80 years on," *Physics Procedia*, vol. 43, pp. 1–9, 2013, The 7th International Topical Meeting on Neutron Radiography (ITMNR-7), ISSN: 1875-3892. DOI: https://doi.org/10.1016/j.phpro.2013.03.001.

[22] E. O. Lawrence, "Artificial radioactivity," University of California, 2004.

[23] M. Thoennessen, *The discovery of isotopes: a complete compilation.* Switzerland: Springer, 2016, ISBN: 331931761X.

[24] C.-H. Yeong, M.-h. Cheng, and K.-H. NG, "Therapeutic radionuclides in nuclear medicine: Current and future prospects," *Journal of Zhejiang University - Science B*, vol. 15, no. 10, 2014, ISSN: 1862-1783. DOI: 10.1631/jzus.B1400131.

[25] H. Gest, "The early history of 32P as a radioactive tracer in biochemical research: A personal memoir," *Biochemistry and Molecular Biology Education*, vol. 33, no. 3, pp. 159–164, 2005. DOI: https://doi.org/10.1002/bmb.2005.494033032427.

[26] W. H. Organization, "100 years of radiological science: X-rays 1895-1995: Radioactivity 1896-1996," *World Health*, vol. 48, no. 3, pp. 1 –31, 1995-05.

[27] M. J. Dykstra, "Autoradiography," in *Biological Electron Microscopy: Theory, Techniques, and Troubleshooting.* Boston, MA: Springer US, 1992, pp. 321–331, ISBN: 978-1-4684-0010-6. DOI: 10.1007/978-1-4684-0010-6_16.

[28] W. G. Bradley, "History of medical imaging," *Proceedings of the American Philosophical Society*, vol. 152, no. 3, pp. 349–361, 2008, ISSN: 0003049X.

[29] F. Guerra, M. Leone, and N. Robotti, "The discovery of artificial radioactivity," *Physics in Perspective*, vol. 14, no. 1, 2012, ISSN: 1422-6960. DOI: 10.1007/s00016-011-0064-7.

[30] "Radiopharmaceuticals: Production and availability," International Atomic Energy Agency (IAEA), Austria. [Online]. Available: https://www.iaea.org/sites/default/files/gc/gc51inf-3-att2_en.pdf.

[31] R. Behling, "X-ray tubes development iomp history of medical physics," *Medical Physics International*, vol. 1, pp. 8–55, 2018, ISSN: 2306-4609.

[32] J. Kissane, J. A. Neutze, and H. Singh, "Introduction to imaging & technology," 2020.

[33] C. J. Giunta and V. V. Mainz, "Pioneers of magnetic resonance," *ACS Symposium Series*, vol. 1349, no. 1, pp. 3–20, 2020, ISSN: 9780841237100.

[34] J. Terry and D. Townsend, "History and future technical innovation in positron emission tomography," *Journal of medical imaging (Bellingham, Wash.)*, vol. 4, no. 1, 2017, ISSN: 2329-4310.

[35] S. Dorbala *et al.*, "Single Photon Emission Computed Tomography (SPECT) Myocardial Perfusion Imaging Guidelines: Instrumentation, Acquisition, Processing, and Interpretation," *Journal of nuclear cardiology*, vol. 25, no. 5, pp. 1784–1846, 2018, ISSN: 1071-3581.

[36] L. E. Romans, *Computed tomography for technologists: a comprehensive text*. Wolters Kluwer Health. Lippincott Williams & Wilkins, 2011, ISBN: 978-0-7817-7751-3.

[37] *An Introduction to Practical Industrial Tomography Techniques for Non-destructive Testing (NDT)* (IAEA TECDOC 1931). Vienna: International Atomic Energy Agency (IAEA), 2020, ISBN: 978–92–0–121020–3.

[38] *Industrial Process Gamma Tomography* (TECDOC Series 1589). Vienna: INTERNATIONAL ATOMIC ENERGY AGENCY (IAEA), 2008, ISBN: 978-92-0-104508-9. [Online]. Available: https://www.iaea.org/publications/7921/industrial-process-gamma-tomography.

[39] J. Diaz, T. Kim, V. Petrov, and A. Manera, "X-ray and gamma-ray tomographic imaging of fuel relocation inside sodium fast reactor test assemblies during severe accidents," *Journal of Nuclear Materials*, vol. 543, p. 152 567, 2021, ISSN: 0022-3115. DOI: https://doi.org/10.1016/j.jnucmat.2020.152567.

[40] K.-L. D. Gottfried and G. Penn, *Radiation In Medicine: A Need For Regulatory Reform.* US: National Academies Press, 1996, ISBN: 0-309-05386-2.

[41] *Radiation Protection and Safety of Radiation Sources: International Basic Safety Standards* (General Safety Requirements GSR Part 3). Vienna: International Atomic Energy Agency (IAEA), 2014, ISBN: 978-92-0-135310-8.

[42] "Radiation safety in industrial radiography. Specific safety guide," International Atomic Energy Agency (IAEA), Austria, Tech. Rep., 2011.

[43] J. Miles, M. Mavrogordato, I. Sinclair, D. Hinton, R. Boardman, and G. Earl, "The use of computed tomography for the study of archaeological coins," *Journal of Archaeological Science: Reports*, vol. 6, pp. 35–41, 2016, ISSN: 2352-409X.

[44] S. D. Rawson, J. Maksimcuka, P. J. Withers, and S. H. Cartmell, "X-ray computed tomography in life sciences," *BMC Biology*, vol. 18, no. 1, 2020. DOI: 10.1186/s12915-020-0753-2.

[45] R. J. Rutten, R. H. Hammerschlag, F. C. M. Bettonvil, P. Sütterlin, and A. G. de Wijn, "Dot tomography of the solar atmosphere," *Astronomy & Astrophysics*, vol. 413, no. 3, pp. 1183–1189, 2004. DOI: 10.1051/0004-6361:20031548.

[46] P. Rizo, C. Robert-Coutant, V. Moulin, R. Sauze, and M. Antonakios, "Application of transmission tomography to nuclear waste management," *NDT.net*, [Online]. Available: https://www.ndt.net/article/wcndt00/papers/idn205/idn205.htm.

[47] G. Davies, N. Spyrou, I. Hutchinson, and J. Huddleston, "Applications of emission tomography in the nuclear industry," *Nuclear instruments & methods in physics research. Section A, Accelerators, spectrometers, detectors and associated equipment*, vol. 242, no. 3, pp. 615–619, 1986, ISSN: 0168-9002.

[48] D. Sim, *Radioactivity and ionizing radiation*, [Online; accessed March 10, 2023], 2014. [Online]. Available: https://commons.wikimedia.org/wiki/File:Radioactivity_and_radiation.svg.

[49] D. E. Goldberg, *Fundamentals of chemistry*, 3rd ed. Boston: McGraw-Hill Co., 2001, ISBN: 0071180753.

[50] T. Poulsen, *Introduction to Chemistry*. US: Flexbook, 2010, ISBN: 0071180753.

[51] N. J. Tro, *Introductory Chemistry*, 4th ed. US: Pearson Education, Inc., 2011, ISBN: 978-0-321-68793-7.

[52] J. Lamarsh and A. Baratta, *Introduction to Nuclear Engineering* (Addison-Wesley series in nuclear science and engineering). Prentice Hall, 2011, ISBN: 9780132764575.

[53] J. K. Shultis, *Fundamentals of nuclear science and engineering*, Third edition. Boca Raton: CRC Press, 2017, ISBN: 1498769292.

[54] R. L. Murray, *Nuclear energy an introduction to the concepts, systems, and applications of nuclear processes*, 6th ed. Amsterdam ; Butterworth-Heinemann/Elsevier, 2009, ISBN: 1-281-98212-1.

[55] H. Etherington, *Nuclear engineering handbook.* (McGraw-Hill handbooks), 1st ed. New York: McGraw-Hill, 1958.

[56] T. Jevremovic, *Nuclear principles in engineering*, 2nd ed. New York ; Springer, 2009, ISBN: 9780387856070.

[57] P. A. Tipler, *Modern physics.* 5th ed. / Paul A. Tipler, Ralph A. Llewellyn. New York, NY: W.H. Freeman, 2008, ISBN: 9780716775508.

[58] S. T. Thornton, *Modern physics for scientists and engineers*, 4th ed. Boston, MA: Cengage Learning, 2013, ISBN: 9781133103721.

[59] C. Leroy and P.-G. Rancoita, *Principles of Radiation Interaction in Matter and Detection*, 2nd. WORLD SCIENTIFIC, 2009. DOI: 10.1142/6872.

[60] *Photon Cross Sections, Attenuation Coefficients, And Energy Absorption Coefficients from 10 keV tp 100 GeV.* (National Standard Reference Data Series. US Dept. of Commerce National Bureau of Standards ; 29). 1970.

[61] L. Pires, F. Cássaro, L. Tech, L. Pereira, and J. d. Oliveira, "Gamma ray attenuation for determining soil density: Laboratory experiments for environmental physics and engineering courses," *Revista Brasileira de Ensino de Física*, vol. 42, no. Rev. Bras. Ensino Fís., 2020 42, e20190340, 2020, ISSN: 1806-1117. DOI: 10.1590/1806-9126-RBEF-2019-0340.

[62] J. E. Turner, "Interaction of ionizing radiation with matter," *Health physics (1958)*, vol. 88, no. 6, pp. 520–544, 2005, ISSN: 0017-9078.

[63] W. N. Cottingham, *An introduction to nuclear physics*, 2nd ed. Cambridge ; Cambridge University Press, 2001, ISBN: 0521651492.

[64] P. Tandon, D. Prakash, S. C. Kheruka, and N. N. Bhat, "Interaction of ionizing radiation with matter," in *Radiation Safety Guide for Nuclear Medicine Professionals*, Singapore: Springer, 2022, pp. 21–35, ISBN: 9789811945175.

[65] K. Vetter, L. Mihailescu, K Nelson, J. Valentine, and D Wright, "Gamma-ray imaging methods," Jan. 2006. DOI: 10.2172/1036848.

[66] M. Ker, "Using texture to predict diagnosis and disease from nuclear medicine lung perfusion scans: A comparison of nuclear medicine physicians to the slope of the power spectrum.," Jan. 1991.

[67] J. O'Malley and H. Ziessman, *Radiation Detection & Ancillary Instrumentation*, 5th ed. US: Elsevier, 2020, ISBN: 9780323550741.

[68] B. Zitelli, S. C. McIntire, A. Nowalk, and J. Garrison, *Fundamentals of Pediatric Radiology*, 8th ed. US: Elsevier, 2021, ISBN: 9780323777896.

[69] G. F. Knoll, *Radiation detection and measurement*, 4th ed. Hoboken, N.J: John Wiley, 2010, ISBN: 9780470131480.

[70] K. H. Czock, "Principles of radiation detection," International Atomic Energy Agency (IAEA), Austria, Tech. Rep., 1998. [Online]. Available: http://inis.iaea.org/search/search.aspx?orig_q=RN:20023330.

[71] D. Sands, *Introduction to crystallography*, Dover ed. New York: Dover Publications, Inc., 1993, ISBN: 0486678393.

[72] F. Hoffmann, *Introduction to crystallography*, 1st ed. Cham, Switzerland: Springer, 2020, ISBN: 9783030351106.

[73] J. M. Fiore, *Semiconductor Fundamentals*. New York: Creative Commons Licence, 2021, ISBN: 978-1796543537.

[74] K. T. Claxton, "Principios y tecnicas para la utilizacion de trazadores gamma," Spanish, International Atomic Energy Agency (IAEA), Spain, Tech. Rep., 1978. [Online]. Available: http://inis.iaea.org/search/search.aspx?orig_q=RN:09408312.

[75] A. Lempicki, "The physics of inorganic scintillators," *Journal of applied spectroscopy*, vol. 62, no. 4, pp. 787–802, 1995, ISSN: 0021-9037.

[76] S. R. Cherry, J. A. Sorenson, and M. E. Phelps, in *Physics in Nuclear Medicine*, S. R. Cherry, J. A. Sorenson, and M. E. Phelps, Eds., Fourth Edition, Philadelphia: W.B. Saunders, 2012, pp. 195–208, ISBN: 978-1-4160-5198-5.

[77] F. D. Mari and E. D. Vito, *Harmonic and Applied Analysis: From Radon Transforms to Machine Learning*. Switzerland: Springer International Publishing, 2021, ISBN: 978-3-030-86664-8.

[78] *Medical imaging systems : an introductory guide* (Lecture notes in computer science, 11111). Cham, Switzerland: Springer Open, 2018, ISBN: 9783319965208.

[79] S. W. Smith, *The scientist and engineer's guide to digital signal processing*, 1st ed. San Diego, Calif: California Technical Pub., 1997, ISBN: 0966017633.

[80] P. V. Chuan, N. D. Hoa, N. X. Hai, N. N. Anh, N. N. Dien, and P. D. Khang, "A scintillation detector configuration for pulse shape analysis," *Nuclear Engineering and Technology*, vol. 50, no. 8, pp. 1426–1432, 2018, ISSN: 1738-5733.

[81] M. N. Asl and A. Sadremomtaz, "Analytical image reconstruction methods in emission tomography," *Journal of Biomedical Science and Engineering*, vol. 6, no. 1, pp. 100–107, 2013. DOI: 10.4236/jbise.2013.61013.

[82] L. Yu and S. Leng, "Image reconstruction techniques," Image Wisely, Tech. Rep., Sep. 2016. [Online]. Available: https : / / www . imagewisely . org / Imaging - Modalities / Computed - Tomography / Image - Reconstruction - Techniques.

[83] *Nuclear medicine physics : a handbook for teachers and students*. Vienna: International Atomic Energy Agency (IAEA), 2014, ISBN: 9201438109.

[84] S. J. Axler, *Linear algebra done right* (Undergraduate texts in mathematics), Third edition. Springer, 2015, ISBN: 9783319110790.

[85] B. Jahne, *Digital image processing : concepts, algorithms, and scientific applications*, 4th ed. Berlin ; Springer, 1997, ISBN: 3540627243.

[86] A. C. Kak, *Principles of computerized tomographic imaging* (Classics in applied mathematics ; 33). Philadelphia, Pa: Society for Industrial and Applied Mathematics (SIAM), 2001 - 1988, ISBN: 0-89871-927-5.

[87] C. A. Mack, *Fundamental principles of optical lithography : the science of microfabrication*. Chichester, West Sussex, England ; Wiley, 2007, ISBN: 9780470018934.

[88] D. Bull and F. Zhang, *Signal processing and information theory fundamentals*. Academic Press, 2021, ISBN: 9780128203538.

[89] M. C. Jeruchim, *Simulation of communication systems : modeling, methodology, and techniques* (Information technology–transmission, processing, and storage), 2nd ed. New York: Kluwer Academic/Plenum Publishers, 2000, ISBN: 0306462672.

[90] B. Osgood, "The fourier transform and its applications," Stanford University, US, Tech. Rep., 1998.

[91] W. K. Pratt, *Digital image processing*. New York: Wiley, 1978, ISBN: 0471018880.

[92] J. W. Goodman, *Introduction to Fourier optics*, 3rd ed. Englewood, Colo: Roberts & Co., 2005, ISBN: 0974707724.

[93] J. M. Blackledge, *Digital image processing : mathematical and computational methods*. Chichester, West Sussex: Horwood Publishing, 2005, ISBN: 1898563497.

[94] G. T. GULLBERG, *The attenuated radon transform: Theory and application in medicine and biology*, eng, 1979.

[95] J. Beatty, "The radon transform and the mathematics of medical imaging," M.S. thesis, Colby Collage, Waterville, Maine, 2012. [Online]. Available: https://digitalcommons.colby.edu/honorstheses/646.

[96] I. Mazur, *Introductory algebra*. Victoria, B.C: BCcampus, BC Open Textbook Project, 2021 - 2021, ISBN: 9781774200957.

[97] G. Strang, *Calculus*. Wellesley, Mass: Wellesley-Cambridge Press, 1991, ISBN: 0961408820.

[98] *Calculus : single and multivariable*, 2nd ed. New York: Wiley, 1998, ISBN: 0471194905.

[99] J. Benjamin, "The radon transform," M.S. thesis, Harvard University, Cambridge, MA, 2020.

[100] G. B. Arfken, *Mathematical methods for physicists*. New York: Academic Press, 1966.

[101] T. G. Feeman, *The mathematics of medical imaging : a beginner's guide* (Springer undergraduate texts in mathematics and technology), Second edition. Cham: Springer International Publishing Sweden, 2015 - 2015, ISBN: 3319226649.

[102] L. A. Shepp and B. F. Logan, "The Fourier reconstruction of a head section," *IEEE Transactions on Nuclear Science*, vol. 21, no. 3, pp. 21–43, 1974, ISSN: 0018-9499.

[103] *Infrared Spectroscopy*, 3rd ed. San Diego: Academic Press, 2002, ISBN: 0122274105.

[104] J. Orrison William W., *Clinical Brain Imaging: Computerized Axial Tomography and Magnetic Resonance Imaging*. Burlington: Elsevier, 1994, ISBN: 1-4832-8444-1.

[105] M. Berger, *Problems in geometry* (Problem books in mathematics). New York: Springer-Verlag, 1984, ISBN: 0387909710.

[106] I. Hacking, "Slightly more realistic personal probability," *Philosophy of science*, vol. 34, no. 4, pp. 311–325, 1967, ISSN: 0031-8248.

[107] M. Schmidt, "Deriving the gradient and hessian of linear and quadratic functions in matrix notation," University of British Columbia, Vancouver, Tech. Rep., 2019.

[108] R. Ganatra, "Single photon emission computerized tomography (SPECT)," International Atomic Energy Agency (IAEA), Austria, Tech. Rep. 1, 1992. [Online]. Available: https://inis.iaea.org/search/search.aspx?orig_q=RN:29049601.

[109] *Radiotracer Applications in Industry* (Technical Reports Series 423). Vienna: International Atomic Energy Agency (IAEA), 2004, ISBN: 92-0-114503-9.

[110] "Radiation sources at nuclear plants," USNRC Technical Training Center, US, Tech. Rep., 2011. [Online]. Available: https://mitnse.files.wordpress.com/2011/03/radiation_npp_07.pdf.

[111] *Computational Analysis of the Behaviour of Nuclear Fuel Under Steady State, Transient and Accident Conditions* (TECDOC Series 1578). Vienna: International Atomic Energy Agency (IAEA), 2008, ISBN: 978-92-0-110507-3.

[112] S. Holcombe, "Gamma spectroscopy and gamma emission tomography for fuel performance characterization of irradiated nuclear fuel assemblies," eng, M.S. thesis, Uppsala Universitet, Uppsala, SE, 2014, ISBN: 978-91-554-9099-7.

[113] H. Kim, M. Lee, H. Choi, C. Min, and H. Choi, "Tomographic image reconstruction techniques for accurate spent fuel assembly verification," *Journal of instrumentation*, vol. 18, no. 1, pp. C01032–, 2023, ISSN: 1748-0221.

[114] M. Dietze, W. Branderhorst, B. Kunnen, M. Viergever, and H. de Jong, "Accelerated SPECT image reconstruction with FBP and an image enhancement convolutional neural network," *EJNMMI Physics*, vol. 6, no. 1, pp. 14–12, 2019, ISSN: 2197-7364.

[115] T. Farncombe, "Functional dynamic SPECT imaging using a single slow camera rotation," Ph.D. dissertation, University of British Columbia, 2000. DOI: http://dx.doi.org/10.14288/1.0085703.

[116] J. Sheng, Y. Ma, W. Liu, and Q. Liu, "Hybrid cardiac imaging integrating elliptical orbit SPECT with CT," *IEEE Access*, vol. PP, pp. 1–1, Dec. 2019. DOI: 10.1109/ACCESS.2019.2960387.

[117] R. J. Estep, T. Prettyman, and G. Sheppard, "Tomographic Gamma Scanning (TGS) to Measure Inhomogenous Nuclear Material Matrices from Future Fuel Cycles," *Future Nuclear Systems: Emerging Fuel Cycles and Waste Disposal Options*, 1993.

[118] J. S. Hansen, "Application guide to tomographic gamma scanning of uranium and plutonium," Safeguards Science and Technology Nuclear Nonproliferation Division Los Alamos Laboratory, New Mexico, Tech. Rep.

[119] X. Mu, R. Shi, G. Luo, and X. Tuo, "A collimator design method for the tomographic gamma scanning system with a fan-shaped NaI(Tl) detector array," *Applied radiation and isotopes*, vol. 182, pp. 110 123–110 123, 2022, ISSN: 0969-8043.

[120] H. Zheng *et al.*, "An improved algebraic reconstruction technique for reconstructing tomographic gamma scanning image," *Nuclear instruments & methods in physics research. Section A, Accelerators, spectrometers, detectors and associated equipment*, vol. 906, pp. 77–82, 2018, ISSN: 0168-9002.

[121] C.-M. Wang *et al.*, "Reconstruction of tomographic gamma scanning transmission image from sparse projections based on convolutional neural networks," *Nuclear instruments & methods in physics research. Section A, Accelerators, spectrometers, detectors and associated equipment*, vol. 1039, pp. 167 110–, 2022, ISSN: 0168-9002.

[122] M. I. Haraguchi, W. A. P. Calvo, and H. Y. Kim, "Tomographic 2-D gamma scanning for industrial process troubleshooting," *Flow measurement and instrumentation*, vol. 62, pp. 235–245, 2018, ISSN: 0955-5986.

[123] K. D. Atkinson and L. Grana, "Development of a limited angle gamma ray emission tomography system for in-situ spatially-resolved measurement of fuel burn up and pre-shutdown power.," *Transactions of the American Nuclear Society*, vol. 118, 2018.

[124] J. A. Adams, "X-ray laminography analysis of ultra-fine-pitch solder connections on ultrathin boards," in *Proceedings of SPIE*, vol. 1464, SPIE, 1991, pp. 484–497, ISBN: 0819405639.

[125] N. S. O'Brien, R. P. Boardman, I. Sinclair, and T. Blumensath, "Recent advances in x-ray cone-beam computed laminography," eng, *Journal of X-ray science and technology*, vol. 24, no. 5, pp. 691–707, 2016, ISSN: 0895-3996.

[126] Y. Zhao, J. Xu, H. Li, and P. Zhang, "Edge information diffusion-based reconstruction for cone beam computed laminography," *IEEE transactions on image processing*, vol. 27, no. 9, pp. 4663–4675, 2018, ISSN: 1057-7149.

[127] S. V. Venkatakrishnan, E. Cakmak, H. Billheux, P. Bingham, and R. K. Archibald, "Model-based iterative reconstruction for neutron laminography," in *2017 51st Asilomar Conference on Signals, Systems, and Computers*, IEEE, 2017, pp. 1864–1869, ISBN: 9781538606667.

[128] S. Gondrom, S. Schropfer, F. ITFP, and D. Saarbrucken, "Digital computed laminography and tomosynthesis - functional principles and industrial applications," eng, *International Symposium on Computerized Tomography for Industrial Applications and Image Processing in Radiology*, vol. 4, no. 7, 1999. [Online]. Available: https://www.ndt.net/article/v04n07/bb67_11/bb67_11.htm.

[129] Y. Haik, *Engineering design process*, 2nd ed. Stamford, CT: Cengage Learning, 2011, ISBN: 9780495668145.

[130] R. Aris, *Mathematical modelling techniques*. New York: Dover Publications, 1994 - 1978, ISBN: 9780486681313.

[131] J. Stewart, *Calculus : early transcendentals*, 7th ed., alternate ed. Belmont, CA: Brooks/Cole, Cengage Learning, 2012, ISBN: 9780840058454.

[132] R. G. Brown, *Introductory Physics I. Elementary Mechanics*. Durham, NC, 2013. [Online]. Available: http://www.phy.duke.edu/âĹijrgb/Class/introphysics1.php.

[133] nagwa editors, *Lesson Explainer: Polar Form of a Vector*. [Online]. Available: https://www.nagwa.com/en/explainers/819141496492/ (visited on 04/01/2023).

[134] M. Berger, *Geometry* (Universitext). Berlin: Springer-Verlag, 1987, ISBN: 0387116583.

[135] S. F. Andrilli, *Elementary linear algebra*, 4th ed. Amsterdam ; Elsevier Academic Press, 2010, ISBN: 9780123747518.

[136] D. W. Baker and W. Haynes, *Engineering Statics. Open and Interactive*, 1st ed. United States: Creative Commons Attribution-Non Commercial-Share Alike 4.0 International Licese, 2023.

[137] cuemath editors, *Rotation matrix*. [Online]. Available: https://www.cuemath.com/algebra/rotation-matrix/ (visited on 04/01/2023).

[138] D. Rose, *Rotations in three-dimensions: Euler angles and rotation matrices*. [Online]. Available: https://danceswithcode.net/engineeringnotes/rotations_in_3d/rotations_in_3d_part1.html (visited on 04/01/2023).

[139] K. F. K. F. Riley, *Mathematical methods for physics and engineering*, 3rd ed. Cambridge: Cambridge University Press, 2006, ISBN: 0521861535.

[140] N. Altshiller-Court, *College geometry. An introduction to the modern geometry of the triangle and the circle* (College outline series ; no. 54), 2d ed., rev. asnd enl.–. New York: Barnes & Noble, 1952.

[141] Geant4 Collaboration, "Introduction to Geant4. Release 11.0," European Organization for Nuclear Research (CERN), Geneva, Tech. Rep., 2021.

[142] K. Martin and B. Hoffman, *Mastering CMake*. [Online]. Available: `https://cmake.org/cmake/help/book/mastering-cmake/` (visited on 04/11/2023).

[143] Microsoft Corporation, *Welcome to Visual Studio*. [Online]. Available: `https : / / learn . microsoft . com / en - us / visualstudio / get - started/visual-studio-ide?view=vs-2019` (visited on 04/11/2023).

[144] Geant4 Collaboration, "Geant4 Installation Guide Documentation. Release 11.0," European Organization for Nuclear Research (CERN), Geneva, Tech. Rep., 2021.

[145] J. Kessenich, *OpenGL Programming Guide: The Official Guide to Learning OpenGL, Version 4.5 with SPIR-V, Ninth Edition*, 9th edition. Addison-Wesley Professional, 2016, ISBN: 9780134495491.

[146] CPLUSPLUS, *Headers and includes: Why and how*, 2009. [Online]. Available: `https : / / cplusplus . com / articles / Gw6AC542/` (visited on 04/11/2023).

[147] "Physical Design. Design of Reactor Facilities," Canadian Nuclear Safety Commission (CNSC), Ottawa, Tech. Rep., 2023.

[148] G. Malkoske, J. Norton, and J. Slack, *Cobalt-60 production in CANDU power reactors*, Canada, 2002.

[149] "The use and management of sealed radioactive sources," International Atomic Energy Agency (IAEA), Vienna, Tech. Rep. [Online]. Available: `https : / / www . iaea . org / sites / default / files / gc / gc56inf - 3 - att6_en.pdf`.

[150] *Radiation doses*, Canada, 2023. [Online]. Available: `http : //nuclearsafety.gc.ca/eng/resources/radiation/introduction-to-radiation/radiation-doses.cfm`.

[151] "NaI(Tl) and Polyscin NaI(Tl) Sodium Iodide Scintillation Material," Saint-Gobain, France, Tech. Rep., 2021. [Online]. Available: `https : / / www . crystals . saint - gobain . com / sites / hps - mac3 - cma - crystals/files/2021-08/Sodium-Iodide-Material-Data-Sheet.pdf`.

[152] G. G. Thoreson, D. J. Mitchell, C. A. Brusseau, L. T. Harding, and L. H. Arakaki, "Design and characterization of a sodium iodide (NaI) array for coincidence measurements," US, Tech. Rep. SAND2012-9348, 2012. [Online]. Available: https://www.osti.gov/servlets/purl/1055886.

[153] *Tutorial of SCIONIX scintillation detectors*, Netherlands, 2018. [Online]. Available: https://scionix.nl/wp-content/uploads/2022/07/Tutorial-of-SCIONIX-scintillation-detectors-2018-3-_compressed.pdf.

[154] P. L. Reeder and D. C. Stromswold, "Performance of large NaI(Tl) gamma ray detectors over temperature -50 degrees C to +60 degrees C," Washington, Tech. Rep., 2004. [Online]. Available: https://digital.library.unt.edu/ark:/67531/metadc1405293/.

[155] J. Nilsson, V. Cuplov, and M. Isaksson, "Identifying key surface parameters for optical photon transport in geant4/gate simulations," *Applied Radiation and Isotopes*, vol. 103, pp. 15–24, 2015, ISSN: 0969-8043. DOI: https://doi.org/10.1016/j.apradiso.2015.04.017. [Online]. Available: https://www.sciencedirect.com/science/article/pii/S096980431530018X.

[156] Geant4 Collaboration, "Book For Application Developers. Release 11.1," European Organization for Nuclear Research (CERN), Geneva, Tech. Rep., 2022.

[157] *Handbook of radioactivity analysis*, 2nd ed. San Diego: Academic Press, 2003, ISBN: 0124366031.

[158] "Photomultiplier tubes catalogue," PHOTONIS, France, Tech. Rep., 2007. [Online]. Available: https://hallcweb.jlab.org/DocDB/0008/000809/001/PhotonisCatalog.pdf.

[159] P. Gonçalves, *Sensitive detectors*, Braga, 2013. [Online]. Available: https://indico.lip.pt/event/681/contributions/2103/attachments/1907/2542/Geant4_SD.pdf.

[160] R. J. Wilson, "Collimator technology and advancements," *Journal of Nuclear Medicine Technology*, vol. 16, no. 4, pp. 198–203, 1988, ISSN: 0091-4916.

[161] F. A. Mettler, *Essentials of nuclear medicine imaging*, eng, 6th ed. Philadelphia, PA: Elsevier/Saunders, 2012, ISBN: 9781455701049.

[162] S. H. Razavi *et al.*, "Characterization of low, medium and high energy collimators for common isotopes in nuclear medicine: A monte carlo study," *Majallahi-i pizishk-i hastahi Īran*, vol. 25, no. 2, pp. 100–, 2017, ISSN: 1681-2824.

[163] H. Pishro-Nik, *Introduction to probability, statistics, and random processes*. Blue Bell, PA: Kappa Research, LLC, 2014, ISBN: 9780990637202.

Appendix A

One-Dimension Signal Processing

Let us define a continuous function in one-dimension (1D) of the form $x(t)$ and dependent on the variable t. Its discrete representation is given by a sample of a specific range of points, or a vector, in an n-dimensional space. For example, $\cdots$, $x(-\tau)$, $x(0)$, $x(\tau)$, $x(2\tau)$, $\cdots$, $x(n\tau)$, $\cdots$ where τ can represent a single value or a set (see Figure A.1).
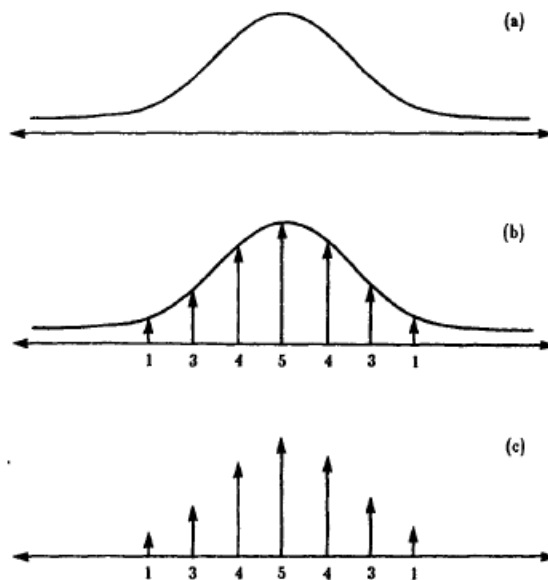
FIGURE A.1: Representation of a function, or signal, being sampled and its discrete values. In this case, (a) is the graph of the function $x(t)$, (b) the sampling of the function, and (c) the respective discrete values given by 1, 3, 4, 5, 4, 3, 1 [86].

In the signal processing of data, operations with functions are necessary for filtering, smoothing, modulate amplitudes, etc. Therefore, mathematical techniques or functions that will simplify these operations are commonly used; for instance, the Dirac delta (or impulse function). The Dirac delta $\delta(x)$ is not a function by itself but a property used to delimit a distribution or sequence of functions [100]. The characteristic of this generalization is that the function is zero everywhere except at zero, and has a height equal to one over all the real numbers. To better understand this distribution, let us define the following function, see Figure A.2 for its representation on a plane

$$\text{rect}(t) = \begin{cases} 0, & \text{elsewhere} \\ 1, & \|t\| < \frac{1}{2} \end{cases} \tag{A.1}$$
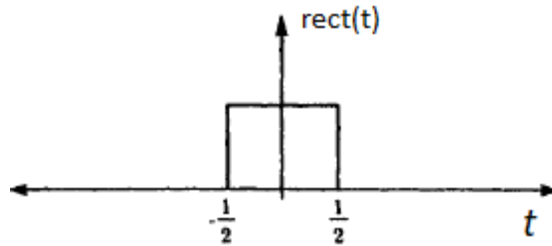
FIGURE A.2: Graph of the function rect(t) [86].

If we scale this function and pile it in width and height, it will be easier to notice that the distribution function is always decreasing for t and it can be described by

$$\delta_n(t) = n \, \text{rect}(nt), \tag{A.2}$$

since the function is always increasing in its height $n \to \infty$. Thus, the width of the function is zero but its height is infinite with a unitary area. This is a property of the Dirac delta and is represented by a line or arrow of length one, as seen in Figure A.3, and mathematically defined with Equation A.3.

$$\int_{-\infty}^{\infty} \delta(t) \, dx = 1 \tag{A.3}$$
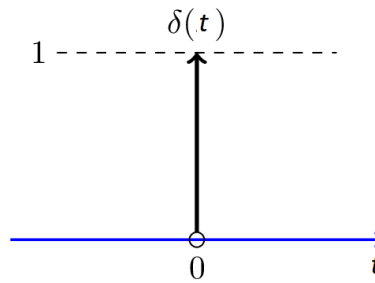
FIGURE A.3: Dirac delta $\delta(t)$ [163].

Therefore, it can be inferred that the delta function is useful to model or sample a peak function or impulse, so it is said that it has a "sampling" property where the change or shift of location $t = t'$ is given by $\delta(t - t')$, and represented on Figure A.4. If the impulse enters with an arbitrary $x(t)$, only those values inside of $t = t'$ are considered [86]; thus, $\delta(t - t')$ samples the function $x(t)$ at t' and has an integral form of

$$\int_{-\infty}^{\infty} x(t)\delta(t - t') \, dx = x(t') \tag{A.4}$$
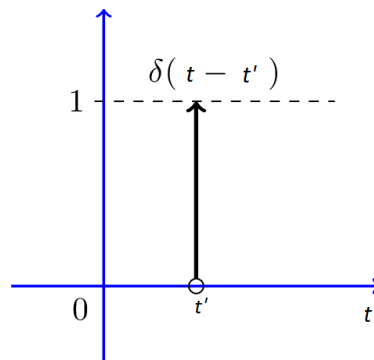
FIGURE A.4: Shifted Dirac delta $\delta(t - t')$ [163].

As mentioned, linear operations are necessary for data manipulation. Thus, let us define a function operator O and apply it to the function $x(t)$, which is presented by $O[x(t)]$. If an operator takes one or more functions as an entry, it will return a function like the following

$$O[\alpha x(t) + \beta y(t)] = \alpha O[x(t)] + \beta O[y(t)] \tag{A.5}$$

where α and β are constants, and $x(t)$ and $y(t)$ are functions.

Let us define the linear operation class in its integral form as

$$y(t) = \int_{-\infty}^{\infty} x(t')h(t,t')\,dt' \tag{A.6}$$

where h is the impulse response of the operator applied to the delta function [86]. If we define the input $x(t)$ as an impulse $t = t_0$, then $x(t) = \delta(t - t_0)$. And, introducing this in Equation A.6, we will obtain

$$
\begin{aligned}
y(t) &= \int_{-\infty}^{\infty} \delta(t' - t_0)h(t,t')\,dt' \\
&= h(t,t_0)
\end{aligned}
\tag{A.7}
$$

where $h(t,t')$ is the impulse response for the shift applied at t'. Moreover, the impulse is said to be invariant if $y(t) = O[x(t)]$ and $y(t - \tau) = O[x(t - \tau)]$ with $h(t,t') = h(t - t')$. Meaning that if the impulse is changed to t', its output will change too, so the output function of a linear operation does not change with an impulse shift since the change is the same. Therefore, Equation A.6 becomes

$$y(t) = \int_{-\infty}^{\infty} x(t')h(t - t')\,dt' \tag{A.8}$$

which is called convolution, and is represented with Figure A.5 and denoted by the following equation

$$z(t) = x(t) * h(t) \tag{A.9}$$
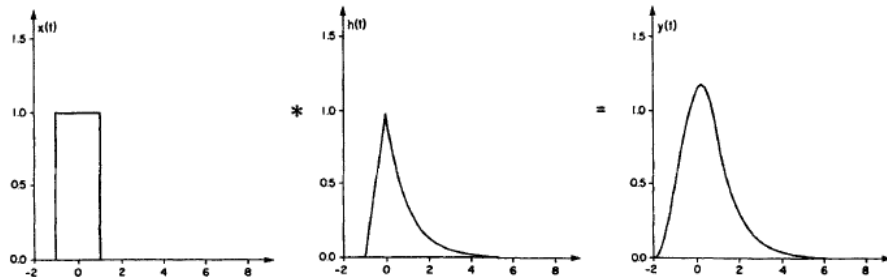
FIGURE A.5: Convolution process on a square impulse $x(t)$ applied to an impulse response $h(t)$; $y(t)$ is the convolved function [86].

Fourier Series and Transform			
		Continuous Time	Discrete Time
Cont. Freq.	Name	Fourier Transform	Discrete Fourier Transform
	Forward	$F(\omega) = \int_{-\infty}^{\infty} f(t)e^{-i\omega t}\, dt$	$F(\omega) = \sum_{n=-\infty}^{\infty} f(n\tau)e^{-i\omega n\tau}$
	Inverse	$f(t) = \frac{1}{2\pi}\int_{-\infty}^{\infty} F(\omega)e^{i\omega t}\, d\omega$	$f(n\tau) = \frac{\tau}{2\pi}\int_{-\pi/\tau}^{\pi/\tau} F(\omega)e^{i\omega n\tau}\, d\omega$
	Period	None	$F(\omega) = F[\omega + j(2\pi/\tau)]$
Disc. Freq.	Name	Fourier Series	Finite Fourier Transform
	Forward	$F_n = \frac{1}{T}\int_0^T f(t)e^{-in(2\pi/T)t}\, dt$	$F_k = \frac{1}{N}\sum_{n=0}^{N} f_n e^{-i(2\pi/N)kn}$
	Inverse	$f(t) = \sum_{n=-\infty}^{\infty} F_n e^{in(2\pi/T)t}$	$f_k = \sum_{n=0}^{N} F_n e^{i(2\pi/N)kn}$ $f_k =$
	Period	$f(t) = f(t+jT)$	f_{k+jN} and $F_k = F_{k+jN}$

TABLE A.1: Overview of Fourier Series and Transforms with their respective name, formulations for forward and inverse cases, and their periodicity. In this table, the notation f is for functions of time while F is for frequency [86][90].

This process of combining two signals to form a third one can be described in discrete terms by defining the functions $x_i = x(i\tau)$ and $y_i = y(i\tau)$, and the convolution applied to x_i will be expressed in terms of y_i

$$y_i = \tau \sum_{j=-\infty}^{\infty} x_j h_{i-j} \tag{A.10}$$

where τ takes values of the real numbers.

Another method used to represent signals is Fourier transforms, which represent these pulses as a function of frequency. This representation brings variety to a different perspective of the problem analysis along with simpler expressions for some function processes like convolution. For simplification of this section, a table (see Table A.1) summarizing the principal Fourier equations for each case is provided and explained.

Fourier series are used to analyze and represent periodic signals where they can be extended to non-periodic conditions with the Fourier transforms. In this case, the discrete periodic group of functions becomes continuous in the non-periodic group [90]. Let us assume that a continuous function $f(t)$ is defined in a time

interval of $T_1 \leq t \leq T_2$ and can be expressed as an addition of a n number of functions, see the Fourier Series section on Table A.1. In these equations, $i = \sqrt{-1}$ is the imaginary unit and $2\pi/T = 2\pi f_0 = \omega_0$ is the fundamental angular frequency with a fundamental frequency f_0 and $T = T_2 - T_1$, F_n are complex coefficients of the n-th component that can be obtained with the forward Fourier Series, and the complex exponential represents a curve or wave in the form of a sine function with oscillations of nf_0 cycles per unit of t [86], which is represented by

$$e^{in(2\pi/T)t} = \cos n(2\pi/T)t + i\sin n(2\pi/T)t \tag{A.11}$$

However, if the $f(t)$ function is now defined in an interval between $-\infty$ to ∞, then the Fourier equations are continuous and called Fourier Transform $F(\omega)$, defined in the frequency domain. In this case, the frequencies are multiples of ω_0 or $\omega = n\omega_0 = n(2\pi/T)$ where ω_0 can take any real number as a value.

Moreover, for discrete functions $f(n\tau)$ represents samples of $f(t)$, and $F(\omega)$ is the sampled data in the frequency domain, see Table A.1. Here, $F(\omega)$ is the Discrete Fourier Transform (DFT) of $f(n\tau)$ and represents the amplitude of the sine function for discrete signals [100].

As seen in Dirac's delta function, the convolution (i.e., the combination of two functions that produces a third one) can be defined with Equation A.10. But, if we defined the functions $x_k = x(k\tau)$ and $h_k = h(k\tau)$, the convolution will be given by

$$y_k = \sum_{j=-\infty}^{\infty} x_j h_{k-j} \tag{A.12}$$

and can be expressed in terms of the Fourier Transform as

$$Y(\omega) = X(\omega)H(\omega) \tag{A.13}$$

Notice the similitude of the functions presented in the Discrete Fourier Transform section on Table A.1; the derivation of the convolution equation with Fourier Transforms is omitted in this paper.

Therefore, if we take τ interval samples of the continuous function then the discrete functions x_n and y_n will result in a function z_n [90], this is

$$z_n = x_n y_n \tag{A.14}$$

and the convolution in the angular frequency domain will be

$$Z(\omega) = \frac{\tau}{2\pi} \int_{-\pi/\tau}^{\pi/\tau} X(\alpha) Y(\omega - \alpha) \, d\alpha \tag{A.15}$$

Finally, for the Finite Fourier Transforms (FFT), let us consider the discrete function set $f(0)$, $f(\tau)$, $f(2\tau)$, $\cdots$, $f((N-1)\tau)$ with N elements, which can be transcribed to the form f_0, f_1, f_2, $\cdots$, f_{N-1}. Therefore, the FFT F_k for $k = 0, 1, 2, \cdots, N-1$ is the sample or samples of the continuous frequency function $F(\omega)$ that is defined with $\omega = k\frac{1}{N\tau}$; this implies that the interval of τ in the time domain sample is a sample interval of $1/N_\tau$ in the domain of frequency [86].

Because it is said that the finite Fourier transform is periodically repeated, let us analyze the inverse function for the FFT for a case where $k = Nm + j$ and $e^{i(2\pi/N)Nm} = 1$ for all m integers, so

$$F_{Nm+j} = F_j \tag{A.16}$$

for the forward and inverse functions. In the same form that convolution was defined for discrete transforms, it can be done for FFT which is commonly called circulation convolution [89]. Let us consider the following operation for finite transforms

$$Z_k = X_k Y_k \tag{A.17}$$

that have the form of the forward FFT, and results in the following function

$$z_n = \frac{1}{N} \sum_{k=0}^{N-1} x_{n-k} y_k \tag{A.18}$$

having a similar form to Equation A.10. For the case when $n = 0$, the first member of the addition will be $x_0 y_0$ and the second one $x_{-1} y_1$, but using the form

of Equation A.16, the terms are between 0 and $N-1$. This implies that $x_{-1} = x_{N-1}$ and leads to a cyclic convolution since terms from the original FFT function are substituted by a cyclic replica of the original data [86]; thus, circular convolution is the convolution of two periodic functions of equal length that will lead to a third function of the same period.

Appendix B

Computational Code

B.1 Header Files

```
// **********************************************************************
// * License and Disclaimer                                           *
// *                                                                  *
// * The  Geant4 software  is  copyright of the Copyright Holders  of *
// * the Geant4 Collaboration.  It is provided  under  the terms  and *
// * conditions of the Geant4 Software License,  included in the file *
// * LICENSE and available at  http://cern.ch/geant4/license .  These *
// * include a list of copyright holders.                             *
// *                                                                  *
// * Neither the authors of this software system, nor their employing *
// * institutes,nor the agencies providing financial support for this *
// * work  make  any representation or  warranty, express or implied, *
// * regarding  this  software system or assume any liability for its *
// * use.  Please see the license in the file  LICENSE  and URL above *
// * for the full disclaimer and the limitation of liability.         *
// *                                                                  *
// * This  code  implementation is the result of  the  scientific and *
// * technical work of the GEANT4 collaboration.                      *
// * By using,  copying,  modifying or  distributing the software (or *
// * any work based  on the software)  you  agree  to acknowledge its *
// * use  in  resulting  scientific  publications,  and indicate your *
// * acceptance of all terms of the Geant4 Software license.          *
```

```cpp
// **********************************************************************
//To avoid file repetition
    #ifndef SYSTEM2CONSTRUCTION_H
    #define SYSTEM2CONSTRUCTION_H

//Packages to create figures
    #include "G4SystemOfUnits.hh"
    #include "G4PhysicalConstants.hh"
    #include "G4VUserDetectorConstruction.hh"
    #include "G4VPhysicalVolume.hh"
    #include "G4LogicalVolume.hh"
    #include "G4Box.hh"
    #include "G4Tubs.hh"
    #include "G4PVPlacement.hh"
    #include "G4NistManager.hh"

//Construction of class designed : embedded or inherited to Geant4 class
    class MySystem2Construction :public G4VUserDetectorConstruction
    {
    public:
      MySystem2Construction(); //Construct class
      ~MySystem2Construction(); //Destruct class

//Constructs all geometry and returns a value
    G4LogicalVolume* GetScoringVolume() const {return fScoringVolume;}

     virtual G4VPhysicalVolume* Construct();

    private:
      G4LogicalVolume* encapLOG;

      virtual void ConstructSDandField();
      G4OpticalSurface* mirrorSurface;
```

```
    G4LogicalVolume* fScoringVolume;
};
#endif
```

LISTING B.1: System2Construction.h

```
#ifndef PHYSICS_H
#define PHYSICS_H

#include "G4VModularPhysicsList.hh" //Particles and processes
#include "G4EmStandardPhysics.hh" //Default electromanetic physics
#include "G4OpticalPhysics.hh" //Process: Absorption, Scattering
#include "G4DecayPhysics.hh" //Decay Processes
#include "G4RadioactiveDecayPhysics.hh" //Transitions: alpa, beta

class MyPhysics : public G4VModularPhysicsList
{
public:
    MyPhysics();
    ~MyPhysics();
};

#endif
```

LISTING B.2: Physics.h

```
#ifndef GENERATOR_H
#define GENERATOR_H

#include "G4VUserPrimaryGeneratorAction.hh"
#include "G4GeneralParticleSource.hh"
#include "G4SystemOfUnits.hh"
#include "G4ParticleTable.hh"
```

```cpp
#include "G4Geantino.hh"
#include "G4IonTable.hh"


class MyPrimaryGenerator : public G4VUserPrimaryGeneratorAction
{
public:
    MyPrimaryGenerator();
    ~MyPrimaryGenerator();

    virtual void GeneratePrimaries(G4Event*);


private:
        G4GeneralParticleSource* particleSource;
};


#endif
```

LISTING B.3: Generator.h

```cpp
#ifndef SENSITIVEDETECTOR_H
#define SENSITIVEDETECTOR_H

#include "G4VSensitiveDetector.hh"
#include "G4RunManager.hh"
#include "G4AnalysisManager.hh"
#include "globals.hh"

class MySensitiveDetector : public G4VSensitiveDetector
{
public:
  MySensitiveDetector(G4String);
  ~MySensitiveDetector();

private:
```

```cpp
    virtual G4bool ProcessHits(G4Step*, G4TouchableHistory*);
};


#endif
```

LISTING B.4: SensitiveDetector.h

```cpp
#ifndef STEPPING_H
#define STEPPING_H

#include "G4UserSteppingAction.hh"
#include "G4RunManager.hh"
#include "G4Step.hh"

#include "System2Construction.h"
#include "Event.h"

class MySteppingAction :public G4UserSteppingAction
{
public:
    MySteppingAction(MyEventAction* eventAction);
    ~MySteppingAction();

//Function with all the required commands to store data
    virtual void UserSteppingAction(const G4Step*);
//Add energy deposition to variable created
private:
    MyEventAction* fEventAction;
};

#endif
```

LISTING B.5: Stepping.h

```cpp
    #ifndef EVENT_H
    #define EVENT_H

    #include "G4UserEventAction.hh"
    #include "G4Event.hh"
    #include "G4AnalysisManager.hh" //Package to store information
    #include "Run.h"

    class MyEventAction : public G4UserEventAction
    {
    public:
        MyEventAction(MyRunAction*);
        ~MyEventAction();

//Defining stages of the event
        virtual void BeginOfEventAction(const G4Event*);
        virtual void EndOfEventAction(const G4Event*);

//Connection between event and stepping
        void AddEdep(G4double edep) { fEdep += edep; }
    private:
//Accumulation of energy
        G4double fEdep;
    };

    #endif
```

LISTING B.6: Event.h

```cpp
    #ifndef TRACKING_H
    #define TRACKING_H

    #include "G4UserTrackingAction.hh"
```

```cpp
#include "globals.hh"


class MyTracking : public G4UserTrackingAction
{
public:
    MyTracking();
    ~MyTracking() { };
    virtual void  PreUserTrackingAction(const G4Track*);
};


#endif
```

LISTING B.7: Tracking.h

```cpp
#ifndef RUN_H
#define RUN_H


#include "G4UserRunAction.hh"
#include "G4AnalysisManager.hh"
#include "G4Run.hh"
#include "globals.hh"


class MyRunAction : public G4UserRunAction
{
public:
    MyRunAction();
    ~MyRunAction();
    virtual void BeginOfRunAction(const G4Run*);
    virtual void EndOfRunAction(const G4Run*);
};
#endif
```

LISTING B.8: Run.h

```
    #ifndef ACTION_H
    #define ACTION_H

    #include "G4VUserActionInitialization.hh"

    #include "Generator.h"
    #include "Run.h"
    #include "Event.h"
    #include "Stepping.h"

//Initiation of class and build
    class MyActionInitialization : public G4VUserActionInitialization
    {
    public:
        MyActionInitialization();
        ~MyActionInitialization();

        virtual void Build() const;
    };

    #endif
```

LISTING B.9: Action.h

B.2 Source Files

```
// *********************************************************************
// * License and Disclaimer                                          *
// *                                                                  *
// * The  Geant4 software  is  copyright of the Copyright Holders  of *
// * the Geant4 Collaboration.  It is provided  under  the terms  and *
// * conditions of the Geant4 Software License,  included in the file *
```

```cpp
// * LICENSE and available at  http://cern.ch/geant4/license .  These *
// * include a list of copyright holders.                            *
// *                                                                 *
// * Neither the authors of this software system, nor their employing *
// * institutes,nor the agencies providing financial support for this *
// * work  make  any representation or  warranty, express or implied, *
// * regarding  this  software system or assume any liability for its *
// * use.  Please see the license in the file  LICENSE  and URL above *
// * for the full disclaimer and the limitation of liability.        *
// *                                                                 *
// * This  code  implementation is the result of  the  scientific and *
// * technical work of the GEANT4 collaboration.                     *
// * By using,  copying,  modifying or  distributing the software (or *
// * any work based  on the software)  you  agree  to acknowledge its *
// * use  in  resulting  scientific  publications,  and indicate your *
// * acceptance of all terms of the Geant4 Software license.         *
// *********************************************************************
//
    #include "System2Construction.h" //Defined constructed class

    #include "G4VPhysicalVolume.hh" //Figure construction
    #include "G4NistManager.hh" //Materials on data-base
    #include "G4Material.hh" //Definition of materials
    #include "G4SystemOfUnits.hh" //Units definition (e.g., meters)
    #include "G4PhysicalConstants.hh" //Constants used in physics
    #include "G4Box.hh" //Package of box shapes
    #include "G4LogicalVolume.hh" //Placement of object solid and material
    #include "G4PVPlacement.hh" //Placement of object in the main volume
    #include "G4Tubs.hh" //Package of cylindrical shapes
    #include "G4VSolid.hh" //Package for general solid properties
    #include "G4VisAttributes.hh" //Attributes (e.g., color) of solids
    #include "G4Orb.hh" //Package of spherical shapes
    #include "G4BooleanSolid.hh" //Package to force "drawing styles"
    #include "G4UnionSolid.hh" //Package to form or unit shapes
```

```cpp
   #include "G4SubtractionSolid.hh" //Package to remove shapes
   #include "G4Transform3D.hh" //Rotation matrices
   #include "G4LogicalSkinSurface.hh" //Package for skin surface
   #include "G4OpticalSurface.hh" //Optical surface properties


   MySystem2Construction::MySystem2Construction()
   {}


   MySystem2Construction::~MySystem2Construction()
   {}


   G4VPhysicalVolume* MySystem2Construction::Construct()
   {
//Materials and Properties

      G4double density, ncomponents, fracMass;

      G4double energy[2] = {2.0*eV,4.0*eV};
      G4double rindexScin[2] = { 1.85,1.85 }; //Scint refractive index
      G4double reflectivity[2] = {1.0,1.0}; //All photons are reflected
      G4double windowref[2] = {0.92,0.92}; //Aluminium reflectivity
        G4double fraction[2] = { 1.0,1.0 };


   //Materials
      G4NistManager* nist1 = G4NistManager::Instance();
      G4Material* mat = nist1->FindOrBuildMaterial("G4_AIR");
      G4Material* Al = nist1->FindOrBuildMaterial("G4_Al");
      G4Material* tugs = nist1->FindOrBuildMaterial("G4_W");
      G4Material* NaI = nist1->FindOrBuildMaterial("G4_SODIUM_IODIDE");
      G4Material* Tl = nist1->FindOrBuildMaterial("G4_Tl");
      G4Material* Si = nist1->FindOrBuildMaterial("G4_Si");
      G4Material* Mn = nist1->FindOrBuildMaterial("G4_Mn");
      G4Material* Cr = nist1->FindOrBuildMaterial("G4_Cr");
      G4Material* Ni = nist1->FindOrBuildMaterial("G4_Ni");
```

```cpp
    G4Material* Fe = nist1->FindOrBuildMaterial("G4_Fe");


      //NaI(Tl)
    G4Material* Scin = new G4Material("Scin", density = 3.67 * g / cm3,
      ncomponents = 2);
    Scin->AddMaterial(NaI, fracMass = 99.8 * perCent);
    Scin->AddMaterial(Tl, fracMass = 0.2 * perCent);


      //Stainless steel
    G4Material* stainsteel = new G4Material("StainlessSteel",
      density = 8.02 * g / cm3, ncomponents = 5);
    stainsteel->AddMaterial(Mn, 0.02);
    stainsteel->AddMaterial(Si, 0.01);
    stainsteel->AddMaterial(Cr, 0.19);
    stainsteel->AddMaterial(Ni, 0.10);
    stainsteel->AddMaterial(Fe, 0.68);


  //Properties
    G4MaterialPropertiesTable* mptScint = new G4MaterialPropertiesTable();


    //Scintillator
    mptScint->AddProperty("RINDEX", energy, rindexScin,2,true,true);
    mptScint->AddProperty("FASTCOMPONENT",energy, fraction,2,true,true);
    mptScint->AddConstProperty("SCINTILLATIONYIELD", 38./keV,true);
    mptScint->AddConstProperty("RESOLUTIONSCALE",1.0,true);
    mptScint->AddConstProperty("FASTTIMECONSTANT", 250.*ns,true);
    mptScint->AddConstProperty("YIELDRATIO", 1.0,true);
    Scin->SetMaterialPropertiesTable(mptScint);


    //Reflective coating
    mirrorSurface = new G4OpticalSurface("mirrorSurface");
    mirrorSurface->SetType(dielectric_metal);
    mirrorSurface->SetFinish(ground);
    mirrorSurface->SetModel(unified);
```

```cpp
    G4MaterialPropertiesTable* mptMirror = new G4MaterialPropertiesTable();
    mptMirror->AddProperty("REFLECTIVITY", energy, reflectivity,
      2,true,true);
    mirrorSurface->SetMaterialPropertiesTable(mptMirror);


    //Entrance window
    G4MaterialPropertiesTable* mptWindow = new G4MaterialPropertiesTable();
    mptWindow->AddProperty("REFLECTIVITY", energy, windowref,
      2, true, true);
    Al->SetMaterialPropertiesTable(mptWindow);



//Construction
  //World
  G4double world_x = 1.5 * m;
  G4double world_y = 1.5 * m;
  G4double world_z = 1.5 * m;

  G4Box* solidWorld = new G4Box("solidWorld", world_x,
    world_y, world_z);
  G4LogicalVolume* logicWorld = new G4LogicalVolume(solidWorld,
    mat, "logicWorld");
  G4VPhysicalVolume* physWorld = new G4PVPlacement(0, //no rotation
    G4ThreeVector(), //at (0,0,0)
    logicWorld, //logical volume
    "physWorld", //name
    0, //mother volume
    false, //no boolean operation
    0, //copy number
    true); //checking overlaps

  //Gamma Camera
  G4double startAngle = 0. * deg;
```

```
      G4double spanningAngle = 360. * deg;
      G4double allWidth = 10 * cm;
      G4double allHeight = 15 * cm;
      G4double allDepth = 20.5 * cm;
      G4double raPmt = 4.45*cm;
      G4double lenPmt = 12.5*cm;
      G4double lenWindow = 0.1 * cm;
      G4double lenColm = 0.5*cm;
      G4double lenSincas = 33.26 * cm;
      G4double widthSincas = 2.55*cm;
      G4double heightSincas = 5.05*cm;


      //Single Dectector
      //G4VSolid* sensdet = new G4Box("sensdetSolid", allWidth/4,
        //allHeight/3, allDepth+lenPmt+lenWindow+lenColm); //single PMT
      //G4LogicalVolume*sensdetLOG = new G4LogicalVolume(sensdet,
        //mat, "sensdetLogic");


      //G4VSolid* encap = new G4Box("encapSolid", allWidth/4,
        //allHeight/3, allDepth); //single scintillator
      //encapLOG = new G4LogicalVolume(encap, Scin, "encapLogic");


      //G4LogicalSkinSurface* skin = new G4LogicalSkinSurface("skin",
        //encapLOG, mirrorSurface); //reflective coating


      //G4VSolid* window = new G4Box("windowSolid", allWidth/4,
        //allHeight/3, lenWindow); //entrance window
      //G4LogicalVolume* windowLOG = new G4LogicalVolume(window,
        //Al, "windowLogic");



      //Collimator
      //G4VSolid* box = new G4Box("Box", allWidth/4,
        //allHeight/3, lenColm); //box for tube
```

```
//G4VSolid* cylinder = new G4Tubs("Cylinder",0,2*mm, lenColm,
  //startAngle, spanningAngle); //tube


//G4VSolid* subtract = new G4SubtractionSolid("Box-Cylinder", box,
  //cylinder, 0, G4ThreeVector()); //single array collimator
//G4LogicalVolume* sincolLOG = new G4LogicalVolume(subtract,
  //tugs, "sincolLogic");



//Aluminium Casing
//G4VSolid* box1 = new G4Box("Box1", widthSincas, heightSincas,
  //allDepth+lenPmt+lenWindow+lenColm); //box for tube
//G4VSolid* box2 = new G4Box("Box2", allWidth/4, allHeight/3,
  //allDepth+lenPmt+lenWindow+lenColm);

//G4VSolid* subtract2 = new G4SubtractionSolid("Box1+Box2", box1,
  //box2, 0, G4ThreeVector());
//G4LogicalVolume* sincasLOG = new G4LogicalVolume(subtract2,
  //Al, "sincasLogic"); //single array case

//G4VSolid* cylinder1 = new G4Tubs("Cylinder1", 0,
  //3*(sqrt(593))/4*cm, allDepth+lenPmt+lenWindow+lenColm,
  //startAngle, spanningAngle); //cylinder for box
//G4VSolid* box3 = new G4Box("Box3", allWidth+0.2*cm,
  //allHeight+0.15*cm, allDepth+lenPmt+lenWindow+lenColm);

//G4VSolid* subtract3 = new G4SubtractionSolid("Cylinder1+Box3",
  //cylinder1, box3, 0, G4ThreeVector());
//G4LogicalVolume* allcasLOG = new G4LogicalVolume(subtract3,
  //Al, "allcasLogic"); //complete array case



//Screen of detector
G4VSolid* sensdet = new G4Box("sensdetSolid", allWidth+0.15*cm,
```

```
        allHeight+0.1*cm, allDepth + lenPmt); //complete PMT
    G4LogicalVolume* sensdetLOG = new G4LogicalVolume(sensdet,
      mat, "sensdetLogic");

    G4VSolid* encap = new G4Box("encapSolid", allWidth+0.15*cm,
      allHeight+0.1*cm, allDepth); //complete scintillator
    encapLOG = new G4LogicalVolume(encap, Scin, "encapLogic");

    G4LogicalSkinSurface* skin = new G4LogicalSkinSurface("skin",
      encapLOG, mirrorSurface);

  //Poisition in world

    //Single Detector
    //G4VPhysicalVolume* sincolPHYS = new G4PVPlacement(0,
      //G4ThreeVector(0, 0, -33.1*cm),sincolLOG, "sincolPhysV",
      //sensdetLOG,false, 0, true); //single array collimator
    //G4VPhysicalVolume* encapPHYS = new G4PVPlacement(0,
      //G4ThreeVector(0, 0,-12.1*cm),encapLOG,"encapPhysV",
      //sensdetLOG,false,0,true); //single scintillator
    //G4VPhysicalVolume* windowPHYS = new G4PVPlacement(0,
      //G4ThreeVector(0, 0, 8.5*cm),windowLOG, "encapPhysV",
      //sensdetLOG, false, 0, true); //entrance window
    //G4VPhysicalVolume* sensdetPHYS = new G4PVPlacement(0,
      //G4ThreeVector(0, 0,0),sensdetLOG, "sensdetPhysV", sincasLOG,
      //false, 0, false); //single PMT

    //Detector Array
    //for (G4int i = 0; i < 4; i++)
    //{
    //  for (G4int j = 0; j < 3; j++)
    //  {
    //     G4VPhysicalVolume* sincasPHYS = new G4PVPlacement(0,
    //        G4ThreeVector(-15.3/2 * cm + (i * 20.4)* cm /4,
```

```cpp
  //                -10.1 * cm + (j * 30.3) * cm / 3, 0),
//      sincasLOG,"sincasPhysV",allcasLOG,false,j + i * 12,true);
//  }
//}
//
//G4VPhysicalVolume* allcasPHYS = new G4PVPlacement(0,
  //G4ThreeVector(0, 0, 0), allcasLOG, "allcasPhysV", logicWorld,
  //false, 0, true); //complete Al casing


//Detector Screen
G4VPhysicalVolume* encapPHYS = new G4PVPlacement(0,
  G4ThreeVector(0, 0, -12.5*cm),encapLOG,"encapPhysV",
  sensdetLOG,false,0,true); //scintillator

//Screen
for (G4int i = 0; i < 10; i++)
{
  for (G4int j = 0; j < 5; j++)
  {
    G4RotationMatrix* yRot = new G4RotationMatrix;
    yRot->rotateY(i*(pi/8.5117)*rad);
    yRot->rotateY(-90 * deg);

    G4VPhysicalVolume* sensdetPHYS = new G4PVPlacement(yRot,
      G4ThreeVector(88*cos(i*(pi/8.5117)*rad)*cm,
          -60.4*cm+(j*150.)*cm/4.9668,
          10.15*cm+(88+10.15/tan((pi*8.5117)*rad))
              *sin(i*(pi/8.5117)*rad)*cm),
      sensdetLOG,"sensdetPhysV",logicWorld,false,i+j*10,true);
  }
}
```

```cpp
//Sample
G4double samWidth = 50. * cm;
G4double samHeight = 75. * cm;
G4double samLength = 0.75 * cm;

G4Box* samp = new G4Box("sampSolid", samWidth,
  samHeight, samLength); //Sample
G4LogicalVolume* sampLOG = new G4LogicalVolume(samp, Al,"sampLogic");

//Place in World
new G4PVPlacement(0, G4ThreeVector(0, 0, 0), sampLOG,"sampPHYS",
  logicWorld, false, 0, true);

//Tripod
G4double innerRadius = 0. * cm;
G4double outerRadius = 0.5 * cm;
G4double hz = 50 * cm;

//Legs
G4VSolid* leg1 = new G4Tubs("leg1Solid", innerRadius, outerRadius,
  hz, startAngle, spanningAngle);
G4VSolid* leg2 = new G4Tubs("leg2Solid", innerRadius, outerRadius,
  hz, startAngle, spanningAngle);
G4VSolid* leg3 = new G4Tubs("leg3Solid", innerRadius, outerRadius,
  hz, startAngle, spanningAngle);

G4VSolid* sphere = new G4Orb("sphereSolid", 0.15 * cm);

//Rotation Matrix
G4RotationMatrix* y1Rot = new G4RotationMatrix;
G4RotationMatrix* y2Rot = new G4RotationMatrix;
G4RotationMatrix* y3Rot = new G4RotationMatrix;

//Rotations
```

```cpp
G4double e = (-pi / 4) * rad;
G4double b = 2 * (pi / 3) * rad;

y1Rot->rotateY(b);
y1Rot->rotateX(e);

y2Rot->rotateY(2*b);
y2Rot->rotateX(e);

y3Rot->rotateY(3*b);
y3Rot->rotateX(e);

//Position
G4ThreeVector leg1Pos = G4ThreeVector(hz*sin(b) * sin(e),
  -hz*cos(e), -hz*cos(b) * sin(e));
G4ThreeVector leg2Pos = G4ThreeVector(-hz*sin(2*b) * cos(e),
  hz*sin(e), hz*cos(2*b) * cos(e));
G4ThreeVector leg3Pos = G4ThreeVector(hz*sin(3*b) * sin(e),
  -hz*cos(e), -hz*cos(3*b) * sin(e));

//Legs Union
G4VSolid* union1 = new G4UnionSolid("sphere+leg2", sphere, leg1,
  y1Rot, leg1Pos);
G4VSolid* union2 = new G4UnionSolid("union1+leg2", union1, leg2,
  y2Rot, leg2Pos);
G4VSolid* union3 = new G4UnionSolid("union2+leg3", union2, leg3,
  y3Rot, leg3Pos);

G4LogicalVolume* tripodLOG = new G4LogicalVolume(union3,
  stainsteel, "tripodLogic"); //tripod
//G4VPhysicalVolume* tripodPhys = new G4PVPlacement(0,
  //G4ThreeVector(), tripodLOG, "tripodPHYS",
  //logicWorld, false, 0, true);
```

```cpp
    return physWorld;
  }


  void MySystem2Construction::ConstructSDandField()
  {
    MySensitiveDetector* sensDet =
      new MySensitiveDetector("SensitiveDetector");


    encapLOG->SetSensitiveDetector(sensDet);
  }
```

LISTING B.10: Construction.cpp

```cpp
  //Defined class
  #include "Physics.h"


  MyPhysics::MyPhysics()
  {
//Register or calling of electromagnetic interactions
      RegisterPhysics(new G4EmStandardPhysics());
      RegisterPhysics(new G4OpticalPhysics());
      RegisterPhysics(new G4DecayPhysics());
      RegisterPhysics(new G4RadioactiveDecayPhysics());
  }


  MyPhysics::~MyPhysics()
  {}
```

LISTING B.11: Physics.cpp

```cpp
#include "Generator.h"

MyPrimaryGenerator::MyPrimaryGenerator()
{
    particleSource = new G4GeneralParticleSource();

    G4ParticleDefinition* electronDef =
    G4ParticleTable::GetParticleTable()->FindParticle("e-");
    G4ParticleDefinition* gammaDef =
    G4ParticleTable::GetParticleTable()->FindParticle("gamma");

    particleSource->SetParticleDefinition(electronDef);
    particleSource->SetParticleDefinition(gammaDef);
    particleSource->SetNumberOfParticles(10); //Number of particles
}

MyPrimaryGenerator::~MyPrimaryGenerator()
{
    delete particleSource;
}

void MyPrimaryGenerator::GeneratePrimaries(G4Event *anEvent)
{
    particleSource->GeneratePrimaryVertex(anEvent);
}
```

LISTING B.12: Generator.cpp

```cpp
#include "SensitiveDetector.h"

MySensitiveDetector::MySensitiveDetector(G4String name)
    : G4VSensitiveDetector(name)
{}
```

```cpp
    MySensitiveDetector::~MySensitiveDetector()
    {}

    G4bool MySensitiveDetector::ProcessHits(G4Step *aStep,
        G4TouchableHistory *ROhist)
    {
      G4Track* track = aStep->GetTrack();

//Photon enters the detector is killed and not propagated
      track->SetTrackStatus(fStopAndKill);

//Photon enters the detector
      G4StepPoint* preStepPoint = aStep->GetPreStepPoint();
//Photon goes out of the detector
      G4StepPoint* postStepPoint = aStep->GetPostStepPoint();

      G4ThreeVector posPhoton = preStepPoint->GetPosition();
      G4cout << "Photon position" << posPhoton << G4endl;

     G4double fX = posPhoton.x(), fY = posPhoton.y(), fZ = posPhoton.z();

      G4int evt = G4RunManager::GetRunManager()
        ->GetCurrentEvent()->GetEventID();

      G4AnalysisManager* man = G4AnalysisManager::Instance();
      man->FillH2(6, fX, fY);
      man->FillNtupleIColumn(9, evt);
      man->AddNtupleRow();

      return true;
    }
```

LISTING B.13: SensitiveDetector.cpp

```cpp
    #include "Stepping.h"
    #include "Event.h"


    MySteppingAction::MySteppingAction(MyEventAction* eventAction)
    {
//Event action stored here, to have access
        fEventAction = eventAction;

    }
    MySteppingAction::~MySteppingAction()
    {}
//Store energy in each step
    void MySteppingAction::UserSteppingAction(const G4Step* step)
    {
//Particle energy stored only if inside of the detector
        G4LogicalVolume* volume =
        step->GetPreStepPoint()->GetTouchableHandle()->
            GetVolume()->GetLogicalVolume();

        const MySystem1Construction* detectorConstruction =
            static_cast < const MySystem1Construction>
            (G4RunManager::GetRunManager()->
            GetUserDetectorConstruction());
        G4LogicalVolume* fScoringVolume =
        detectorConstruction->GetScoringVolume();


//Comparisson, if particles are inside of logic volume
        if (volume != fScoringVolume)
            return;
        G4double edep = step->GetTotalEnergyDeposit();
        fEventAction->AddEdep(edep);
    }
```

LISTING B.14: Stepping.cpp

```cpp
    #include "Tracking.h"
    #include "Run.h"

    #include "G4Track.hh"
    #include "G4SystemOfUnits.hh"
    #include "G4PhysicalConstants.hh"

    MyTracking::MyTracking():G4UserTrackingAction()
    { }

        void MyTracking::PreUserTrackingAction(const G4Track* track)
    {
        G4int pid = track->GetDynamicParticle()->GetPDGcode();
        G4double ekin = track->GetKineticEnergy();
        G4ThreeVector vertex = track->GetPosition();
        G4ThreeVector direction = track->GetMomentumDirection();
        G4double weight = track->GetWeight();

        G4double x = vertex.x(), y = vertex.y(), z = vertex.z();
        G4double theta = direction.theta(), phi = direction.phi();
        if (phi < 0.) phi += twopi;
        G4double cost = std::cos(theta);

        G4AnalysisManager* man = G4AnalysisManager::Instance();
        G4double r = vertex.mag();
        G4double dr = man->GetH1Width(2);
        G4double dv = 2 * twopi * r * r * dr;

// Fill histograms
        man->FillH1(1, ekin);
        if (dv > 0.) man->FillH1(2, r, 1. / dv);
        man->FillH1(3, cost);
        man->FillH1(4, phi);
        man->FillH2(1, x, y);
```

```
      man->FillH2(2, y, z);
      man->FillH2(3, z, x);
      man->FillH2(4, phi, cost);
      man->FillH2(5, phi, theta);


// Fill ntuple
      man->FillNtupleIColumn(0, pid);
      man->FillNtupleDColumn(1, ekin);
      man->FillNtupleDColumn(2, x);
      man->FillNtupleDColumn(3, y);
      man->FillNtupleDColumn(4, z);
      man->FillNtupleDColumn(5, theta);
      man->FillNtupleDColumn(6, phi);
      man->FillNtupleDColumn(7, weight);
      man->AddNtupleRow();
   }

```

LISTING B.15: Tracking.cpp

```
   #include "Event.h"


   MyEventAction::MyEventAction(MyRunAction*)
   {
//Counter variable
      fEdep = 0.;
   }


   MyEventAction::~MyEventAction()
   {}


   void MyEventAction::BeginOfEventAction(const G4Event*)
   {
      fEdep = 0.;
   }
```

```cpp
 //Everytime that photon hits the detector, the class is activated
    void MyEventAction::EndOfEventAction(const G4Event*)
    {
//Fill data with energy stored through all event
        G4cout << "Energy deposition: " << fEdep << G4endl;
        G4AnalysisManager* man = G4AnalysisManager::Instance();
        man->FillNtupleDColumn(8,fEdep/keV);
    man->AddNtupleRow();
    }
```

LISTING B.16: Event.cpp

```cpp
    #include "Run.h"


    #include "G4AnalysisManager.hh"
    #include "G4Run.hh"
    #include "G4RunManager.hh"
    #include "G4UnitsTable.hh"
    #include "G4SystemOfUnits.hh"


    MyRunAction::MyRunAction()
    {
//Printing event number per each event
     G4RunManager::GetRunManager()->SetPrintProgress(1);


     G4AnalysisManager* man = G4AnalysisManager::Instance();


     man->SetVerboseLevel(1);
     man->SetNtupleMerging(true);


     G4int nbins = 100.;
     G4double vmin = 0.;
     G4double vmax = 100.;
```

```cpp
   man->SetHistoDirectoryName("histo");
   man->SetFirstHistoId(1);

   G4int id = man->CreateH1("h1.1", "kinetic energy",
     nbins, vmin, vmax);
   id = man->CreateH1("h1.2", "vertex dist dN/dv = f(r)",
     nbins, vmin, vmax);
   id = man->CreateH1("h1.3", "direction: cos(theta)",
     nbins, vmin, vmax);
   id = man->CreateH1("h1.4", "direction: phi", nbins, vmin, vmax);

//2d
   id = man->CreateH2("h2.1", "vertex: XY", nbins, vmin, vmax,
     nbins, vmin, vmax);
   id = man->CreateH2("h2.2", "vertex: YZ", nbins, vmin, vmax,
     nbins, vmin, vmax);
   id = man->CreateH2("h2.3", "vertex: ZX", nbins, vmin, vmax,
     nbins, vmin, vmax);
   id = man->CreateH2("h2.4", "direction: phi-cos(theta)",
     nbins, vmin, vmax, nbins, vmin, vmax);
   id = man->CreateH2("h2.5", "direction: phi-theta",
     nbins, vmin, vmax, nbins, vmin, vmax);
     id = man->CreateH2("h2.6","photon: XY",nbins,vmin,vmax,
        nbins,vmin,vmax);

   man->SetNtupleDirectoryName("ntuple");
   man->SetFirstNtupleId(1);
   man->CreateNtuple("101", "Primary Particle Tuple");
   man->CreateNtupleIColumn("particleID");    //column 0
   man->CreateNtupleDColumn("Ekin");          //column 1
   man->CreateNtupleDColumn("posX");          //column 2
   man->CreateNtupleDColumn("posY");          //column 3
   man->CreateNtupleDColumn("posZ");          //column 4
```

```cpp
  man->CreateNtupleDColumn("dirTheta");      //column 5
  man->CreateNtupleDColumn("dirPhi");        //column 6
  man->CreateNtupleDColumn("weight");        //column 7
    man->CreateNtupleDColumn("fEdep");       //column 8
  man->CreateNtupleIColumn("fEvent");      //column 9
  man->CreateNtupleDColumn("fX");        //column 10
  man->CreateNtupleDColumn("fY");        //column 11
  man->CreateNtupleDColumn("fZ");        //column 12
  man->FinishNtuple();
}


MyRunAction::~MyRunAction()
{
}


void MyRunAction::BeginOfRunAction(const G4Run* run)
{
  G4AnalysisManager* man = G4AnalysisManager::Instance();
  G4int runID = run->GetRunID();

  std::stringstream strRunID;
  strRunID << runID;

  G4String fileName = "sim"+strRunID.str()+".root";
  man->OpenFile(fileName);
  G4cout << "Using" << man->GetType() << G4endl;

}


void MyRunAction::EndOfRunAction(const G4Run*)
{
  G4AnalysisManager* man = G4AnalysisManager::Instance();

  man->Write();
```

```
    man->CloseFile();
    }
```

LISTING B.17: Run.cpp

```cpp
    #include "Action.h"
    #include "Generator.h"
    #include "Run.h"
    #include "Event.h"
    #include "Stepping.h"
    #include "Tracking.h"

    MyActionInitialization::MyActionInitialization()
    {}

    MyActionInitialization::~MyActionInitialization()
    {}

//Construction of primary particle, run, event, stepping and tracking
    void MyActionInitialization::Build() const
    {
        MyPrimaryGenerator* generator = new MyPrimaryGenerator();
        SetUserAction(generator);

        MyRunAction* runAction = new MyRunAction();
        SetUserAction(runAction);

        MyEventAction* eventAction = new MyEventAction(runAction);
        SetUserAction(eventAction);

        MySteppingAction* steppingAction =
        new MySteppingAction(eventAction);
        SetUserAction(steppingAction);
```

```cpp
    MyTracking* tracking = new MyTracking();
  SetUserAction(tracking);
}
```

LISTING B.18: Action.cpp

B.3 Main Program

```cpp
//
// ***********************************************************************
// * License and Disclaimer                                             *
// *                                                                     *
// * The  Geant4 software  is  copyright of the Copyright Holders  of *
// * the Geant4 Collaboration.  It is provided  under  the terms  and *
// * conditions of the Geant4 Software License,  included in the file *
// * LICENSE and available at  http://cern.ch/geant4/license .  These *
// * include a list of copyright holders.                               *
// *                                                                     *
// * Neither the authors of this software system, nor their employing *
// * institutes,nor the agencies providing financial support for this *
// * work  make  any representation or  warranty, express or implied, *
// * regarding  this  software system or assume any liability for its *
// * use.  Please see the license in the file  LICENSE  and URL above *
// * for the full disclaimer and the limitation of liability.         *
// *                                                                     *
// * This  code  implementation is the result of  the  scientific and *
// * technical work of the GEANT4 collaboration.                      *
// * By using,  copying,  modifying or  distributing the software (or *
// * any work based  on the software)  you  agree  to acknowledge its *
// * use  in  resulting  scientific  publications,  and indicate your *
// * acceptance of all terms of the Geant4 Software license.          *
// ***********************************************************************
```

```
//
    #include <iostream> //Start-up of the program

    #include "G4Types.hh" //Definition of parameters (e.g., int, bool)
    #include "G4RunManager.hh" //Running of other files
    #include "G4UIExecutive.hh" //User interface
    #include "G4VisExecutive.hh" //Visualization
    #include "G4VisManager.hh" //Part of visualization package
    #include "G4UImanager.hh" //Part of user interface package

    #include "System2Construction.h" //Defined geometry
    #include "Physics.h" //Defined physcis
    #include "Action.h" //Defined actions

    int main(int argc, char** argv) //Rooting for parameters
    {
        //Run program
        G4RunManager* runManager = new G4RunManager();
        //Initialization of defined classes
        runManager->SetUserInitialization(new MyConstruction());
        runManager->SetUserInitialization(new MyPhysics());
        runManager->SetUserInitialization(new MyActionInitialization());
        runManager->Initialize();

    G4UIExecutive* ui = 0;

        if (argc == 1)
        {
            ui = new G4UIExecutive(argc, argv);
        }

        G4VisManager* visManager = new G4VisExecutive();
        visManager->Initialize();
```

```cpp
    G4UImanager* UImanager = G4UImanager::GetUIpointer();
    if (ui)
    {
        UImanager->ApplyCommand("/control/execute vis.mac");
        if (ui-> IsGUI()) {
            UImanager->ApplyCommand("/control/execute run.mac");
        }
        ui->SessionStart();
    }
    else
    {
        G4String command = "/control/execute";
        G4String fileName2 = argv[1];
        UImanager->ApplyCommand(command+fileName2);
}
    delete visManager;
    delete runManager;
    return 0;
}
```

LISTING B.19: sim.cpp

Appendix C

Extra Files

C.1 Text Files

```
cmake_minimum_required(VERSION 3.16...3.21 FATAL_ERROR)

project(Simulation)

find_package(Geant4 REQUIRED ui_all vis_all)

option(WITH_GEANT4_UIVIS
    "Build example with Geant4 UI and Vis drivers" ON)
if(WITH_GEANT4_UIVIS)
  find_package(Geant4 REQUIRED ui_all vis_all)
else()
  find_package(Geant4 REQUIRED)
endif()

include(${Geant4_USE_FILE})
include_directories(${PROJECT_SOURCE_DIR}/include)

file(GLOB sources ${PROJECT_SOURCE_DIR}/src/*.cpp)
file(GLOB headers ${PROJECT_SOURCE_DIR}/include/*.h)

add_executable(sim sim.cpp ${sources} ${headers})
target_link_libraries(sim ${Geant4_LIBRARIES})
```

```
set(SIM_SCRIPTS
  vis.mac
  run.mac
  )

foreach(_script ${SIM_SCRIPTS})
  configure_file(
  ${PROJECT_SOURCE_DIR}/${_script}
  ${PROJECT_BINARY_DIR}/${_script}
  COPYONLY
  )
endforeach()

add_custom_target(Simulation DEPENDS sim)

install(TARGETS sim DESTINATION bin)
```

LISTING C.1: CMakeLists.txt

```
/run/initialize

#Case 1
#/gps/particle ion
#/gps/ion 27 60
#/gps/pos/type Plane
#/gps/pos/shape Circle
#/gps/pos/centre 0. 0. 0. cm
#/gps/pos/radius 1.5 cm
#/gps/number 30
#/gps/ang/type iso

#Case 2
#/gps/particle ion
```

```
#/gps/ion 27 60
#/gps/pos/type Plane
#/gps/pos/shape Square
#/gps/pos/centre 40. 70. 0. cm
#/gps/pos/halfx 3. cm
#/gps/pos/halfy 3. cm
#/gps/number 30
#/gps/ang/type iso

#Case 3
#/gps/source/add 1.
#/gps/particle ion
#/gps/ion 27 60
#/gps/pos/type Plane
#/gps/pos/shape Circle
#/gps/pos/centre 25. 0. 0. cm
#/gps/pos/radius 1.5 cm
#/gps/number 1
#/gps/ang/type iso

#/gps/source/add 1.
#/gps/particle ion
#/gps/ion 27 60
#/gps/pos/type Plane
#/gps/pos/shape Circle
#/gps/pos/centre -25. 0. 0. cm
#/gps/pos/radius 1.5 cm
#/gps/number 1
#/gps/ang/type iso

#/gps/source/multiplevertex true

#Case 4
/gps/particle ion
```

```
/gps/ion 27 60
/gps/pos/type Surface
/gps/pos/shape Cylinder
/gps/pos/centre 0. 0. 0. cm
/gps/pos/radius 1.5 cm
/gps/pos/halfz 0.5 cm
/gps/number 1
/gps/ang/type iso

#Histograms axes
#Source
/analysis/h2/setX 1 100 -50 50 cm
/analysis/h2/setY 1 100 -75 75 cm

#Case 1
#/analysis/h2/setX 6 100 -11.5 10.5 cm  #x-y
#/analysis/h2/setY 6 100 -16.5 15.5 cm #x-y

#Case 2
#/analysis/h2/setX 6 100 29 51 cm  #x-y
#/analysis/h2/setY 6 100 54 86 cm #x-y

#Case 3 and 4
/analysis/h2/setX 6 100 -65 65 cm  #x-y
/analysis/h2/setY 6 100 -16.5 16.5 cm #x-y

/run/printProgress 10000
/run/beamOn 3000

/tracking/verbose 0
```

LISTING C.2: Run File: run.mac

```
/vis/open OGL
/vis/viewer/set/viewpointVector 1 1 1
/vis/drawVolume
/vis/viewer/set/autoRefresh true
/vis/scene/add/trajectories smooth
/vis/scene/add/scale 10 cm
/vis/scene/add/axes
/vis/scene/add/eventID
/vis/scene/endOfEventAction accumulate
/vis/modeling/trajectories/create/drawByParticleID
/vis/modeling/trajectories/drawByParticleID-0/set gamma yellow
/vis/modeling/trajectories/drawByParticleID-0/set e- red
/vis/modeling/trajectories/drawByParticleID-0/set anti_nu_e grey
```

LISTING C.3: Visualization File: vis.mac